VISIBLE LIGHT COMMUNICATION TECHNIQUES FOR FUTURE GENERATION UNDERWATER NETWORKS

A Dissertation

by

Mohammed Elamassie

Submitted to the
Graduate School of Sciences and Engineering
In Partial Fulfillment of the Requirements for
the Degree of

Doctor of Philosophy

in the
Department of Electrical and Electronics Engineering

Özyeğin University
June 2020

VISIBLE LIGHT COMMUNICATION TECHNIQUES FOR FUTURE GENERATION UNDERWATER NETWORKS

Approved by:

Professor Murat Uysal, Advisor
Department of Electrical and Electronics Engineering
Özyeğin University

Assistant Professor Kadir Durak
Department of Electrical and Electronics Engineering
Özyeğin University

Assistant Professor Ahmet Tekin
Department of Electrical and Electronics Engineering
Özyeğin University

Associate Professor Ertuğrul Başar
Department of Electrical and Electronics Engineering
Koç University

Date Approved: 08 June 2020

Assistant Professor Tuncer Baykas
Department of Electrical and Electronics Engineering
Istanbul Medipol University

I dedicate this dissertation to my beloved parents, who have instilled in me the desire to learn and helped me in everything great and small.

ABSTRACT

The demand for underwater communication systems has increased due to the increasing expansion of human activities in underwater environments such as underwater scientific data collection, environmental monitoring, offshore oil field exploration, maritime archaeology, port security and tactical surveillance. Wire-line systems (especially optical fiber systems) can be used to provide real-time communication, but their lack of flexibility, high cost and operational disadvantages become restrictive for most practical scenarios. This increases the demand for underwater wireless communications. The typical choice for wireless transmission underwater is acoustic signaling, which can support transmission ranges in the order of kilometers. It, however, falls short with its low data rate (in the order of tens of Kilobits Per Second (Kb/s)) for high-bandwidth underwater applications such as image and real-time video transmission. For short and medium ranges, optical communication has emerged as a high-capacity alternative. Since water is relatively transparent to blue or green light (450 nm – 550 nm), Laser Diodes (LDs) or Light Emitting Diodes (LEDs) can be used as transmitters for underwater wireless connectivity with data rates in the orders of tens of Megabits Per Second (Mb/s). Despite the increasing attention on Underwater Visible Light Communication (UVLC) systems, there is still a need for investigating the performance limit of UVLC, investigating the benefits of link adaptation, accurate modeling of Underwater Optical Turbulence (UOT), mitigating the turbulence effect and developing the physical layer algorithms.

Motivated by these, we firstly investigate the performance limit of UVLC system in the absence of turbulence and pointing errors, which can be considered as an ideal benchmark. Particularly, we investigate the maximum achievable link distance to achieve a specified targeted Bit Error Rate (BER) in the pure sea, clear ocean, coastal water and harbor water

based on the recently introduced closed-form path loss ratio expression. We further consider the deployment of relay-assisted transmission and determine the maximum achievable distance for a given number of hops to satisfy a targeted end-to-end BER.

Investigating the performance limit of UVLC systems requires also studying it with the required data speed for high-bandwidth underwater applications. Since UVLC aim to achieve high data rates sufficiently high for real-time image and video transmission, the transmission may experience frequency-selectivity. This necessitates the use of efficient multi-carrier techniques such as Orthogonal Frequency Division Multiplexing (OFDM). Therefore, we consider an adaptive DC-biased optical-OFDM (DCO-OFDM) and investigate the benefits of link adaptation in the context of OFDM-based UVLC systems in the absence of turbulence and pointing errors.

In the above points, the effect of UOT on the performance of UVLC systems is excluded. However, the performance of UVLC is severely affected by UOT. UOT introduces instantaneous fluctuations over the average received power as a result of the fluctuation in the refractive index of seawater. This is mainly caused by temperature and salinity fluctuations. Therefore, we develop an accurate spatial power spectrum model of turbulent fluctuations of the sea-water refraction index that accurately describe how the fluctuation in both temperature and salinity contribute to the fluctuation in the refractive index. Additionally, since both temperature and salinity of the seawater are not constant but change with depth and hence vertical links may experience variation in turbulence strength through the transmission range, we characterize the vertical UVLC optical turbulence channels.

Utilizing our spectrum model and turbulence channels, we investigate the performance of UVLC systems. Particularly, we derive closed-form expressions for the BER performance of UVLC system based on the cascaded structure of the fading coefficient considering both weak and moderate/strong turbulence conditions. Then, we analyze the asymptotic behavior of BER and determine the diversity orders. Additionally, we derive closed-form expressions for the average Ergodic capacity of UVLC systems.

Since the performance of UVLC is severely affected by UOT, we investigate the benefit of using different fading mitigation techniques on the performance of UVLC systems. Particularly, we consider the deployment of multiple transmitters and/or receivers to extract the spatial diversity. As an alternative, we consider the deployment of Transmit Laser Selection (TLS) that can extract full diversity while significantly reducing the complexity of the front-end. We propose the concept of Incremental Diversity Order (IDO) to quantify diversity gains of communication systems over Lognormal (LN) fading channels, which is defined as the incremental change in the decreasing rate of BER in log-log scale and determines how fast the diversity order changes with Signal-to-Noise Ratio (SNR).

In the last part of this dissertation, we consider a practical implementation of Underwater Sensor Networks (USNs) that requires the design of multiple access systems for supporting several sensor nodes. We first introduce the use of adaptive Orthogonal Frequency Division Multiple Access (OFDMA) in the context of UVLC systems. The adaptive system is formulated such that the overall data rate is maximized subject to two constraints: identical user's data rate and BER of each user not exceeding a pre-defined maximum acceptable BER. We further consider Non-Orthogonal Multiple Access (NOMA) in the context of USN and investigate the achievable NOMA capacity.

ÖZETÇE

Sualtı bilimsel veri toplama, çevresel izleme, açık deniz petrol sahası araştırmaları, deniz arkeolojisi, liman güvenliği ve taktik gözetim gibi su altı ortamlarında artan insan faaliyetleri nedeniyle su altı iletişim sistemlerine olan talep artmıştır. Kablolu haberleşme sistemleri (özellikle optik fiber sistemler) gerçek zamanlı iletişim sağlamak için kullanılabilir, ancak esnek bir çözüm olmaması, yüksek maliyet ve operasyonel dezavantajları nedeniyle çoğu pratik senaryo için kısıtlayıcı hale gelmektedir. Bu durum, su altı kablosuz haberleşme sistemlerine olan talebi arttırmaktadır.

Sualtı kablosuz haberleşme için geleneksel seçim, kilometrelerce haberleşme mesafesi destekleyebilen akustik haberleşmedir. Fakat bu sistemler, görüntü ve gerçek zamanlı video aktarımı gibi yüksek bant genişlikli sualtı uygulamaları için düşük veri hızına sahip olmaları nedeniyle (saniyede onlarca Kilobit/Saniye (Kb/s)) yetersiz kalır. Kısa ve orta menzilli haberleşme için optik iletişim, yüksek kapasiteli bir alternatif olarak ortaya çıkmıştır. Su ortamı, mavi veya yeşil ışık dalgaboylarına (450 nm – 550 nm) nispeten etkisiz olduğundan, Lazer Diyotlar (LD'ler) veya Işık Yayan Diyotlar (LED'ler), onlarca Megabit/Saniye (Mb/s) hızlara ulaşan veri hızlarıyla su altı kablosuz haberleşme için kullanılabilir.

Sualtı Görünür Işık İletişimi (UVLC) sistemlerine artan ilgiye rağmen, UVLC'nin başarım sınırını araştırmaya, bağlantı adaptasyonunun faydalarını araştırmaya, Sualtı Optik Türbülansının (UOT) doğru modellenmesine, türbülans etkisini azaltmaya ve fiziksel katman algoritmalarını geliştirmeye hala ihtiyaç vardır.

Bunları amaç edinerek, öncelikle ideal durumdaki referans olarak kabul edilebilecek türbülans ve işaretleme hatalarının yokluğunda UVLC sisteminin başarım sınırını

araştırıyoruz. Özellikle, yakın zamanda piyasaya sürülen kapalı-form yol kaybı oranı ifadesine dayanarak saf deniz, berrak okyanus, kıyı suyu ve liman suyunda belirli bir hedeflenen Bit Hata Oranını (BER) elde etmek için ulaşılabilecek maksimum bağlantı mesafesini araştırıyoruz. Ayrıca, röle destekli iletimin konumlandırılmasını düşünüyoruz ve hedeflenen uçtan uca BER'i karşılamak amacıyla belirli sayıda atlama ile ulaşılabilecek maksimum mesafeyi belirliyoruz.

UVLC sistemlerinin başarım sınırının araştırılması, yüksek bant genişlikli sualtı uygulamaları için gerekli veri hızı ile de incelenmesini gerektirir. UVLC, gerçek zamanlı görüntü ve video iletimi için yeterince yüksek yüksek veri hızları elde etmeyi amaçladığından, iletim frekans seçiciliği yaşayabilir. Bu, Dikey Frekans Bölmeli Çoğullama (OFDM) gibi verimli çok taşıyıcılı tekniklerin kullanılmasını gerektirir. Bu nedenle, adaptif bir Doğrusal Akım (DC) merkezli optik-OFDM (DCO-OFDM) düşünüyor ve türbülans ve işaretleme hataları olmadan OFDM tabanlı UVLC sistemleri bağlamında link adaptasyonunun faydalarını araştırıyoruz.

Yukarıdaki noktalarda, UOT'nin UVLC sistemlerinin başarımı üzerindeki etkisi hariç tutulmuştur. Bununla birlikte, UVLC'nin başarımı UOT'den ciddi şekilde etkilenir. UOT, deniz suyunun kırılma endeksindeki dalgalanmanın bir sonucu olarak, ortalama alınan güç üzerinde anlık dalgalanmalar ortaya koymaktadır. Bu esas olarak sıcaklık ve tuzluluk dalgalanmalarından kaynaklanır. Bu nedenle, deniz suyu kırılma endeksinin türbülans dalgalanmalarının, hem sıcaklık hem de tuzluluktaki dalgalanmanın kırılma endeksindeki dalgalanmaya nasıl katkıda bulunduğunu doğru bir şekilde tanımlayan doğru bir uzaysal güç spektrum modeli geliştiriyoruz. Ayrıca, deniz suyunun hem sıcaklığı hem de tuzluluğu sabit olmadığından, derinlikle değiştiğinden ve bu nedenle dikey bağlantılar, iletim aralığı boyunca türbülans mukavemetinde değişiklik yaşayabildiğinden, dikey UVLC optik türbülans kanallarını karakterize ediyoruz.

Spektrum modelimizi ve türbülans kanallarımızı kullanarak UVLC sistemlerinin başarımını araştırıyoruz. Özellikle, zayıf ve orta / kuvvetli türbülans koşullarını göz önünde bulundurarak sönümleme katsayısının kademeli yapısına dayalı UVLC sisteminin BER başarımı için kapalı-form ifadeleri türetiyoruz. Ardından, BER'in asimptotik davranışını analiz eder ve çeşitlilik düzenlerini belirleriz. Ek olarak, UVLC sistemlerinin ortalama ergodik kapasitesi için de kapalı form ifadeleri türetiyoruz.

UVLC'nin başarımı UOT'den ciddi şekilde etkilendiğinden, UVLC sistemlerinin başarımı üzerinde farklı sönümleme önleme tekniklerinin kullanılmasının yararını araştırıyoruz. Özellikle, mekansal çeşitliliği çıkarmak için birden fazla verici ve / veya alıcı konuşlandırılmasını düşünüyoruz. Alternatif olarak, ön çeşitliliğin karmaşıklığını önemli ölçüde azaltırken, tam çeşitliliği elde edebilen İletim Lazer Seçimi'nin (TLS) konuşlandırılmasını düşünüyoruz. Daha sonra log-log ölçeğinde BER'nin azalan oranındaki artımlı değişiklik olarak tanımlanan ve lognormal (LN) solma kanalları üzerinden iletişim sistemlerinin çeşitlilik kazanımlarını ölçmek için SNR ile çeşitlilik sırası değişikliklerinin ne kadar hızlı değiştiğini ortaya çıkaran Artımlı Çeşitlilik Düzeni (IDO) kavramını öneriyoruz.

Bu tezin son bölümünde, çeşitli sensör düğümlerini desteklemek için çoklu erişim sistemlerinin tasarlanmasını gerektiren Sualtı Sensörü Ağlarının (USN) pratik bir uygulamasını düşünüyoruz. İlk olarak UVLC sistemleri bağlamında uyarlanabilir Dikey Frekans Bölmeli Çoklu Erişim (OFDMA) kullanımını sunuyoruz. Uyarlanabilir sistem, toplam veri hızının iki kısıtlamaya tabi olarak maksimize edileceği şekilde formüle edilmiştir: özdeş kullanıcının veri hızı ve her kullanıcının BER'ini aşmayacak şekilde, önceden tanımlanmış bir maksimum kabul edilebilir. Ayrıca USN bağlamında Dikey Olmayan Çoklu Erişimi (NOMA) ele alıyor ve ulaşılabilir NOMA kapasitesini araştırıyoruz.

ACKNOWLEDGEMENTS

I want to express my appreciation to my advisor, Prof. Murat Uysal, for his wisdom, friendship, encouragement, support, patient guidance, invaluable insights and suggestions during this experience as a PhD student and research assistant. The work of the thesis would not be possible without his consistent support and guidance. I also had a great opportunity to work with him. I learned a lot from him throughout my PhD studies.

I am totally grateful to the members of my dissertation committee, Asst. Prof. Ahmet Tekin, Asst. Prof. Tuncer Baykaş, Asst. Prof. Kadir Durak and Assoc. Prof. Ertuğrul Başar for their time serving on my committee and carefully reviewing my dissertation.

I very gratefully acknowledge the funding received towards my PhD from The Scientific and Technological Research Council of Turkey (TÜBİTAK) under Grant 215E119 (01/11/2016 - 31/05/2019) and 215E311 (13/06/2019 - 15/07/2020).

I am also grateful for technical and non-technical discussions with my colleagues in the CT&T research group at Özyeğin university. I have as well enjoyed the collaboration and fruitful conversations with members of The Center of Excellence for Optical Wireless Communications Technologies (OKATEM).

My warmest gratitude goes to my parents, Taysier and Nawal, who always supported me unconditionally throughout my life. Their sacrifice was great. The distances separated us, so I could not see them during the period of doctoral studies, and they could not attend my thesis defense. I would like to lovingly thank my wife, Salma, for her unconditional love, unrestricted kindness, and unlimited patience. I would like to especially thank my sisters: Weeam, Haneen, Samah, Amal, Eman, Israa, Huda and Nada for their continuous support. I will be forever indebted to my family for their unlimited trust and willingness to endure with me the difficulties and stresses of my endeavours. Finally, I would like to thank my wonderful children: Taysier and Ahmad.

ACRONYMS

AF	Amplify-and-Forward
AIDO	Asymptotical Incremental Diversity Order
ARDO	Asymptotical Relative Diversity Order
AWGN	Additive White Gaussian Noise
AUV	Autonomous Underwater Vehicle
BER	Bit Error Rate
b/s	Bits Per Subcarrier
CIR	Channel Impulse Response
CP	Cyclic Prefix
DCO	DC-Biased Optical
DCO-OFDM	DC-biased optical-OFDM
DF	Detect-and-Forward
DFT	Discrete Fourier Transform
DO	Diversity Order
EGC	Equal Gain Combining
FSO	Free-Space Optical
FSOC	Free-Space Optical Communication
Gb/s	Gigabits Per Second
GG	Gamma-Gamma
GTLS	Generalized Transmit Laser Selection
IDFT	Inverse Discrete Fourier Transform
IDO	Incremental Diversity Order
i.i.d	Independent and Identical Distributed

IM/DD	Intensity Modulation / Direct Detection
i.n.i.d	Independent and Non-Identical Distributed
Kb/s	Kilobits Per Second
LD	Laser Diode
LED	Light Emitting Diode
LN	Lognormal
LOS	Line of Sight
Mb/s	Megabits Per Second
MIMO	Multiple-Input Multiple-Output
MS/s	Mega-Symbols Per Second
NOMA	Non-Orthogonal Multiple Access
OFDM	Orthogonal Frequency Division Multiplexing
OFDMA	Orthogonal Frequency Division Multiple Access
OTHG	One-term Henyey-Greenstein
OOK	On-Off Keying
PDF	Probability Density Function
PAM	Pulse-Amplitude Modulation
PPT	Part Per Thousand
PSK	Phase Shift Keying
QAM	Quadrature Amplitude Modulation
RDO	Relative Diversity Order
RF	Radio Frequency
RTE	Radiative Transfer Equation
SIC	Successive Interference Cancellation
SISO	Single-Input Single-Output
SNR	Signal-to-Noise Ratio
TLS	Transmit Laser Selection

VLC	Visible Light Communication
UOT	Underwater Optical Turbulence
UOWC	Underwater Optical Wireless Communication
USN	Underwater Sensor Network
UVLC	Underwater Visible Light Communication

TABLE OF CONTENTS

LIST OF TABLES

LIST OF FIGURES

LIST OF ALGORITHMS

CHAPTER I

INTRODUCTION

1.1 Motivation

The demand for underwater communication systems is increasing due to the continuous and diversified expansion in human activities such as underwater scientific data collection, environmental monitoring, oil field exploration, maritime archaeology, port security and tactical surveillance [1]. Wire-line systems (especially fiber optical systems) can be used to provide real-time communication for underwater applications. However, due to its high cost, lack of flexibility and operational disadvantages, it is restricted for most practical cases. This increases the demand for underwater wireless connections.

Several wireless technologies, e.g., Radio Frequency (RF), acoustic and optical signaling are considered as connectivity solutions. While RF is considered as a practical solution for short-range communications with data rate up to 100 Mb/s, it is not always preferred due to size and cost limitations. On the other hand, acoustic technology was considered effective communication scheme for long-range transmissions. However, the major challenge in this technology is the low data rate which is in the order of Kb/s. In this respect, Underwater Optical Wireless Communication (UOWC) with data rates in the orders of tens of Mb/s [2] has been proposed recently to address these challenges.

As light propagates through water, ultraviolet and infrared signals are absorbed first, leaving visible light restricted, mainly, to the blue-green part of the spectrum as the best wavelength for underwater transmission [3]. While the green part of the spectrum has less attenuation in the coastal water, the blue part of the spectrum has less attenuation in the open ocean [4]. Based on this, there has been increasing investigations of UVLC in the blue-green part of the spectrum [5–14]. In this regard, studying the performance limits of UVLC systems based on accurate models of optical channel gain in the absence of turbulence, which can be considered as an ideal benchmark, is the first thing that needs to be addressed and studied in detail. Recalling the fact that UVLC is required to achieve sufficiently high data rates for real-time image and video transmission. These high data rates may experience frequency selectivity. Therefore, the use of powerful adaptive multi-carrier technologies such as OFDM should be investigated.

The performance of UVLC systems is severely affected by UOT, which introduces instantaneous fluctuations over the average received power [15] as a result of the fluctuation in the refractive index of seawater. This is mainly caused by temperature and salinity fluctuations. Therefore, there is a need for accurate spatial power spectrum model of turbulent fluctuations of the sea-water refraction index that accurately describe how the fluctuation in both temperature and salinity contribute to the fluctuation in the refractive index. Furthermore, the temperature and salinity of the seawater are not constant but change with depth. Accordingly, the vertical link may experience variation in turbulence strength through the transmission range of vertical UVLC links. Therefore, vertical UVLC links must be characterized considering actual temperature and salinity distributions.

As a result of the fact that underwater communication systems are highly affected by UOT, there are increasing studies to combat and reduce its impact. These include the deployment of multiple transmitters and/or receivers in UVLC [16–18] to extract the spatial diversity. This concept has been widely adopted in the context of Free-Space Optical Communication (FSOC) [19–21]. As an alternative, TLS can be considered where only one of the transmitters is active. This method is able to extract full diversity while significantly reducing the complexity of the front-end. The same concept was earlier studied in the context of terrestrial Free-Space Optical (FSO) links [22–24]. These technologies require further research to see how effective they are in underwater optical communication systems. Since link distance of UVLC is extremely short compared to those in FSOC systems, this may make underwater optical turbulence typically modeled by LN. As a result, investigating the asymptotic behaviour of BER and outage probabilities over LN channels is a big challenge and needs to be addressed.

The practical implementation of USNs requires the design of multiple access systems for supporting several sensor nodes. Motivated by this, several multiple access schemes have been proposed in the open literature for supporting multiple nodes connectivity. Multiple-access can be divided into orthogonal and non-orthogonal multiple access schemes. In orthogonal multiple access schemes, nodes are allocated orthogonal resources. This requires the design of an adaptive algorithm for efficiently allocating the resources. In NOMA schemes, multiple users simultaneously share the entire available frequency and time resources, with a controlled interference threshold in order to increase the overall system capacity. Therefore, in order to quantify the benefits of using NOMA in the context of UVLC, we need to investigate the overall system capacity in an underwater environment.

1.2 Overview of Underwater Wireless Communication

Underwater connectivity is needed in different applications such as undersea exploration for natural minerals, environment monitoring for the effect of human underwater activities on the marine ecosystem, and navigation assisting by locating dangerous rocks in shallow water.

Wire-line systems such as the fiber optic are the ideal connectivity solution in terms of high data bandwidth and long link range underwater since the glass fibers are manufactured to have extremely low scattering and absorption coefficients in addition to the fact that they work in the near infra-red part of the spectrum. The obvious disadvantage of this technology is that the transmitter and receiver must be physically connected by cables, which makes this option not suitable for communications with some types of underwater vehicles. Besides, the difficulty and cost of maintenance increase the need for wireless communication options.

Wireless communications in an underwater environment have new challenges, especially when compared to wireless communications through the atmosphere. This environment requires sophisticated communication devices to achieve relatively low transmission rates, even at relatively short communication distances [1]. The three methods for achieving underwater wireless communication are acoustics, RF and optics. The advantages and disadvantages of each are as follows

- **Acoustic communications:** Acoustic waves are the most widely used technique for underwater wireless communications. Among the aforementioned three techniques, acoustics offer the longest range up to tens of kilometers. However, there are several challenges/drawbacks for underwater acoustic wireless communication such as huge delay as a result of low propagation speed, low data rate as a result of limited available bandwidth and multi-path propagation.

  Furthermore, frequencies of this limited bandwidth experience different attenuation. At high acoustic frequencies, the absorption is dominated by the viscous absorption of the fluid. At low acoustic frequencies, the molecular absorption of dissolved compounds such as magnesium carbonate and Boric acid are the dominant factors. Moreover, attenuation is different for different physical characteristics of the underwater medium such as temperature, salinity, and pressure. Additionally, acoustic waves have an adverse impact on marine life.

- **RF communications:** Recalling the fact that acoustic signaling yields poor performance in water and harms marine life. As an alternative RF signaling can be used to achieve faster wireless transmission. Unlike acoustic signaling, RF is not affected by temperature and depth and it has two main features. RF wave can cross air/water boundary easily and smoothly. This feature enables unifies both underwater and terrestrial RF communication systems. It is remarkable that underwater RF communication is the method that is most tolerant to the water turbulence and turbidity.

However, there are some obstacles and limitations of using RF underwater: the large antenna size needed in freshwater and high attenuation in seawater. Furthermore, this method is limited by the relatively short link range.

- **Optical communications:** The outstanding and distinguished technical features of UOWC are the lowest delay, the highest security, the highest data rate and the lowest implementation costs compared to other aforementioned underwater wireless methods. The high-speed of UOWC makes it the best candidate for real-time applications like underwater imaging and video transmission. In UOWC systems, Line of Sight (LOS) configuration is typically employed. This helps to prevent eavesdroppers, and hence improving communication security. Furthermore, UOWC is the most energy-efficient and cost-effective mean of underwater wireless communication.

  However, UOWC also has some challenges. These challenges are listed as follows:

  - Optical signaling suffers from severe absorption and scattering.
  - Optical links with LOS configuration require transceivers' alignment.
  - The physical characteristics of water such as temperature and salinity strongly influence the performance.

Table 1: Comparison of wireless communication technologies underwater [25].

	Advantages/Benefits/Facts	Disadvantages/Limitations
Acoustic	Most widely used technology. Long communication range up to 20 km.	Low data rate (in the order of Kb/s). Large latency (in the order of seconds). Bulky, costly and energy consuming transceivers. Harmful to some marine life.
RF	Relatively smooth transition to cross air/water boundary. More tolerant to water turbulence and turbidity. Loose pointing requirement. Moderate data rate (up to 100 Mb/s) at close distances.	Relatively short link range. Bulky, costly and energy consuming transceivers.
Optical	Ultra-high data rate (in the order of Gbp/s). Immune to transmission latency. Low cost and small volume transceivers.	Can not cross air/water boundary easily. Suffer from severe absorption and scattering. Short link range (up to tens of meters).

1.3 Underwater Optical Wireless Communications

Optical wireless communication has emerged as a high-capacity alternative to acoustic and RF counterparts. Since water is relatively transparent to blue or green light with a wavelength in the range of (450 nm –550 nm), LDs or LEDs can be used as transmitters for underwater wireless connectivity with data rates in the orders of tens of Mb/s [2]. Experimental UVLC demonstrations exceeding Gigabits Per Second (Gb/s) were further reported in the controlled lab environments [26–29]. Designing a realistic UOWC system and verifying its effectiveness requires studying two things in depth which are accurate attenuation and turbulence models.

1.3.1 Attenuation Models

In recent years, there has been a growing literature on UVLC. These works span from channel modeling to physical layer and upper layer issues [6, 30–43]. In such an emerging topic, channel modeling is particularly important to understand the fundamental performance limits imposed by the underwater medium. For a full characterization of underwater light propagation, Radiative Transfer Equation (RTE) [44, Chapter 9] can be used. RTE involves integro-differential equation which does not yield a general analytical solution [45]. Approximate analytical solutions to RTE have been further proposed [46–48]. These, however, build upon various simplifying assumptions and the predicted irradiances are typically accurate to a few tens of percent at best, and can be off by an order of magnitude.

As an alternative, ray-tracing simulations [30–37] are widely adopted in the literature to characterize the channel. In ray tracing, numerous photons are statistically generated based on the source pattern and traced until the receiver simulating the interactions of each photon with the underwater medium. For a given number of rays and the number of scattering events, the received power and associated path lengths for each ray are computed to obtain the channel impulse response. These simulations are capable to provide a realistic underwater channel model, but their computational complexity is very large. Furthermore, as a numerical method, they provide limited insight into system design parameters.

The lack of a generic RTE solution and the complexity of simulations become a main motivation to obtain closed-form path loss ratio expressions. The Beer-Lambert formula [49] is widely used in the literature to calculate underwater path loss. However, it overestimates the path loss since it ignores the possibility of receiving scattered photons. To consider the effect of scattering, a modified version of Beer-Lambert formula based on a weighted function of two exponential terms is proposed in [40]. One of these terms determines the attenuation for path lengths less than the diffusion length (i.e., the longest distance that a photon could travel theoretically [50]) while the other term is associated with path lengths greater than the diffusion length. The four weighting coefficients in this formulation are found via data fitting to simulation data. The expression in [40] provides a good match to simulation results but is a function of only distance and does not explicitly reflect the dependence of system parameters and water type.

Very recently, a novel closed-form path loss ratio expression was proposed which modifies the well-known and commonly adopted Beer-Lambert formula [11]. This formula introduced an additional term proportional to the geometrical propagation of the light source in the negative exponential coefficient. This term determines the volume of the scattered rays that might be received by the detector. Unlike the formulation in [40], the proposed expression is an explicit function of beam divergence angle, receiver aperture diameter and extinction coefficient (i.e., water type).

1.3.2 Underwater Optical Turbulence

In addition to the path loss that we discussed in Section 1.3, UOT introduces instantaneous fluctuations over the average received power [15]. This is as a result of the changes in the refractive index of seawater. The underwater environment can be modeled as an inhomogeneous medium with multi-homogeneous cells, also known as eddies or turbulent cells, each with a different refractive index. If the size of the eddy is larger than or comparable in size to the beam diameter, the optical beam bends as a whole effectively resulting in the unsteady tilt of the beam (i.e., beam jitter). If the size of the eddy is smaller than optical beam diameter, ray bending and diffraction cause distortions in the optical beam [51].

The statistical distribution of underwater fading was investigated experimentally in [10, 52–55]. LN and Gamma-Gamma (GG) Probability Density Function (PDF) were shown to match the measurement results [52, 54, 55] respectively for weak and moderate/strong turbulence. The performance of UVLC systems over LN and GG turbulence channels was investigated in [5, 6, 16, 56–59]. A common underlying assumption in these works is fixed turbulence strength through the transmission range which can be justified only for horizontal links. In vertical links, the gradient of temperature and salinity changes with depth [60]. This effectively results in ocean stratification, i.e., water with different values of salinity and temperature form non-mixing layers [61]. Extensive measurements performed in the Pacific Ocean showed that strong stratification prevailed in 35% of the cases [62]. Similarly, measurements in the Weddell Sea reveal that the surface layer is separated from the deep ocean by numerous layers [63]. Each of these layers has a thickness which typically varies between few meters to tens of meters [64, 65].

1.4 Dissertation Outline

The dissertation has five main parts that can be outlined as follow

1. In the first part of this thesis, we use the newly proposed closed-form expression for the underwater optical channel coefficient in order to determine the maximum achievable link distance for different water types assuming point-to-point link. Then, we investigate extending the distance by the deployment of underwater relay-assisted systems. Particularly, we determine the maximum achievable distance for a given number of hops to satisfy a targeted end-to-end BER assuming the deployment of both Detect-and-Forward (DF) and Amplify-and-Forward (AF) relaying schemes. Then, we investigate the benefits of link adaptation in the context of OFDM-based

underwater Visible Light Communication (VLC) systems considering two adaptive algorithms, which aim to maximize the throughput while satisfying a pre-defined targeted BER target.

2. In the second part of this thesis, we propose a novel simplified spatial power spectrum model of underwater turbulent fluctuations as an explicit function of eddy diffusivity ratio. We use the proposed model for investigating the effect of eddy diffusivity on scintillation index of optical plane and spherical waves and compare the results with the previous works that have built on an inaccurate assumption of unit eddy diffusivity ratio. Next, we discuss horizontal and vertical UVLC turbulence channels and demonstrate that in a vertical UVLC link, water with different values of salinity and temperature form non-mixing layers due to ocean stratification and statistically characterize the cascaded channel.

3. In the third part of this thesis, we use our proposed cascaded LN and GG turbulence channels, respectively, for the case of weak and moderate/strong turbulence conditions and derive closed-form expressions for the BER performance of vertical links. We further analyze the asymptotic behavior of BER and determine the diversity gains. In addition, we derive closed-form expressions for Ergodic capacity and investigate the effect of layering on the achievable capacity.

4. In the fourth part of this thesis, we consider two fading mitigation techniques to mitigate turbulence-induced intensity fluctuations, i.e., signal fading. The techniques we consider are Multiple-Input Multiple-Output (MIMO) and Generalized Transmit Laser Selection (GTLS). We first consider MIMO UVLC system over LN turbulence channels, derived a novel closed-form BER expression, introduced the concept of IDO and quantified the achievable IDO as a function of the number of laser sources, the number of photo-detectors and the variance of the log-amplitude coefficient. In an effort to reduce the hardware complexity, we consider the use of TLS in the context

of UVLC. Since feedback error or outdated selection due to temporal changes in the channel may result in selecting another source rather than the best one, we consider an UVLC system with GTLS where single source, unnecessarily the best, is selected among the available lasers and determined the achievable IDO.

5. In the fifth part of this thesis, we consider the design of a multiple access system. We first consider the downlink of a USN where the system is built upon OFDMA-based VLC. We proposed an adaptive algorithm which aims to maximize the overall data rate subject to maintaining identical data rate for each underwater sensor node while satisfying a predefined maximum acceptable BER. In the second part of this chapter, we considered NOMA in the context of USN and derive a simple closed-form expression for the NOMA capacity as well as a simple and accurate asymptotic representation of the achievable capacity.

1.5 Organization

The dissertation is organized as follow. Chapter 2 focuses on the performance of UVLC system in the absence of turbulence, which can be considered as an ideal benchmark in the following chapters, Chapter 3 focuses on turbulence channel modeling, Chapter 4 focuses on investigating the performance of UVLC system in the presence of turbulence, Chapter 5 focuses on investigating the performance of different fading mitigation techniques. To this end, work is limited to a single-user case. Therefore, Chapter 6 focuses on the design of multiple access systems. These chapters are organized as follow:

- Chapter 2 has three sections. In Section 2.2, we formulate a closed-form expression for maximum achievable distance as a function of system and channel parameters. In Section 2.3, we investigate the performance of UVLC systems with DF and AF relaying. First, we determine the optimal placement of relay in a dual-hop serial relaying system based on minimizing BER. Then, we present a closed-form expression for maximum achievable distance in a multi-hop serial relaying system. In Section 2.4, we investigate the benefits of link adaptation in the context of OFDM-based UVLC systems.

- Chapter 3 has two sections. In Section 3.2, we discuss the spatial power spectrum model of turbulent fluctuations of the sea-water refraction index. In Section 3.3, we discuss the horizontal and vertical UVLC turbulence channels demonstrating that vertical link can be presented as a concatenation of multiple non-mixing layers and statistically characterize the cascaded channel.

- Chapter 4 is organized as follow. We derive closed-form expressions for the BER performance of vertical UVLC system described in Section 3.3.2 based on the cascaded LN (see Section 3.3.2.1) and GG (see Section 3.3.2.2) distributions respectively for weak and moderate/strong turbulence conditions. Then, we analyze the asymptotic BER performance and determine the diversity orders. In addition, we derive closed-form expressions for the average Ergodic capacity of underwater cascaded fading channels under consideration.

- Chapter 5 has two sections. In Section 5.2, we consider a MIMO UVLC system over LN channels, derive a novel closed-form BER expression, introduce the concept of IDO and quantify IDO. In Section 5.3, we consider an UVLC system with GTLS where the n^{th} best laser is selected among the available N lasers and determine the so-called IDO.

- Chapter 6 has two sections. In Section 6.2, we introduce the use of adaptive OFDMA in the context of UVLC systems. The adaptive system is formulated such that the overall data rate is maximized subject to two constraints: identical user's data rate and BER of each user not exceeding a pre-defined maximum BER. In Section 6.3, we consider NOMA in the context of USN and investigate the achievable NOMA capacity.

CHAPTER II

PERFORMANCE ANALYSIS OF UVLC SYSTEMS

2.1 Introduction

In this chapter, we investigate the performance limits of UVLC system, i.e., we study the performance of UVLC in the absence of turbulence that can be considered as an ideal benchmark. Therefore, we first derive in this chapter the maximum achievable link distance to achieve a specified BER in the pure sea, clear ocean, coastal water and harbor water based on the closed-form path loss ratio expression of the UVLC provided in [11, Eq. (6)].

Our results demonstrate that the maximum achievable distance is limited to a few tens of meters. This necessitates the deployment of relay-assisted UVLC systems to extend the transmission range. We consider both DF and AF relaying. For each relaying method, we first consider a dual-hop UVLC system and determine optimal relay placement to minimize the BER. Then, we consider a multi-hop system with equidistant relays and determine the maximum achievable distance for a given number of hops to satisfy a targeted end-to-end BER.

Distance is not the only challenge. UVLC is needed to achieve high data rates sufficiently high for real-time image and video transmission. Such high data rates over underwater channels with frequency-selectivity necessitate the use of efficient multi-carrier techniques such as OFDM. Therefore, we consider an adaptive DC-Biased Optical (DCO)-OFDM UVLC system. The design of the adaptive algorithm is formulated to maximize the throughput under error rate performance constraints. The receiver first calculates the SNR per each subcarrier. Then, based on SNR information, it determines which subcarrier should be loaded first and selects the maximum constellation size for each subcarrier while satisfying a predefined targeted BER.

The rest of this chapter is organized as follow. In Section 2.2, we formulate a closed-form expression for maximum achievable distance as a function of system and channel parameters. In Section 2.3, we investigate the performance of UVLC systems with DF and AF relaying. First, we determine the optimal placement of relay in a dual-hop serial relaying system based on minimizing BER. Then, we present a closed-form expression for maximum achievable distance in a multi-hop serial relaying system. In Section 2.4, we investigate the benefits of link adaptation in the context of OFDM-based UVLC systems.

2.2 *Maximum Achievable Distance- Single Hop*

In this section, we derive a closed-form expression for the maximum achievable distance for a point-to-point UVLC link. For this purpose, we firstly propose an accurate closed-form expression for the underwater path loss ratio and solve it for distance [11]. We then use our derived expression for investigating the maximum achievable link distance to achieve a predefined maximum acceptable BER in different water types: pure sea, clear ocean, coastal water and harbor water.

The proposed closed-form path loss ratio expression modifies the well-known commonly used Beer-Lambert formula such that an additional term proportional to the geometrical propagation of the light source is introduced in the negative exponential coefficient. This is due to the fact that, in practice, the detector can receive the rays after multiple scattering. In other words, the additional term that we propose determines the volume of the scattered rays that might be received by the detector. Furthermore, the proposed expression is the first expression that is an explicit function of beam divergence angle, receiver aperture diameter and extinction coefficient (i.e., water type). Let h denote the optical path loss measured on a linear scale (i.e., optical channel coefficient), we express h as

$$h \approx \left(\frac{D_{\mathrm{R}}}{\theta_F d}\right)^2 \exp\left(-cd\left(\frac{D_{\mathrm{R}}}{\theta_F d}\right)^T\right). \tag{2.1}$$

where θ_F and D_{R} denote full-width transmitter beam divergence angle and receiver aperture diameter, respectively. In Eq. (2.1), c and T represent correction and extinction coefficients, which are both water type dependent (see Table 2).

Table 2: Configurations under consideration.

Configuration		System Parameters	T
1	**Effect of receiver aperture diameter**	$\theta_{\mathrm{F}}=6^{\circ}$, $D_{\mathrm{R}}=5\,\mathrm{cm}$, $FOV=180^{\circ}$	0.13
2		$\theta_{\mathrm{F}}=6^{\circ}$, $D_{\mathrm{R}}=10\,\mathrm{cm}$, $FOV=180^{\circ}$	0.16
3		$\theta_{\mathrm{F}}=6^{\circ}$, $D_{\mathrm{R}}=20\,\mathrm{cm}$, $FOV=180^{\circ}$	0.21
4		$\theta_{\mathrm{F}}=6^{\circ}$, $D_{\mathrm{R}}=30\,\mathrm{cm}$, $FOV=180^{\circ}$	0.26
5		$\theta_{\mathrm{F}}=6^{\circ}$, $D_{\mathrm{R}}=40\,\mathrm{cm}$, $FOV=180^{\circ}$	0.31
6		$\theta_{\mathrm{F}}=6^{\circ}$, $D_{\mathrm{R}}=50\,\mathrm{cm}$, $FOV=180^{\circ}$	0.37
7	**Effect of beam divergence angle**	$\theta_{\mathrm{F}}=6^{\circ}$, $D_{\mathrm{R}}=20\,\mathrm{cm}$, $FOV=180^{\circ}$	0.21
8		$\theta_{\mathrm{F}}=12^{\circ}$, $D_{\mathrm{R}}=20\,\mathrm{cm}$, $FOV=180^{\circ}$	0.24
9		$\theta_{\mathrm{F}}=18^{\circ}$, $D_{\mathrm{R}}=20\,\mathrm{cm}$, $FOV=180^{\circ}$	0.25
10	**Effect of field of view**	$\theta_{\mathrm{F}}=6^{\circ}$, $D_{\mathrm{R}}=5\,\mathrm{cm}$, $FOV=60^{\circ}$	0.13
11		$\theta_{\mathrm{F}}=6^{\circ}$, $D_{\mathrm{R}}=5\,\mathrm{cm}$, $FOV=120^{\circ}$	0.13
12		$\theta_{\mathrm{F}}=6^{\circ}$, $D_{\mathrm{R}}=5\,\mathrm{cm}$, $FOV=180^{\circ}$	0.13

To solve Eq. (2.1) on the preceding page for d, we first need to multiply both sides by $\theta_{\mathrm{F}}^2/D_{\mathrm{R}}^2$ and then raise both sides to the power of $(T-1)/2$. If both sides of the resulting expressions are multiplied by $(1-T)\left(cD_{\mathrm{R}}^T/2\theta_F^T\right)$, we obtain

$$(1-T)\left(\frac{c}{2}\frac{D_{\mathrm{R}}^T}{\theta_F^T}\right)d^{(1-T)}e^{(1-T)\left(\frac{c}{2}\frac{D_{\mathrm{R}}^T}{\theta_F^T}\right)d^{(1-T)}}=(1-T)\left(\frac{c}{2}\frac{D_{\mathrm{R}}^T}{\theta_F^T}\right)\left(\frac{h\theta_F^2}{D_{\mathrm{R}}^2}\right)^{\left(\frac{T-1}{2}\right)}. \tag{2.2}$$

The left-hand side of Eq. (2.2) is in the form of (xe^x) whose inverse can be taken by the Lambert-W function, i.e., $\mathrm{W}(xe^x)=x$ [66]. We take the Lambert-W function for both sides of Eq. (2.2) and divide the resulting expression by $\left(cD_{\mathrm{R}}^T(1-T)\right)/(2\theta_{\mathrm{F}}^T)$. Then, by raising both sides to the power of $1/(1-T)$, transmission distance is obtained as

$$d=\left[\frac{\mathrm{W}\left(\frac{c}{2}(1-T)\left(\frac{D_{\mathrm{R}}}{\theta_{\mathrm{F}}}\right)h^{\left(\frac{T-1}{2}\right)}\right)}{\frac{c}{2}(1-T)\left(\frac{D_{\mathrm{R}}}{\theta_{\mathrm{F}}}\right)^T}\right]^{\frac{1}{1-T}}. \tag{2.3}$$

Let BER_{target} denote the targeted BER. Assume that the required SNR to achieve BER_{target} is given by SNR_{req}. The relationship between BER_{target} and SNR_{req} depends on the deployed system architecture and modulation type which are dictated by the channel characteristics. Let B_s and τ_d respectively denote the data rate and channel delay spread. A channel is classified as frequency-selective for $B_s\tau_d \geq 1$. If $B_s\tau_d \approx 1$, then it is classified as frequency-flat channel [67]. Underwater optical channels exhibit frequency selectivity only for data rates higher than hundreds of Mb/s.

In such cases, multicarrier communication in the form of OFDM is employed to deal with the resulting intersymbol interference. Otherwise, for most practical purposes, single-carrier systems with simple modulation techniques such as On-Off Keying (OOK) can be used. The BER for OOK over real Additive White Gaussian Noise (AWGN) channel is given by [68]

$$BER = Q\left(\sqrt{\frac{SNR}{2}}\right), \tag{2.4}$$

where average SNR is defined as

$$SNR = \frac{\eta^2 r^2 h^2 P_{\text{te}}}{\sigma_n^2}. \tag{2.5}$$

In Eq. (2.5), P_{te} is average electrical transmit power, η is the electrical to optical conversion efficiency of a laser diode, r is the photodetector responsivity and σ_n^2 is the noise variance. Based on Eq. (2.4), SNR_{req} that satisfies a given target BER of BER_{target} can be expressed as

$$SNR_{\text{req}} = 2\left(Q^{-1}\left(BER_{\text{target}}\right)\right)^2. \tag{2.6}$$

Based on Eq. (2.5) and Eq. (2.6), the required h value to achieve BER_{target} can be obtained. By replacing the resulting expression in Eq. (2.3) on the previous page, the maximum achievable link distance to achieve the BER_{target} for OOK is found as

$$d_{\max} = \left[\frac{\mathrm{W}\left(\frac{c}{2}(1-T)\left(\frac{D_{\text{R}}}{\theta_F}\right)\left(\sqrt{\frac{2\sigma_n^2}{r^2\eta^2 P_{\text{te}}}}Q^{-1}\left(BER_{\text{target}}\right)\right)^{\left(\frac{T-1}{2}\right)}\right)}{\frac{c}{2}(1-T)\left(\frac{D_{\text{R}}}{\theta_F}\right)^T}\right]^{\frac{1}{1-T}}. \tag{2.7}$$

In the following, we present numerical results for different system and channel parameters. Unless otherwise stated, we assume a receiver aperture diameter of $D_{\mathrm{R}} = 5$ cm, transmitter beam divergence angle of $\theta_{\mathrm{F}} = 6°$, average electrical transmit power of $P_{\mathrm{te}} = 10$ dBm, noise power of $\sigma_n^2 = -100$ dBm, electrical to optical conversion efficiency of η = 0.5 [69] and photodetector responsivity of $r = 0.28$ A/W [68].

First, we investigate the maximum achievable distance in different water types for $\theta_F = 6°$, $D_R = 5$ cm, $FOV = 180°$. In Figure 1, we present the achievable distance versus the targeted BER for pure sea, clear ocean, coastal water and harbor water [30]. It is observed from Figure 1 that a transmission range of 21.33 m is possible for pure sea at $BER_{\mathrm{target}} = 10^{-6}$ while it decreases to 15.02 m, 11.82 m and 4.04 m for clear ocean, coastal water and harbor water, respectively. It is due to the fact that the optical beam has more attenuation through the turbid water. It is also observed that by decreasing the targeted BER, the maximum achievable distance decreases. For example, at $BER_{\mathrm{target}} = 10^{-9}$ the maximum achievable distances in pure sea, clear ocean, coastal water and harbor water are respectively 19.81 m, 14.11 m, 11.15 m and 3.86 m.

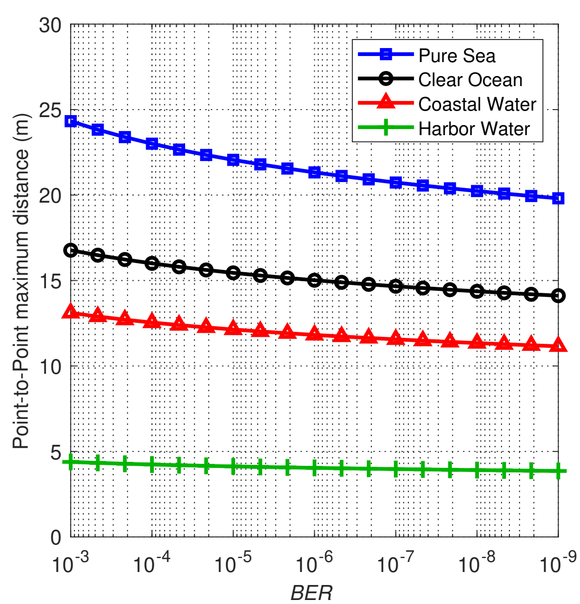

Figure 1: Effect of water type on maximum achievable distance in point-to-point system.

Second, we investigate the effect of receiver aperture size on the maximum achievable distance. We assume coastal water as an example. It is observed from Figure 2 that as receiver aperture size increases, the maximum achievable distance increases since the larger receiver aperture size collects more energy. For example, the maximum achievable distance in coastal water at $BER_{\text{target}} = 10^{-6}$ is 11.82 m for $D_{\text{R}} = 5$ cm. This climbs to 16.16 m, 21.53 m, 25.57 m for $D_{\text{R}} = 10$ cm, $D_{\text{R}} = 20$ cm and $D_{\text{R}} = 30$ cm, respectively.

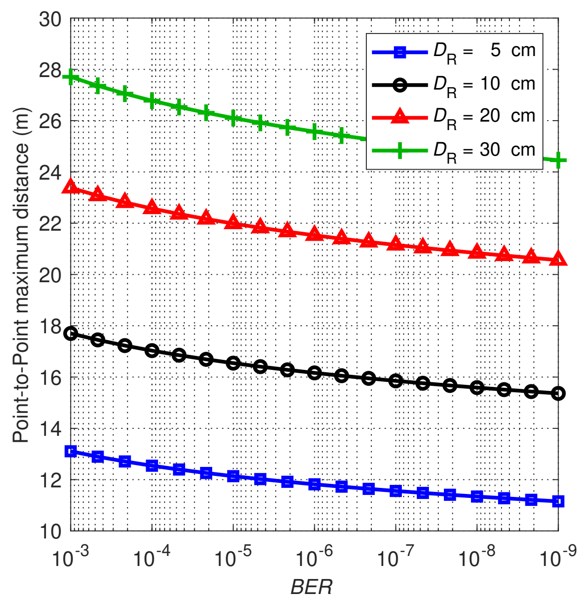

Figure 2: Effect of receiver aperture sizes on maximum achievable distance in coastal water for point-to-point system.

Third, we investigate the effect of the transmitter beam divergence angle on the maximum achievable distance. We assume a receiver aperture diameter of $D_{\text{R}} = 20$ cm. Coastal water is assumed. It is observed from Figure 3 on the next page that as transmitter divergence angle decreases, the maximum achievable distance increases. This is a result of the fact that the focused beam has less attenuation through the water medium. For example, the maximum achievable distances in coastal water at $BER_{\text{target}} = 10^{-6}$ is 16.74 m for $\theta_{\text{F}} = 18^{\circ}$. This climbs to 18.93 m and 21.53 m for $\theta_F = 12^{\circ}$ and $\theta_{\text{F}} = 6^{\circ}$, respectively.

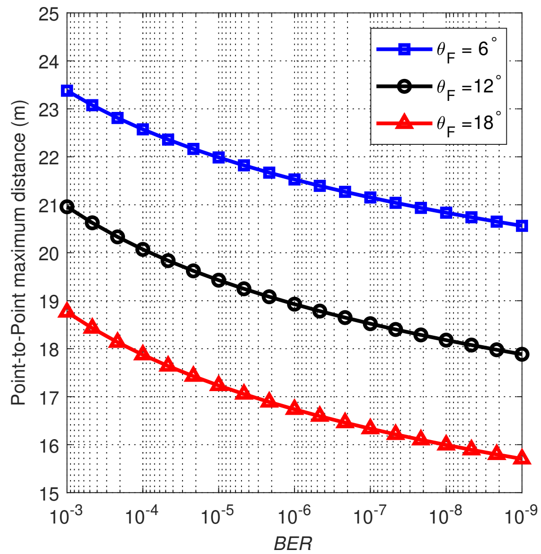

Figure 3: Effect of beam divergence angle on maximum achievable distance in coastal water for point-to-point system.

2.3 Maximum Achievable Distance-Multi Hop

In Section 2.2, we derived the maximum achievable link distance for a point-to-point communication link. Numerical results revealed that in underwater environments, the strength of an optical signal falls severely with propagation distance and maximum achievable distance for an uncoded UVLC system is limited to a few tens of meters[1]. In this section, we explore the deployment of relay-assisted transmission to extend transmission range. We consider both DF and AF relaying. For each relaying type, we first consider a dual-hop relaying system and determine optimal relay placement to minimize BER. Then, we consider a multi-hop system and determine the maximum achievable distance for a given number of hops to satisfy a targeted end-to-end BER. While the achievable distances for multi-hop RF systems were studied in the literature [70, 71], no such work on UVLC systems has been reported before.

[1]Some improvement in the error rate performance can be obtained through coding gain if forward error correction techniques are employed. Such improvements can be further traded for extension of transmission range.

2.3.1 Decode and Forward

Let N denote the number of relay terminals. Let h_i denote the optical channel coefficient for the i^{th} hop, $i = 1, \cdots, N+1$. Under the assumption of OOK signaling, the end-to-end (i.e., source-to-destination) BER for a DF serial relaying system is given by[2] [42]

$$\begin{aligned} BER_{\text{SD}} &= 1 - \prod_{i=1}^{N+1} \left(1 - BER_{\text{i}}\right) \\ &= 1 - \prod_{i=1}^{N+1} \left(1 - Q\left(\sqrt{\frac{r^2\eta^2 h_{\text{i}}^2}{2\sigma_n^2}\left(\frac{P_{\text{te}}}{N+1}\right)}\right)\right), \end{aligned} \tag{2.8}$$

where BER_{i} is the BER of the i^{th} hop.

In the following, we assume the deployment of a single relay (i.e., $N = 1$) and study the optimal placement of the relay for the dual-hop system to minimize the end-to-end BER. For a dual-hop system, Eq. (2.8) reduces to

$$\begin{aligned} BER_{\text{SD}} =& Q\left(\sqrt{\frac{r^2\eta^2 h_1^2 P_{\text{te}}}{4\sigma_n^2}}\right) + Q\left(\sqrt{\frac{r^2\eta^2 h_2^2 P_{\text{te}}}{4\sigma_n^2}}\right) \\ & - Q\left(\sqrt{\frac{r^2\eta^2 h_1^2 P_{\text{te}}}{4\sigma_n^2}}\right) Q\left(\sqrt{\frac{r^2\eta^2 h_2^2 P_{\text{te}}}{4\sigma_n^2}}\right). \end{aligned} \tag{2.9}$$

The last term in Eq. (2.9) involves the multiplication of two small values and can be ignored for most practical purposes [72]. Using the approximation $Q(x) \approx (1/12)\exp\left(-x^2/2\right) + (1/4)\exp\left(-2x^2/3\right)$ [73], we have

$$\begin{aligned} BER_{\text{SD}} \approx& \frac{1}{12}\exp\left(-\frac{r^2\eta^2 h_1^2 P_{\text{te}}}{8\sigma_n^2}\right) + \frac{1}{4}\exp\left(-\frac{r^2\eta^2 h_1^2 P_{\text{te}}}{6\sigma_n^2}\right) \\ & + \frac{1}{12}\exp\left(-\frac{r^2\eta^2 h_2^2 P_{\text{te}}}{8\sigma_n^2}\right) + \frac{1}{4}\exp\left(-\frac{r^2\eta^2 h_2^2 P_{\text{te}}}{6\sigma_n^2}\right). \end{aligned} \tag{2.10}$$

[2] In the derivation of Eq. (2.8), it is assumed that a bit can correctly be detected at the destination if and only if all of the relay terminals perform detection without an error [42]. This implicitly assumes sufficiently high SNR values per each hop.

Let $D = d_1 + d_2$ denote the distance between source and destination where d_1 and d_2 denote respectively the distances of source-to-relay and relay-to-destination links. Replacing Eq. (2.1) on page 14 in Eq. (2.10) on the preceding page, BER_{SD} can be then written as

$$BER_{\mathrm{SD}} \approx f\left(d_1\right) + g\left(d_1\right) + f\left(D - d_1\right) + g\left(D - d_1\right), \tag{2.11}$$

where $f\left(d_{\mathrm{i}}\right)$ and $g\left(d_{\mathrm{i}}\right)$ are respectively given as

$$f\left(d_{\mathrm{i}}\right) = \frac{1}{12}\exp\left(-\frac{P_{\mathrm{te}}r^2\eta^2}{8\sigma_n^2}\left(\frac{D_{\mathrm{R}}}{\theta_F}\right)^4 d_{\mathrm{i}}^{-4} e^{-2c\left(\frac{D_{\mathrm{R}}}{\theta_F}\right)^T d_{\mathrm{i}}^{1-T}}\right), \tag{2.12}$$

$$g\left(d_{\mathrm{i}}\right) = \frac{1}{4}\exp\left(-\frac{P_{\mathrm{te}}r^2\eta^2}{6\sigma_n^2}\left(\frac{D_{\mathrm{R}}}{\theta_F}\right)^4 d_{\mathrm{i}}^{-4} e^{-2c\left(\frac{D_{\mathrm{R}}}{\theta_F}\right)^T d_{\mathrm{i}}^{1-T}}\right). \tag{2.13}$$

To obtain d_1 in Eq. (2.11) that minimizes BER_{SD}, we take the derivative of Eq. (2.11) and set it to zero, i.e.,

$$\psi\left(d_1\right) + \phi\left(d_1\right) - \psi\left(D - d_1\right) - \phi\left(D - d_1\right) = 0\cdot \tag{2.14}$$

In Eq. (2.14), $\psi\left(d_{\mathrm{i}}\right)$ and $\phi\left(d_{\mathrm{i}}\right)$ are respectively given as

$$\psi\left(d_{\mathrm{i}}\right) = F\exp\left(\frac{1}{4}Fd_{\mathrm{i}}^{-4}e^{Gd_{\mathrm{i}}^{1-T}}\right)\left(-4d_{\mathrm{i}}^{-5}e^{Gd_{\mathrm{i}}^{1-T}} + (1-T)\,d_{\mathrm{i}}^{-4-T}Ge^{Gd_{\mathrm{i}}^{1-T}}\right), \tag{2.15}$$

$$\phi\left(d_{\mathrm{i}}\right) = 4F\exp\left(\frac{1}{3}Fd_{\mathrm{i}}^{-4}e^{Gd_{\mathrm{i}}^{1-T}}\right)\left(-4d_{\mathrm{i}}^{-5}e^{Gd_{\mathrm{i}}^{1-T}} + (1-T)\,d_{\mathrm{i}}^{-4-T}Ge^{Gd_{\mathrm{i}}^{1-T}}\right), \tag{2.16}$$

where $F = -\left(P_{\mathrm{te}}r^2\eta^2/2\sigma_n^2\right)\left(D_{\mathrm{R}}/\theta_{\mathrm{F}}\right)^4$ and $G = -2c\left(D_{\mathrm{R}}/\theta_{\mathrm{F}}\right)^T$. It is obvious that the solution of Eq. (2.14) is obtained when the consecutive hops are placed equidistant, i.e., $d_1 = d_2$.

In the following, we consider a multi-hop DF relaying system with equidistant placement of relays. We determine the maximum achievable distance for a given number of hops to satisfy a targeted end-to-end BER. Since relay nodes are located equidistant from each other, the channel coefficients of all hops are the same, i.e., $h_i = h_{hop}$, $i = 1, \cdots, N+1$. Therefore, the average BER of each hop is also identical, i.e., $BER_i =$

BER_{hop}, $i = 1, \cdots, N+1$. Replacing this in Eq. (2.8) on page 20, we obtain the end-to-end BER as

$$BER_{\mathrm{SD}} = 1 - \left(1 - BER_{\mathrm{hop}}\right)^{N+1}. \tag{2.17}$$

Noting that $\ln(1+x) \approx x$ for small x [74], we obtain BER_{hop} as

$$BER_{\mathrm{hop}} \approx \frac{BER_{\mathrm{SD}}}{(N+1)}. \tag{2.18}$$

Assume that we want to achieve $BER_{\mathrm{SD,target}}$ for end-to-end BER. This indicates that $BER_{\mathrm{hop,target}} = BER_{\mathrm{SD,target}}/(N+1)$ should be satisfied per hop. Utilizing Eq. (2.8) on page 20, the required h_{hop} value to achieve $BER_{\mathrm{hop,target}}$ can be obtained. By replacing the resulting expression in Eq. (2.3) on page 15, the maximum achievable distance per hop is calculated. Multiplying this with $(N+1)$, we obtain the maximum achievable distance for multi-hop system as

$$\begin{aligned} d_{\mathrm{max,DF}} &= (N+1) \\ &\times \left[\frac{\mathrm{W}\left(\frac{c}{2}(1-T)\left(\frac{D_{\mathrm{R}}}{\theta_F}\right) \left(\sqrt{\frac{2(N+1)\sigma_n^2}{r^2\,\eta^2 P_{\mathrm{te}}}}\, Q^{-1}\left(\frac{BER_{\mathrm{SD,target}}}{(N+1)}\right)\right)^{\left(\frac{T-1}{2}\right)}\right)}{\frac{c}{2}(1-T)\left(\frac{D_R}{\theta_{1/e}}\right)^{T}} \right]^{\frac{1}{1-T}}. \end{aligned} \tag{2.19}$$

2.3.2 Amplify and Forward

In AF relaying, the relay terminal amplifies and retransmits the signal without performing any detection. Minimization of end-to-end BER in AF relaying is equivalent to maximizing end-to-end SNR [75]. Under the assumption of sufficiently large SNR per hop, an approximation for end-to-end SNR is given by [76]

$$SNR_{\mathrm{SD}} \approx \left(\sum_{i=1}^{N+1} \frac{1}{SNR_{\mathrm{i}}} \right)^{-1}, \tag{2.20}$$

where SNR_{i} is the SNR of the i^{th} hop, $i = 1, \cdots, N+1$. Similar to Section 2.3.1, first assume the deployment of a single relay, i.e., $N=1$. For a dual-hop AF system, Eq. (2.20) reduces to

$$SNR_{\mathrm{SD}} \approx \frac{SNR_1 SNR_2}{SNR_1 + SNR_2} = \frac{\eta^2 r^2 P_{\mathrm{te}}}{2\sigma_n^2}\left(\frac{h_1^2 h_2^2}{h_1^2 + h_2^2}\right). \tag{2.21}$$

Replacing Eq. (2.1) on page 14 in Eq. (2.21), SNR_{SD} can be written as

$$SNR_{\mathrm{SD}} = \Upsilon \frac{\zeta(d_1)\,\zeta(D-d_1)}{\zeta(d_1)+\zeta(D-d_1)}, \tag{2.22}$$

where $\zeta(d_i)$ and Υ are respectively given as

$$\zeta(d_i) = d_i^{-4} e^{-2c\left(\frac{D_{\mathrm{R}}}{\theta_F}\right)^T d_i^{1-T}}, \tag{2.23}$$

$$\Upsilon = \frac{\eta^2 r^2 P_{\mathrm{te}}}{2\sigma_n^2}\left(\frac{D_{\mathrm{R}}}{\theta_F}\right)^4. \tag{2.24}$$

To determine d_1 in Eq. (2.22) that maximizes SNR_{SD}, we take the derivative of Eq. (2.22) and set it to zero, i.e.,

$$\begin{aligned}&\Big(\wp(d_1)\,\zeta(D-d_1) - \wp(D-d_1)\,\zeta(d_1)\Big)\left(\zeta(d_1)+\zeta(D-d_1)\right)\\ &-\Big(\wp(d_1)-\wp(D-d_1)\Big)\zeta(d_1)\,\zeta(D-d_1) = 0,\end{aligned} \tag{2.25}$$

where $\wp(d_i)$ is given as

$$\wp(d_i) = -4d_i^{-5} e^{-2c\left(\frac{D_{\mathrm{R}}}{\theta_{\mathrm{F}}}\right)^T d_i^{1-T}} - 2c(1-T)\left(\frac{D_{\mathrm{R}}}{\theta_{\mathrm{F}}}\right)^T d_i^{-4-T} e^{-2c\left(\frac{D_{\mathrm{R}}}{\theta_{\mathrm{F}}}\right)^T d_i^{1-T}}. \tag{2.26}$$

It can be easily verified that the solution of Eq. (2.25) is obtained for $d_1 = d_2$. This indicates that, similar to DF relaying, the best performance is attained when relays are placed equidistant.

Now consider a multi-hop AF relaying system. Under the assumption that relay nodes are located equidistant from each other, the SNR of each hop is identical, i.e., $SNR_i = SNR_{hop}$, $i = 1, \cdots, N+1$. Replacing this in Eq. (2.20) on the preceding page, we obtain the end-to-end SNR as

$$SNR_{\mathrm{SD}} \approx \frac{SNR_{\mathrm{hop}}}{(N+1)} = \frac{\eta^2 r^2 h_{\mathrm{hop}}^2 P_{\mathrm{te}}}{\sigma_n^2 (N+1)^2}. \tag{2.27}$$

Utilizing Eq. (2.6) on page 16, the required end-to-end SNR to achieve $BER_{\mathrm{SD,target}}$ is obtained. This can be then used to obtain the required h_{hop} value. By replacing the resulting expression in Eq. (2.3) on page 15, the maximum achievable distance for multi-hop AF relaying system is calculated as

$$d_{\mathrm{max,AF}} = (N+1) \times \left[\frac{\mathrm{W}\left(\frac{c}{2}(1-T)\left(\frac{D_{\mathrm{R}}}{\theta_{\mathrm{F}}}\right)\left(\sqrt{\frac{2\sigma_n^2 (N+1)^2}{\eta^2 r^2 P_{\mathrm{te}}}} Q^{-1}\left(BER_{\mathrm{SD,target}}\right)\right)^{\left(\frac{T-1}{2}\right)} \right)}{\frac{c}{2}(1-T)\left(\frac{D_{\mathrm{R}}}{\theta_{\mathrm{F}}}\right)^{T}} \right]^{\frac{1}{1-T}}. \tag{2.28}$$

2.3.3 Results and Discussions

In this sub-section, we demonstrate how much extension in transmission distance is possible through the deployment of multi-hop system. Unless otherwise stated, we assume targeted BER of $BER_{\mathrm{SD,target}} = 10^{-6}$, receiver aperture diameter of $D_{\mathrm{R}} = 5$ cm, transmitter beam divergence angle of $\theta_{\mathrm{F}} = 6^{\circ}$, average electrical transmit power of $P_{\mathrm{te}} =10$ dBm, noise power of $\sigma_n^2 = -100$ dBm, electrical to optical conversion efficiency of $\eta = 0.5$ and photodetector responsivity of $r = 0.28$ A/W.

In Figure 4 on the next page, we present the maximum achievable distance versus the number of relay terminals for different water types. The case of $N = 0$, i.e., direct transmission, is also included as a benchmark. The maximum achievable distances for pure sea, clear ocean, coastal water and harbor water for $N = 0$ are, respectively, 21.33 m, 15.02 m, 11.82 m and 4.04. Assuming the deployment of a single DF relay, i.e., $N =1$, these increase to 37.83 m, 27.15 m, 21.51 m and 7.50 m while they respectively increase to 151.80 m, 114.40 m, 92.42 m and 34.04 m with the deployment of $N = 10$ relays. On the other hand, for AF relaying with $N = 10$, we have achievable distances of 99.71 m, 79.89 m, 66.33 m and 26.45 m which are significantly lower than those of its DF counterpart.

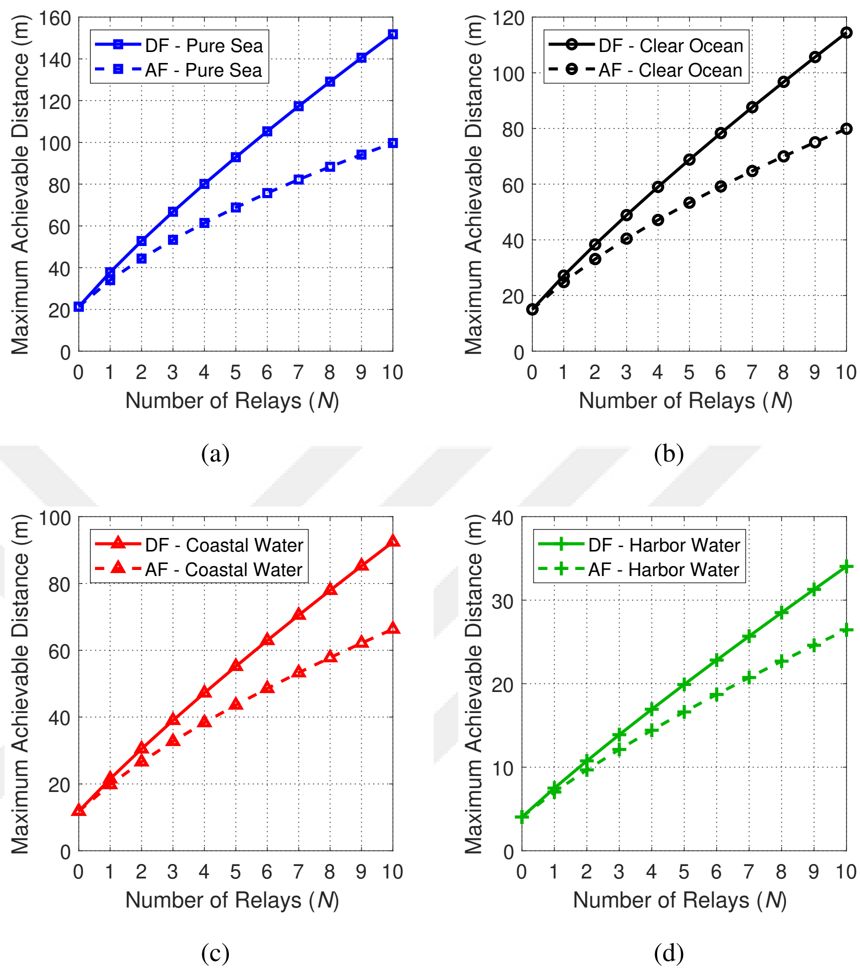

Figure 4: Maximum achievable distance versus number of relays in different water types.

It is clear from Figure 4 that a linear increase in transmission distance with respect to the number of hops is not obtained. To better illustrate this, we plot the improvement factor, i.e., $d_{\text{multi-hop}}/d_{\max}$, in Figure 5 on the next page for different water types. As an example, we consider pure sea. For DF relaying, the improvement factors at $N = 1$, 5 and 10 are respectively 1.77, 4.36 and 7.12. These further decrease to 1.6, 3.23 and 4.68 for AF relaying. These are smaller than the ideal improvement factor of $(N+1)$. It can be further noted that the improvement factor is dependent on the water type and slightly increases with the level of water turbidity. For example, at $N = 10$ and assuming DF relaying, we have $d_{\text{multi-hop}}/d_{\max} = 7.12$, 7.62, 7.82, and 8.43 for pure sea, clear ocean, coastal water and harbor water, respectively.

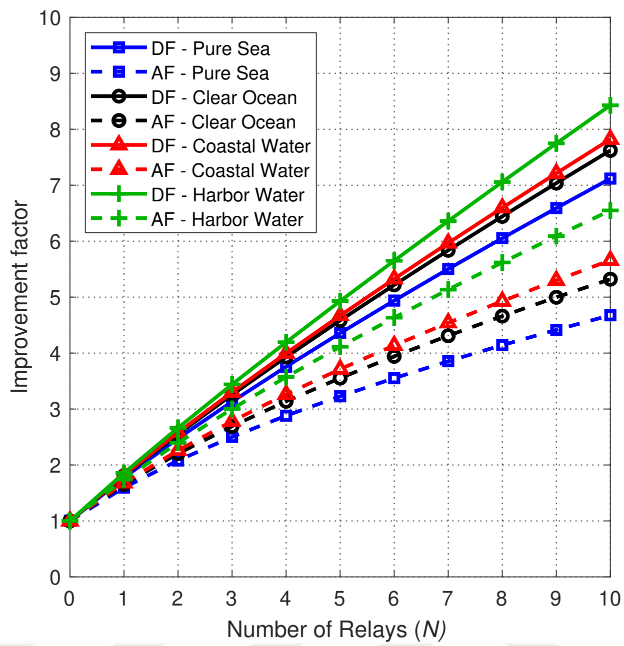

Figure 5: Improvement factor for maximum achievable distance in different water types.

2.4 *Adaptive DC-biased OFDM*

In Sections 2.2 and 2.3, frequency-flat channel has been considered. This is since underwater optical channels exhibit frequency selectivity only for data rates higher than hundreds of Mb/s. Underwater VLC can achieve much higher data rates sufficiently high for real-time image and video transmission. Such high data rates over underwater channels with frequency-selectivity necessitate the use of efficient multi-carrier techniques such as OFDM. In this section, we consider an adaptive DCO-OFDM underwater VLC system. The design of the adaptive algorithm is formulated to maximize the throughput under error rate performance constraints. The receiver first calculates the SNR per each subcarrier. Then, based on SNR information, it determines which subcarrier should be loaded first and selects the maximum constellation size for each subcarrier while satisfying a predefined targeted BER. Our simulation results demonstrated that significant improvements in throughput can be obtained through link adaptation.

2.4.1 System Model

We consider an underwater VLC system with a link distance of d at a depth of z from the sea surface. The block diagram of adaptive-DCO-OFDM system under consideration is provided in Figure 6. The source node first maps bit streams into complex symbols chosen from one of two available modulation techniques, i.e., Phase Shift Keying (PSK) or Quadrature Amplitude Modulation (QAM). The selection of subcarriers to be loaded and modulation size for each subcarrier are made by the adaptive algorithm (see Section 2.4.2).

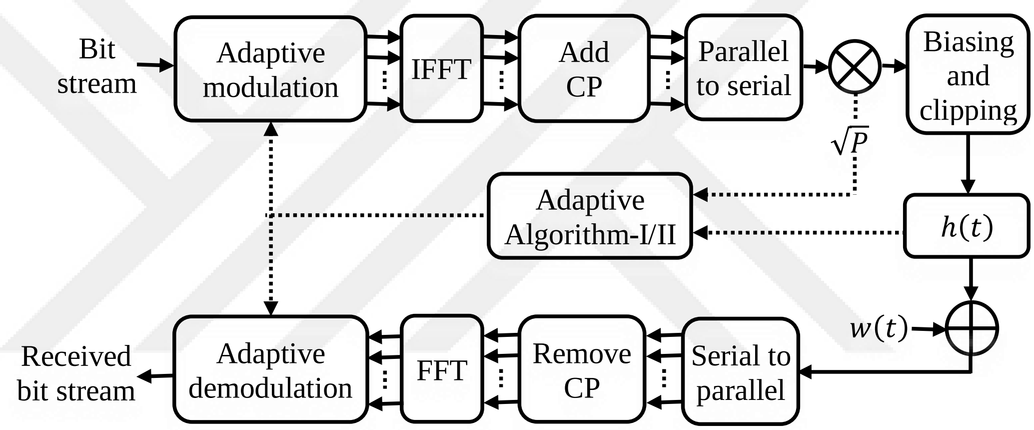

Figure 6: Block diagram of adaptive DCO-OFDM.

Let S_i, $i = 1, \cdots, N/2-1$ denote PSK/QAM modulated symbols where N is the number of subcarriers. To ensure that the output of Inverse Discrete Fourier Transform (IDFT) is real-valued, Hermitian symmetry is applied. Therefore, the resulting OFDM symbol is expressed in the form of $\mathbf{X} = \begin{bmatrix} 0 & S_1 & \cdots & S_{N/2-1} & 0 & S^*_{N/2-1} & \cdots & S^*_1 \end{bmatrix}^T$ where only $N/2-1$ subcarriers are assigned to data. The output of IDFT block can be written as $x[n] = \frac{1}{\sqrt{N}} \sum_{k=0}^{N-1} X[k] \exp\left(j2\pi nk/N\right)$, $n = 0, 1, \cdots, N-1$. The resulting time-domain real-valued signal is given by $\mathbf{x} = \begin{bmatrix} x[0] & x[1] & \cdots & x[N-1] \end{bmatrix}^T$. A Cyclic Prefix (CP) with a length of N_{CP} is appended. This results in $\tilde{\mathbf{x}} = \begin{bmatrix} x[N-N_{cp}] & \cdots & x[N-1] & x[0] & \cdots & x[N-1] \end{bmatrix}^T$. After the addition of DC bias (denoted by V_{DC}) to ensure that the resulting signal lies within the dynamic range of LED, the continuous waveform can be expressed as

$$x_s(t) = \sqrt{P} \sum_{k=0}^{(N-1)+N_{cp}} \tilde{x}[k]\,\delta(t-kT_s) + V_{DC}, \tag{2.29}$$

where $\tilde{x}[k]$ is the k^{th} element of $\tilde{\mathbf{x}}$, P is average electrical transmit power, T_s is pulse duration and $\delta(\cdot)$ is the Dirac delta function. The received electrical signal at the destination can be written as

$$\tilde{y}(t) = Rx_s(t) \otimes h(t) + w(t), \tag{2.30}$$

where $\otimes$ is the convolution sign, R is the photodetector responsivity, $h(t)$ is the underwater Channel Impulse Response (CIR) and $w(t) \sim \mathcal{N}\left(0, \sigma_n^2\right)$ denoting that $w(t)$ follows Gaussian distribution with zero mean and variance of σ_n^2. Replacing Eq. (2.29) in Eq. (2.30), we have Eq. (2.31)

$$\tilde{y}(t) = R\left[\sqrt{P} \sum_{k=0}^{(N-1)+N_{cp}} \tilde{x}[k]\,\delta(t-kT_s)\right] \otimes h(t) + V_{R_{DC}}(t) + w(t)\cdot \tag{2.31}$$

In (3), we define $V_{R_{DC}}(t) = RV_{DC} \otimes h(t)$. Let $w(n)$, $\tilde{y}(n)$, $h(n)$ and $V_{R_{DC}}(n)$ denote, respectively, the sampled versions of $w(t)$, $\tilde{y}(t)$, $h(t)$ and $V_{R_{DC}}(t)$. Noting that $V_{R_{DC}}(n)$ has the same value for all samples, we drop index n and write it as $V_{R_{DC}}$. After removing CP from $\tilde{y}(n)$, the resulting signal $y(n)$ can be written as

$$y(n) = \sqrt{P}Rx(n) \otimes h(n) + V_{R_{DC}} + w(n), \quad n = 0,\cdots,N-1 \;\cdot \tag{2.32}$$

Taking the Fourier transform and let $x(n) \xleftrightarrow{\text{DFT}} X(k)$ denotes N-point Discrete Fourier Transform (DFT) (N-DFT), the corresponding frequency domain signal for the k^{th} carrier can be written as

$$Y(k) = \sqrt{P}RX(k)H(k) + W(k), \quad k = 1,\cdots,N/2-1 \;, \tag{2.33}$$

where $h(n) \xleftrightarrow{\text{DFT}} H(k)$ and $w(n) \xleftrightarrow{\text{DFT}} W(k)$. Note that since $V_{R_{DC}}$ is a DC signal, its Fourier transform is zero everywhere, except at subcarrier $k=0$. Therefore, it does not appear in Eq. (2.33).

2.4.2 Adaptive Algorithms

In this section, we consider two adaptive algorithms [77–79] from the literature which were originally proposed in the context of RF communication and apply to UVLC systems under consideration. These adaptive algorithms were designed to maximize the throughput by selecting proper subcarrier and deciding on modulation size for each subcarrier.

Let n_k denote the number of bits for loading the k^{th} subcarrier. The throughput (i.e., average number of bits per subcarrier) for DCO-OFDM is then given by

$$\bar{n} = \frac{1}{N/2-1} \sum_{k=1}^{N/2-1} n_k \ . \tag{2.34}$$

In Algorithm 1 on the next page, the throughput is maximized by choosing the highest modulation size on each subcarrier under the constraint that BER per subcarrier does not exceed a specific BER. Mathematically speaking, we can write [79]

$$\begin{aligned} &\max \bar{n} \\ &\text{s.t.: } BER[k] \leq BER_{\max}, \end{aligned} \tag{2.35}$$

where $BER\,[k]$ denotes the BER for the k^{th} subcarrier and $BER_{\max}$ denotes the maximum acceptable BER. For 2-PSK and M-QAM (assuming $M = U \times J$ with M denoting the modulation size), $BER\,[k]$ can be computed as [80]

$$BER[k] = A\,Q\left(\sqrt{C\,SNR[k]}\right), \tag{2.36}$$

In Eq. (2.36), $A = (2M-U-J)/\left(M\log_2\sqrt{M}\right)$, $C = 6/\left(U^2+J^2-2\right)$, and $SNR[k] = PR^2H^2\,(k)/\sigma_n^2$.

The throughput maximization in Eq. (2.35) can be further improved by considering a constraint on the overall BER. In Algorithm 2 on page 31, the optimization problem is formulated as [81]

$$\begin{aligned} &\max \bar{n} \\ &\text{s.t.: } BER \leq BER_{\max}, \end{aligned} \tag{2.37}$$

where BER denotes the average BER and is given by

$$BER = \frac{1}{N/2-1} \sum_{k=1}^{N/2-1} BER[k] \cdot \tag{2.38}$$

The flowcharts of Algorithms under consideration are provided, respectively, in Algorithms 1 and 2 on the current page and on the following page. In these algorithms, $M_{\max}$ denotes the maximum modulation size. Therefore, $n_{\max} = \log_2(M_{\max})$ denotes the maximum number of bits that can be loaded to a subcarrier. Let $\mathbf{n}$ denote the vector that contains bit loading information of all subcarriers in the first half of OFDM symbols (i.e., data-carrying part). This is given by Eq. (2.39)

$$\mathbf{n} = \begin{bmatrix} n_1 & n_2 & \cdots & n_k & \cdots & n_{N/2-1} \end{bmatrix}, \quad n_k \leq n_{\max} \ \forall k, \quad k = 1, \cdots, N/2-1 \tag{2.39}$$

Algorithm 1 is executed simply by computing the BER per subcarrier for different modulation sizes and then the modulation with the highest size that satisfies $BER[k] \leq BER_{\max}$ is selected. In Algorithm 2 on the next page, bit loading is initiated by assigning the first bit to the subcarrier that imposes the least BER to accept one bit. Then, the k^{th} subcarrier is selected, for which the transmission of an additional bit can be done with the smallest increase in average BER. The algorithm stops when subcarriers cannot be loaded with an extra bit subject to maximum acceptable average BER.

Algorithm 1 OFDM-Bit Loading Adaptive Algorithm-I

for $k = 1$ to $N/2-1$ **do**
    for $n_k = 1$ to $n_{\max}$ **do**
        if $BER[k]_{+1} \leq BER_{\max}$ **then**
            load k^{th} subcarrier by n_k bits.
        else
            k^{th} subcarrier cannot be loaded with extra bit.
        end if
    end for
end for

Algorithm 2 OFDM-Bit Loading Adaptive Algorithm-II

1: **Initialize:**
   $n_k = 0\,\forall k,\ k = 1,2,\ldots,N/2-1$ $BER = 0$
   Define: $\mathbf{BER_{+1}} = [\,]$
2: **while** $BER \leq BER_{\max}$ **do**
   Step 1: Search for all subcarriers that can be loaded with extra bit.
3: **for** $k = 1$ to $N/2-1$ **do**
4: **if** $n_k = n_{\max}$ **then**
5: This subcarrier cannot be loaded with extra bit.
6: **else**
7: Compute $BER_{k_{+1}}$ and add it to $\mathbf{BER_{+1}}$.
8: **end if**
9: **end for**
   Step 2: Select the subcarrier to be loaded with extra one bit.
10: **if** $\min\left(\mathbf{BER_{+1}}\right) \leq BER_{\max}$ **then**
   1. k^{th} subcarrier that satisfies $BER_{k_{+1}} = \min\left(\mathbf{BER_{+1}}\right)$ will be loaded by extra bit.
   2. Update the new average BER, i.e., $BER = \min\left(\mathbf{BER_{+1}}\right)$
   3. Update the vector $\mathbf{n}$, i.e., $\mathbf{n} = \begin{bmatrix} \mathbf{n_1} & \mathbf{n_2} & \cdots & \mathbf{n_k}+\mathbf{1} & \cdots & \mathbf{n_{N/2-1}} \end{bmatrix}$
   4. Re-initialize the vector $\mathbf{BER_{+1}}$, i.e., $\mathbf{BER_{+1}} = [\,]$.
11: **else**
12: Stop iterations.
13: **end if**
14: **end while**

In Algorithms, if the k^{th} subcarrier is likely to be loaded with an extra bit, i.e., the new possible number of bits for the k^{th} subcarrier is n_k+1, the average BER is then defined as

$$BER_{k_{+1}} = \frac{1}{N/2-1}\left[BER[k]_{+1} + \sum_{\substack{i=1\\ i\neq k}}^{N/2-1} BER\,[i]\right], \tag{2.40}$$

where $BER[k]_{+1}$ denotes the BER of the k^{th} subcarrier if it is loaded by extra bit.

2.4.3 Results and Discussions

In this section, we present simulation results for adaptive DCO-OFDM UVLC systems under consideration. We consider a scenario where the link is placed horizontally at a depth of $z = 5$ m with a link distance of $d = 20$ m in coastal water. CIR for the link under consideration is obtained by the using of ray tracing simulation similar to [37] with channel parameters listed in Table 3.

Table 3: Channel Parameters.

Transmitter specifications	Power: 1 Watt Brand: Cree® XR-E LED Viewing angle: 60°
Receiver specifications	Aperture size: 50 cm Field of view: 180°
Absorption, scattering and extinction coefficients $\left(\mathrm{m}^{-1}\right)$	0.2347, 0.3375, 0.5722
Scattering phase function	One-term Henyey-Greenstein (OTHG)
Mean cosine of scattering angles	0.9470

In Figure 7, we present CIR, sampled CIR as well as the channel transfer function obtained through Fourier transform. The sampled version of the channel is obtained based on pulse duration of $T_s = 10$ ns. It is observed from Figure 7 that the delay spread exceeds 20 ns and such a channel will exhibit frequency-selectivity if the symbol rate exceeds 50 Mega-Symbols Per Second (MS/s). As system parameters, we assume a responsivity of $R = 0.28$ A/W, average electrical transmit power of $P = 15$ dBm, noise variance of $\sigma_n^2 = -120$ dBm and number of subcarriers of $N = 64$. We assume the deployment of 2-PSK, 4-QAM and 8-QAM.

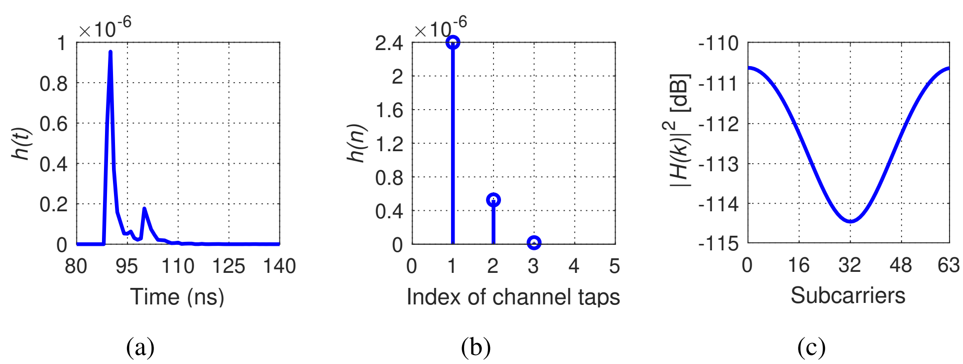

Figure 7: (a) CIR, (b) sampled CIR and (c) channel transfer function.

In Fig. 8, we consider Algorithm 1 on page 30 and present the achieved BER of each subcarrier for the modulation types under consideration. The selected modulation is shown by circles. We consider $BER_{\max} = 1 \times 10^{-3}$ and 1×10^{-5} as the maximum acceptable BER values in Figs. 8(a) and 8(b), respectively. It is observed from Fig. 8(a) that $BER_{\max} = 1 \times 10^{-3}$ can be satisfied with Algorithm 2 on page 31 by selecting the modulation order of 4-QAM for most subcarriers and 2-PSK for the other subcarriers that experience weak channel gains. The average loading is therefore achieved as $\bar{n} = 1.839$ Bits Per Subcarrier (b/s). In non-adaptive transmission, $BER_{\max} = 1 \times 10^{-3}$ can be satisfied by loading all subcarriers with 2-PSK. Therefore, the average loading for the non-adaptive system is $\bar{n} = 1.0$ b/s. This indicates that adaptive transmission brings an improvement percentage of 83.9%. In Fig. 8(b), the maximum acceptable BER is set as $BER_{\max} = 1 \times 10^{-5}$. It can be satisfied by selecting either 4-QAM or 2-PSK for some subcarriers while some subcarriers have $BER[k] > BER_{\max}$ even for 2-PSK. Therefore, these subcarriers will not be loaded. An average loading of $\bar{n} = 1.258$ b/s is obtained. On the other hand, in non-adaptive transmission, even if all subcarriers are loaded with 2-PSK, the condition of $BER[k] \leq 1 \times 10^{-5}$ cannot be satisfied and hence $\bar{n} = 0$ b/s is obtained.

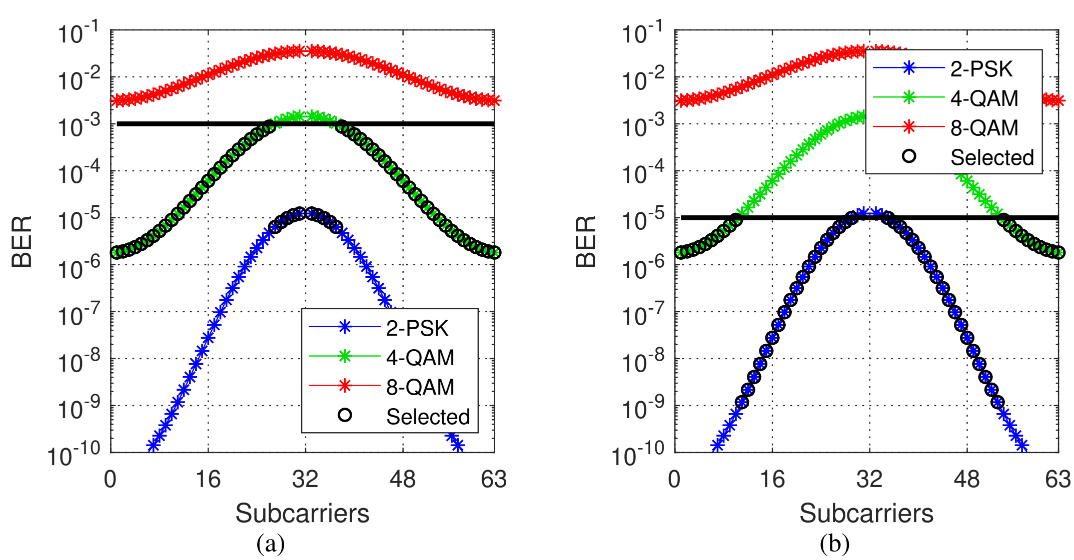

Figure 8: Bit loading for Algorithm-I: (a) $BER_{\max}$=1×10^{-3} and (b) $BER_{\max}$=1×10^{-5}.

In Fig. 9, we consider Algorithm 2 on page 31 with overall BER constraint. The selected modulation is shown by circles. Unlike Fig. 8 on the previous page where 8-QAM is never selected, there are some instances where this modulation type is further selected. Furthermore, it can be observed that some subcarriers have BER more than targeted BER. However, over the average, the BER constraint is satisfied. Average bit loading of $\bar{n} = 2.097$ b/s and $\bar{n} = 1.484$ b/s are obtained for $BER_{\max} = 1 \times 10^{-3}$ and 1×10^{-5}, respectively. These are higher than those in Algorithm 1 on page 30. It is expected since individual subcarrier in Algorithm 2 on page 31 can be loaded with additional bit and the BER in that subcarrier may exceed the maximum acceptable BER while in Algorithm-I each subcarrier must satisfy the maximum acceptable BER.

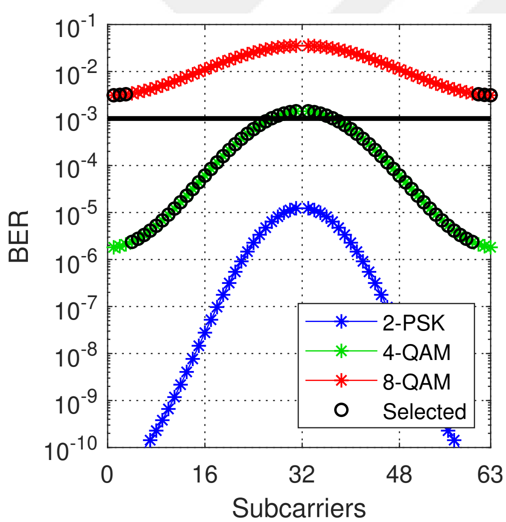

(a)

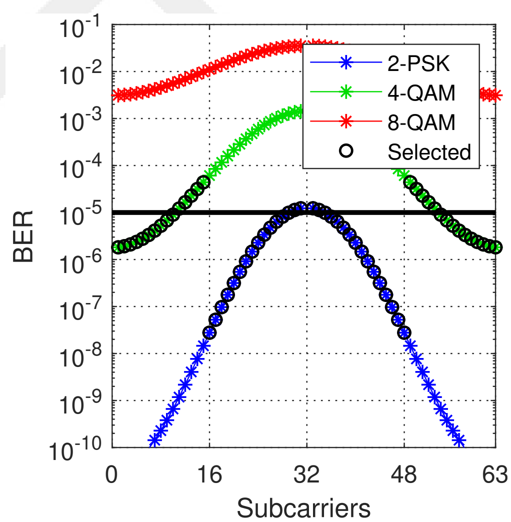

(b)

Figure 9: Bit loading for Algorithm-II: (a) $BER_{\max}$=1 × 10^{-3} and (b) $BER_{\max}$=1 × 10^{-5}.

CHAPTER III

UNDERWATER TURBULENCE CHANNEL MODELING

3.1 Introduction

In addition to the path loss that we discussed in Section 1.3.1, UOT introduces instantaneous fluctuations over the average received power [15]. This is as a result of the fluctuation in the refractive index of seawater which is mainly caused by temperature and salinity fluctuations. Therefore, there is a need for accurate spatial power spectrum model of turbulent fluctuations of the sea-water refraction index that accurately describe how the fluctuation in both temperature and salinity contribute to the fluctuation in the refractive index. Furthermore, the temperature of the seawater, as well as its salinity, are not constant, but change with depth. Therefore, the vertical link may experience variation in turbulence strength through the transmission range, which must be considered.

The rest of this chapter is organized as follow. In Section 3.2, we discuss the spatial power spectrum model of turbulent fluctuations of the sea-water refraction index. In Section 3.3, we discuss the horizontal and vertical UVLC turbulence channels.

3.2 Power Spectrum Model

Most of the previous studies [82–89] assume a simplifying, yet inaccurate, assumption in turbulence spectrum model that eddy diffusivity ratio is equal to unity. It is however well known that eddy diffusivity of temperature and salt are different from each other in most underwater environments. Therefore, we first present the spatial power spectrum model of turbulent fluctuations of the sea-water refraction index in Section 3.2.1 and revise the spectrum model and express it as an explicit function of eddy diffusivity ratio in Section 3.2.2. Using the derived spectrum model, we obtain the scintillation index of optical plane and spherical waves and investigate the effect of eddy diffusivity ratio in Section 3.2.3. In Section 3.2.4, we present numerical results and discussions

3.2.1 Spectrum Model of UOT

The spatial power spectrum of turbulent fluctuations of the sea-water refraction index is given by [62]

$$\Phi_n(\kappa) = \left(4\pi\kappa^2\right)^{-1} C_0 \chi_n \varepsilon^{-\frac{1}{3}} \kappa^{-\frac{5}{3}} \left[1 + C_1 (\kappa\mathfrak{Y})^{\frac{2}{3}}\right] \phi(\kappa,\omega) , \tag{3.1}$$

where κ is the magnitude of the spatial frequency, ε is the dissipation rate of turbulent kinetic energy per unit mass of fluid and the constants C_0 and C_1 are respectively equal to 0.72 and 2.35. In Eq. (3.1), $\mathfrak{Y}$ is Kolmogorov microscale length and given by $\mathfrak{Y} = \left(\upsilon^3/\varepsilon\right)^{1/4}$ with υ denoting the kinematic viscosity. χ_n is the dissipation rate of mean-squared refractive index and given by

$$\chi_n = \alpha^2 \chi_T + \beta^2 \chi_S - 2\alpha\beta\chi_{TS}, \tag{3.2}$$

where α is thermal expansion coefficient and β is saline (i.e., Haline) contraction coefficient. χ_T, χ_S and χ_{TS} are respectively the dissipation rate of mean-squared temperature, the dissipation rate of mean-squared salinity and the correlation of χ_T and χ_S. They are given as

$$\chi_T = K_T \left(\frac{dT_0}{dz}\right)^2 , \tag{3.3}$$

$$\chi_S = K_S \left(\frac{dS_0}{dz}\right)^2 , \tag{3.4}$$

$$\chi_{TS} = \frac{K_T + K_S}{2} \left(\frac{dT_0}{dz}\right)\left(\frac{dS_0}{dz}\right) , \tag{3.5}$$

where K_S and K_T denote eddy diffusivity of salinity and temperature, respectively. In Eq. (3.1), $\phi(\kappa,\omega)$ is given by

$$\phi(\kappa,\omega) = \frac{1}{\omega^2 - (1+d_r)\,\omega + d_r} \begin{pmatrix} \omega^2 \exp\left(-C_0 C_1^{-2} P_T^{-1} \delta\right) \\ +d_r \exp\left(-C_0 C_1^{-2} P_S^{-1} \delta\right) \\ -\omega\,(d_r+1) \exp\left(-C_0 C_1^{-2} (2P_{TS})^{-1} \delta\right) \end{pmatrix} , \tag{3.6}$$

where $\delta = 1.5C_1^2(\kappa\mathfrak{Y})^{\frac{4}{3}} + C_1^3(\kappa\mathfrak{Y})^2$ and ω is the relative strength of temperature and salinity fluctuations. Let dT_0/dz and dS_0/dz respectively denote the temperature and salinity difference between top and bottom boundaries, respectively. The term ω is then defined as

$$\omega = \frac{\alpha\left(dT_0/dz\right)}{\beta\left(dS_0/dz\right)}. \tag{3.7}$$

In Eq. (3.6) on the preceding page, $P_T = \upsilon D_T^{-1}$ is the Prandtl number for temperature, $P_S = \upsilon D_S^{-1}$ is the Prandtl number for salinity, and P_{TS} is the one-half of the harmonic mean of P_T and P_S. Here, D_T and D_S denote molecular diffusivity of temperature and salinity, respectively. The eddy diffusivity ratio is defined as

$$d_r = \frac{K_S}{K_T}. \tag{3.8}$$

Due to the difficulties of computing either K_T or K_S in most practical cases, this ratio is typically obtained through [90, 91]

$$d_r = \frac{|\omega|}{R_F}, \tag{3.9}$$

where $R_F = \alpha F_T/\beta F_S$ is the eddy flux ratio with F_T and F_S respectively denoting eddy flux of temperature and salinity. It can be calculated as [90, 92, 93]

$$R_F \approx \begin{cases} |\omega| - \sqrt{|\omega|\left(|\omega|-1\right)}, & |\omega| \geq 1 \\ \dfrac{1}{1.85 - 0.85|\omega|^{-1}}, & 0.5 \leq |\omega| \leq 1 \\ \dfrac{1}{0.15}. & |\omega| < 0.5 \end{cases} \tag{3.10}$$

From the above explanations, it is clear that d_r is a function of ω. In previous works [82–89], this is simply ignored and d_r is set to 1 whatever the value of ω is. In the Section 3.2.2, paying particular attention on their dependent characteristics, we aim to obtain a simplified spatial power spectrum model as an explicit function of d_r and ω.

3.2.2 Revised UOT Spectrum Model

Dividing Eq. (3.4) on the preceding page by Eq. (3.3) on the previous page and replacing Eq. (3.8) within the resulting expression, we express the dissipation rate of mean-squared salinity as

$$\chi_S = d_r \frac{\left(dS_0/dz\right)^2}{\left(dT_0/dz\right)^2}\chi_T\cdot \tag{3.11}$$

Utilizing Eq. (3.7) on the previous page, we can rewrite Eq. (3.11) as a function of relative strength of temperature and salinity fluctuations (ω), thermal expansion coefficient (α) and saline contraction coefficient (β) in the form of

$$\chi_S = d_r \left(\frac{\alpha}{\beta\omega}\right)^2 \chi_T\cdot \tag{3.12}$$

Replacing K_T from Eq. (3.3) on page 36 and K_S from Eq. (3.4) on page 36 into Eq. (3.5) on page 36 and using Eq. (3.7) on the preceding page within the resulting expression, we rewrit χ_{TS} as

$$\chi_{TS} = \frac{\alpha}{2\beta\omega}\chi_T + \frac{\beta\omega}{2\alpha}\chi_S\cdot \tag{3.13}$$

Utilizing Eq. (3.12), we can rewrite Eq. (3.13) in the form of

$$\chi_{TS} = \frac{\alpha}{2\beta\omega}\chi_T\left(1+d_r\right)\cdot \tag{3.14}$$

Replacing χ_S from Eq. (3.12) and χ_{TS} from Eq. (3.14) into Eq. (3.2) on page 36, we rewrite χ_n as

$$\chi_n = \frac{\alpha^2\chi_T}{\omega^2}\left[\omega^2 - \left(1+d_r\right)\omega + d_r\right]\cdot \tag{3.15}$$

By inserting Eq. (3.6) on page 36 and Eq. (3.15) into Eq. (3.1) on page 36, we obtain the spectrum model as

$$\begin{aligned}\Phi_n(\kappa) = &\left(4\pi\kappa^2\right)^{-1} C_0 \left(\frac{\alpha^2\chi_T}{\omega^2}\right)\varepsilon^{-\frac{1}{3}}\kappa^{-\frac{5}{3}}\left[1+C_1\left(\kappa\mathfrak{Y}\right)^{\frac{2}{3}}\right] \\ &\times \begin{pmatrix} \omega^2 \exp\left(-C_0C_1^{-2}P_T^{-1}\delta\right) \\ +d_r \exp\left(-C_0C_1^{-2}P_S^{-1}\delta\right) \\ -\omega\left(d_r+1\right)\exp\left(-0.5C_0C_1^{-2}P_{TS}^{-1}\delta\right)\end{pmatrix}.\end{aligned} \tag{3.16}$$

As a sanity check, we also consider two special cases of eddy diffusiviy ratio. Under the assumption that the contribution of salinity to density variation $\beta\left(dS_0/dz\right)$ cancels the contribution of temperature to density variation $\alpha\left(dT_0/dz\right)$ (i.e., d_r = 1 and ω=1), χ_n in

Eq. (3.15) on the previous page becomes zero (i.e., there is no turbulence). Under the assumption that the contribution of salinity to density variation is equal to the contribution of temperature to density variation (i.e., d_r = 1 and ω = -1), $\Phi_n(\kappa)$ in Eq. (3.16) on the preceding page reduces to

$$\begin{aligned}\Phi_n(\kappa) = &\left(4\pi\kappa^2\right)^{-1} C_0\alpha^2\chi_T\varepsilon^{-\frac{1}{3}}\kappa^{-\frac{5}{3}}\left[1+C_1(\kappa\mathfrak{Y})^{\frac{2}{3}}\right] \\ &\times\left[\exp\left(-A_T\delta\right)+\exp\left(-A_S\delta\right)+2\exp\left(-A_{TS}\delta\right)\right],\end{aligned} \tag{3.17}$$

where $A_T = C_0C_1^{-2}P_T^{-1}$, $A_S = C_0C_1^{-2}P_S^{-1}$, and $A_{TS} = 0.5C_0C_1^{-2}P_{TS}^{-1}$. This special case has been also reported in [82, Eq. (8)].

3.2.3 Scintillation Index for Optical Plane and Spherical Waves

The strength of optical intensity fluctuation is typically quantified by scintillation index defined by [94]

$$\sigma^2 = \frac{\left\langle I^2(r,d_0,\lambda)\right\rangle - \langle I(r,d_0,\lambda)\rangle^2}{\langle I(r,d_0,\lambda)\rangle^2}, \tag{3.18}$$

where $\langle I(r,d_0,\lambda)\rangle$ and $\left\langle I^2(r,d_0,\lambda)\right\rangle$ are the average of received intensity and the average of the square of the received intensity at a point detector with position $(r,d_0) = (x,y,d_0)$, respectively. d_0 is the link length and λ is the wavelength.

For plane waves under the assumption of weak turbulence, the scintillation index can be calculated by [94]

$$\sigma^2 = 8\pi^2k_0^2d_0\int_0^1\int_0^\infty \kappa\Phi_n(\kappa)\left\{1-\cos\left[\frac{d_0\kappa^2}{k_0}\zeta\right]\right\}d\kappa d\zeta, \tag{3.19}$$

where $k_0 = 2\pi/\lambda$ is the wavenumber. By replacing Eq. (3.16) on the previous page in Eq. (3.19), we obtain

$$\begin{aligned}\sigma^2 =&2\pi k_0^2 d_0 C_0 \alpha^2 \frac{\chi_T}{\omega^2}\varepsilon^{-\frac{1}{3}} \int_0^1 \int_0^\infty \kappa^{-\frac{8}{3}} \left\{1-\cos\left[\frac{d_0\kappa^2}{k_0}\zeta\right]\right\} \\ &\times \left[1+C_1(\kappa\mathfrak{Y})^{\frac{2}{3}}\right] \begin{pmatrix} \omega^2 \exp(-A_T\delta) \\ +d_x \exp(-A_S\delta) \\ -\omega(d_x+1)\exp(-A_{TS}\delta) \end{pmatrix} d\kappa d\zeta, \end{aligned} \tag{3.20}$$

For spherical waves under the assumption of weak turbulence, the scintillation index can be calculated by [94]

$$\sigma^2 = 8\pi^2 k_0^2 d_0 \int_0^1 \int_0^\infty \kappa\Phi_n(\kappa) \left\{1-\cos\left[\frac{d_0\kappa^2}{k_0}(\zeta-\zeta^2)\right]\right\} d\kappa d\zeta. \tag{3.21}$$

Replacing Eq. (3.16) on page 38 in Eq. (3.21), we have

$$\begin{aligned}\sigma^2 =& 2\pi k_0^2 d_0 C_0 \alpha^2 \frac{\chi_T}{\omega^2}\varepsilon^{-\frac{1}{3}} \int_0^1 \int_0^\infty \kappa^{-\frac{8}{3}} \left\{1-\cos\left[\frac{d_0\kappa^2}{k_0}(\zeta-\zeta^2)\right]\right\} \\ &\times \left[1+C_1(\kappa\mathfrak{Y})^{\frac{2}{3}}\right] \begin{pmatrix} \omega^2 \exp(-A_T\delta) \\ +d_x \exp(-A_S\delta) \\ -\omega(d_x+1)\exp(-A_{TS}\delta) \end{pmatrix} d\kappa d\zeta, \end{aligned} \tag{3.22}$$

While there are no closed-form expressions for Eq. (3.20) and Eq. (3.16) on page 38, these can be efficiently evaluated by numerical means.

3.2.4 Results and Discussions

In this section, we present numerical results for the scintillation index of plane and spherical waves for different eddy diffusivity ratios. We limited the scintillation index value smaller than one; therefore, our results are for weak turbulence. We assume $\alpha = 2.56\times10^{-4}\,1/\deg$, $\beta = 7.44X10^{-4}\,1/\mathrm{g}$, $P_T \approx 7$, $P_S \approx 700$, $\upsilon = 1.0576\times10^{-6}\,\mathrm{m^2s^{-1}}$ when the salinity is 35 Part Per Thousand (PPT) and the temperature is 20°C [95, 96] (i.e. $A_T = 1.863\times10^{-2}$, $A_S = 1.9\times10^{-4}$ and $A_{TS} = 9.41\times10^{-3}$). The other parameters are $\chi_T = 1\times10^{-5}\,\mathrm{K^2s^{-3}}$, $\varepsilon = 1\times10^{-2}\,\mathrm{m^2s^{-3}}$ and $\lambda = 0.530\,\mu\mathrm{m}$.

In Figure 10(a), we present the scintillation index with respect to link length for plane waves using Eq. (3.20) on the preceding page. We assume ω = - 0.25, - 0.75, -1, -3 and -5. The corresponding values of eddy diffusivity ratios are then calculated as d_r = 0.037, 0.54, 1.0, 5.4 and 9.5 based on Eq. (3.9) on page 37 and Eq. (3.10) on page 37. In previous works [82–89], it is simply assumed that d_r and ω are independent of each other and d_r is set to 1. To demonstrate the difference between our results and the previous results, Figure 10(b) presents the scintillation index based on this erroneous assumption of d_r = 1.

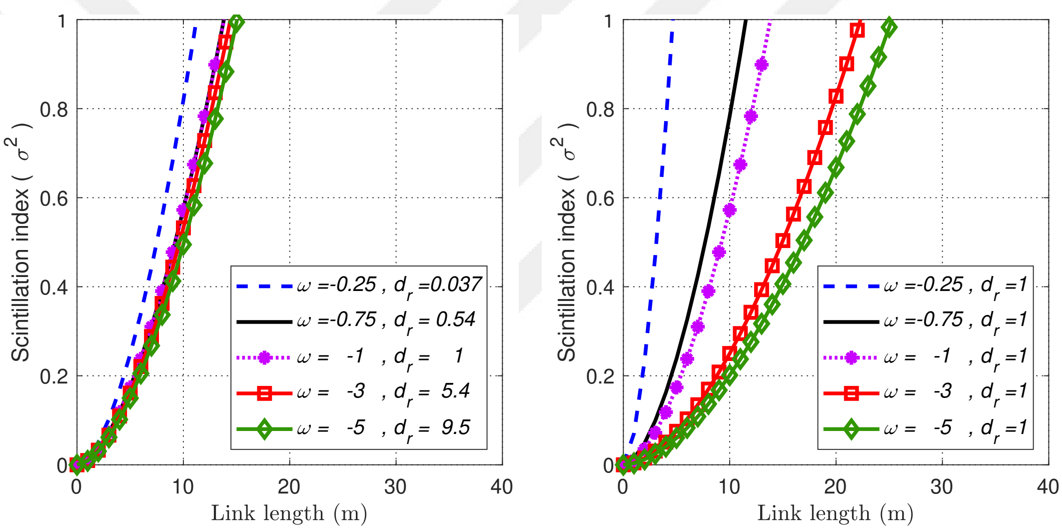

(a) Diffusivity ratios are calculated based on the assumed ω values.

(b) Unity eddy diffusivity ratio is assumed regardless of ω value.

Figure 10: Scintillation index of plane waves.

It is observed from the comparison of Figures 10(a) and 10(b) that the scintillation index is either underestimated or overestimated in previous works that were built on the assumption of unity eddy diffusivity ratio. For $|\omega| > 1$ (i.e., underwater turbulence is dominated by the temperature fluctuations), the scintillation index is underestimated. For example, assume a link distance d_0 = 10 m. Figure 10(b) shows that the scintillation index for $|\omega| = 3$ is 0.25 while the actual value (as seen from Figure 10(a)) should be 0.53. Relative error percentage is 53%. For $|\omega| < 1$ (i.e., underwater turbulence is dominated by the salinity fluctuations), the scintillation index is overestimated. For example, assume a link distance $d_0 = 5$ m, Figure 10(b) on the previous page shows that the scintillation index for $|\omega| = 0.75$ is 0.238 while the actual value (as seen from Figure 10(a) on the preceding page) should be 0.174. Relative error percentage is 36%.

In Figures 11(a) and 11(b), we present the scintillation index with respect to link length for spherical waves using Eq. (3.22) on page 40. We assume the same set of ω and d_r pairs. Similar to plane waves, the comparison reveals that the scintillation index is not accurately calculated and either underestimation or overestimation take place if the dependence of ω and d_r is ignored. Further comparison of Figures 10(a) and 11(a) on the previous page and on this page show that the scintillation index of plane wave is larger than that of the spherical wave. For example, assume a link distance $d_0 = 10$ m and $|\omega| = 1$. Figures 10(a) and 10(b) on the previous page show that the scintillation index is 0.57 and 0.26 for plane waves and spherical waves, respectively. It is also observed that the change in scintillation is more noticeable for $d_r < 1$ (i.e.,$|\omega| < 1$) in both plane and spherical waves.

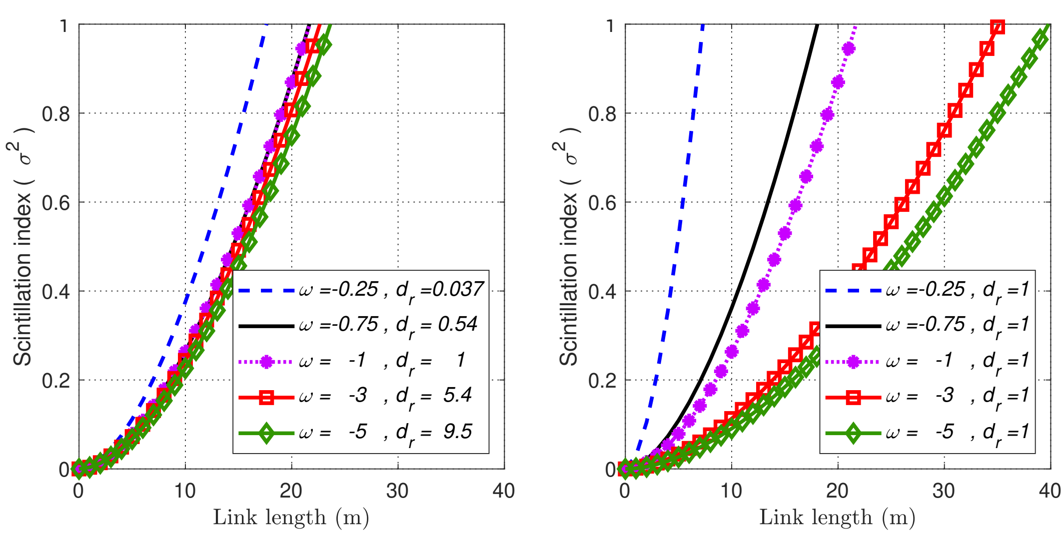

(a) Diffusivity ratios are calculated based on the assumed ω values.

(b) Unity eddy diffusivity ratio is assumed regardless of ω value.

Figure 11: Scintillation index of spherical waves.

3.3 Statistical Modeling of Underwater Links

Most of the initial works in UVLC literature [31, 47] consider only path loss and ignore the effects of turbulence. However, refractive index fluctuates in an underwater environment due to salinity and temperature fluctuations effectively results in underwater turbulence. This turbulence causes the received signal intensity to fluctuate over its average also known as fading. Therefore, full statistical characterization for the distribution of turbulence-induced fading in UVLC systems must be investigated.

3.3.1 Horizontal Links

The statistical distribution of underwater fading was investigated experimentally for horizontal UVLC links in [10, 52–55]. LN and GG PDF were shown to match the measurement results [52, 54, 55] respectively for weak and moderate/strong turbulence.

3.3.1.1 Weak Turbulence

Assuming weak turbulence conditions and let I_h denote the fading coefficient of horizontal link, the PDF of I_h is then given by

$$f_{I_h}(I_h) = \frac{1}{I_h\sqrt{2\pi\left(4\sigma_{x_h}^2\right)}} \exp\left(-\frac{\left(\ln\left(I_h\right) - 2\mu_{x_h}\right)^2}{2\left(4\sigma_{x_h}^2\right)}\right) \cdot \tag{3.23}$$

where $\sigma_{x_h}^2$ and μ_{x_h} denote, respectively, the variance and the mean of log-amplitude coefficient $X_h = 0.5\ln\left(I_h\right)$. In order to make sure that the fading coefficient does not influence the value of average power, the fading amplitude is normalized such that $\mathrm{E}\left[I_h\right] = 1$, which implies $\mu_{x_h} = -\sigma_{x_h}^2$ [19]. Let $\sigma_{I_h}^2$ denote the scintillation index of the horizontal link. Then, the log-amplitude variance $\sigma_{x_h}^2$ can be written in terms of scintillation index as

$$\sigma_{x_h}^2 = 0.25\ln\left(1+\sigma_{I_h}^2\right) \cdot \tag{3.24}$$

3.3.1.2 Moderate/Strong Turbulence

In moderate to strong turbulence conditions, the fading coefficient of horizontal link I_k follows GG distribution [54]. Its PDF is given by

$$f_{I_h}(I_h) = \frac{2(\alpha_h\beta_h)^{(\alpha_h+\beta_h)/2}}{\Gamma(\alpha_h)\Gamma(\beta_h)} I_h^{((\alpha_h+\beta_h)/2)-1} \mathrm{K}_{\alpha_h-\beta_h}\left(2\sqrt{\alpha_h\beta_h I_h}\right), \tag{3.25}$$

where $\Gamma(\cdot)$ and $\mathrm{K}_v(\cdot)$ are Gamma function and modified Bessel function of the second kind with order v. In Eq. (3.25), α_h and β_h are the effective number of large-scale and small-scale cells of the scattering process for the horizontal link, respectively. Under the assumption of plane wave propagation, they are given by [97, Chapter 3]

$$\alpha_h = \left[\exp\left(\frac{0.49\sigma_{I_h}^2}{\left(1+1.11\sigma_{I_h}^{12/5}\right)^{7/6}}\right) - 1\right]^{-1}. \tag{3.26}$$

$$\beta_h = \left[\exp\left(\frac{0.51\sigma_{I_h}^2}{\left(1+0.69\sigma_{I_h}^{12/5}\right)^{5/6}}\right) - 1\right]^{-1}. \tag{3.27}$$

3.3.2 Vertical Links

The performance of UVLC systems over LN and GG turbulence channels was investigated in [5, 6, 16, 56–59]. A common underlying assumption in these works is fixed turbulence strength through the transmission range which can be justified only for horizontal links. In vertical links, the gradient of temperature and salinity changes with depth [60]. This effectively results in ocean stratification, i.e., water with different values of salinity and temperature form non-mixing layers [61]. Extensive measurements performed in the Pacific Ocean showed that strong stratification prevailed in 35% of the cases [62]. Similarly, measurements in the Weddell Sea reveal that the surface layer is separated from the deep ocean by numerous layers [63]. Each of these layers has a thickness which typically varies between few meters to tens of meters [64, 65]. As an example, Figure 12 on the next page illustrates vertical temperature and salinity profiles as a function of depth [60, Fig. 7.1] for different seasons, oceans and latitudes. It is obvious that both temperature and salinity profiles show depth-dependency and this dependency is particularly significant in the top 500 m. This requires the development of cascaded fading channel models for vertical underwater links taking into account the depth-dependency of refractive index.

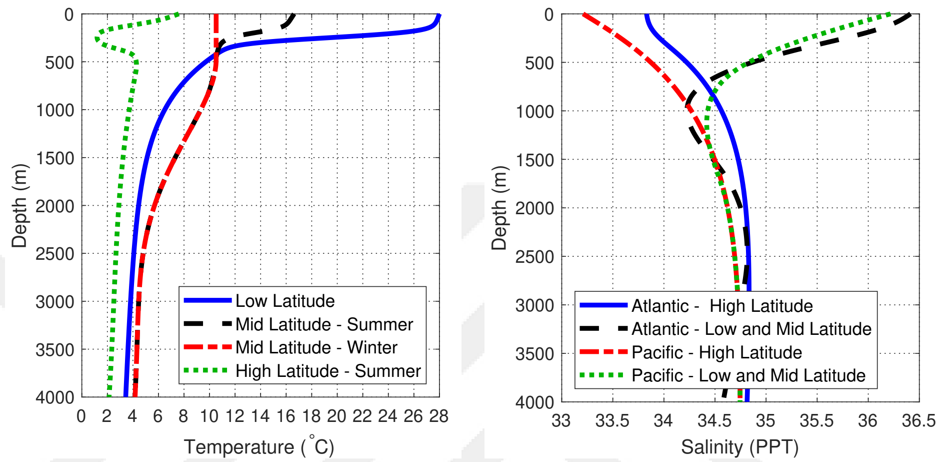

(a) (b)

Figure 12: Oceanic profiles: (a) temperature (b) salinity.

As illustrated in Figure 13 on the following page, we consider an underwater vertical link with a transmission range of d_T. The source is assumed to be placed at a depth of d_0 from the sea surface. Underwater vertical link is modeled as successive non-mixing layers. Let d_k denote the thickness of the k^{th} layer, $k = 1, 2, \cdots, K$. The total transmission range becomes $d_T = \sum_{k=1}^{K} d_k$. Furthermore, let I_k, $k = 1, 2, \cdots, K$, denote the multiplicative fading coefficient of the k^{th} layer[1]. Under the assumption that the coefficients associated with different layers are independent (which can be justified due to ocean stratification), the overall fading coefficient spanning K layers can be expressed as

$$I_T = \prod_{k=1}^{K} I_k. \tag{3.28}$$

[1] Since the underwater delay spread is typically much less than 5 ns [17, 18, 98], underwater optical channels exhibit frequency selectivity only for data rates higher than hundreds of Mb/s [11]. In this section, we assume frequency-flat fading which can be justified for most practical purposes.

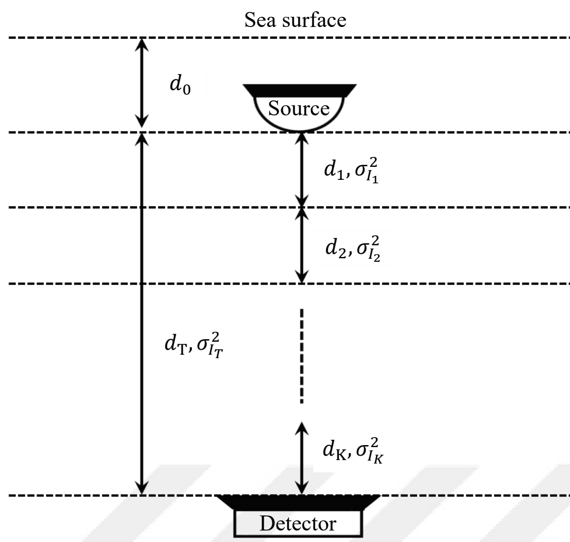

Figure 13: Vertical underwater link under consideration.

3.3.2.1 Weak Turbulence

In weak turbulence conditions, the fading coefficient of each layer I_k follows LN distribution [54]. Let $\sigma^2_{x_k}$ and μ_{x_k} denote, respectively, the variance and the mean of log-amplitude coefficient $X_k = 0.5 \ln(I_k)$ for the k^{th} layer. The PDF of I_k is then given by

$$f_{I_k}(I_k) = \frac{1}{I_k\sqrt{2\pi\left(4\sigma^2_{x_k}\right)}} \exp\left(-\frac{\left(\ln(I_k) - 2\mu_{x_k}\right)^2}{2\left(4\sigma^2_{x_k}\right)}\right). \tag{3.29}$$

Let $\sigma^2_{I_k}$ denote the scintillation index. Then, the variance $\sigma^2_{x_k}$ can be written in terms of scintillation index as

$$\sigma^2_{x_k} = 0.25 \ln\left(1 + \sigma^2_{I_k}\right). \tag{3.30}$$

To ensure that the fading coefficient does not change the value of average power, the fading amplitude is normalized such that $\mathrm{E}[I_k] = 1$, which implies $\mu_{x_k} = -\sigma^2_{x_k}$ [19]. Under the assumption that I_i and I_j are independent, $i, j \in \{1, 2, \cdots, K\}$, but non-identically distributed, it can be shown that the PDF of I_T still follows LN distribution and is given by [99, Chapter 6]

$$f_{I_T}(I_T) = \frac{1}{I_T\sqrt{2\pi\sigma^2_T}} \exp\left(-\frac{\left(\ln(I_T) - \mu_T\right)^2}{2\sigma^2_T}\right), \tag{3.31}$$

where the overall mean and variance are respectively given by $\mu_T = \sum_{k=1}^{K} 2\mu_{x_k}$ and $\sigma_T^2 = \sum_{k=1}^{K} 4\sigma_{x_k}^2$. This indicates that the overall variance is simply found as the summation of the variances of underlying layers' fading coefficients.

3.3.2.2 *Moderate/Strong Turbulence*

In moderate to strong turbulence conditions, the fading coefficient of each layer I_k follows GG distribution [54]. Its PDF is given by

$$f_{I_k}(I_k) = \frac{2(\alpha_k\beta_k)^{(\alpha_k+\beta_k)/2}}{\Gamma(\alpha_k)\Gamma(\beta_k)} I_k^{((\alpha_k+\beta_k)/2)-1} \mathrm{K}_{\alpha_k-\beta_k}\left(2\sqrt{\alpha_k\beta_k I_k}\right), \tag{3.32}$$

α_k and β_k are the effective number of large-scale and small-scale cells of the scattering process for the k^{th} layer, respectively. Under the assumption of plane wave propagation, they are given by [97, Chapter 3]

$$\alpha_k = \left[\exp\left(\frac{0.49\sigma_{I_k}^2}{\left(1+1.11\sigma_{I_k}^{12/5}\right)^{7/6}}\right) - 1\right]^{-1}. \tag{3.33}$$

$$\beta_k = \left[\exp\left(\frac{0.51\sigma_{I_k}^2}{\left(1+0.69\sigma_{I_k}^{12/5}\right)^{5/6}}\right) - 1\right]^{-1}. \tag{3.34}$$

It can be readily verified that the first and second moments of each fading coefficient are respectively given by $E[I_k] = 1$ and $E\left[I_k^2\right] = (1+1/\alpha_k)(1+1/\beta_k)$.

In the following, we derive the PDF for the product of K Independent and Non-Identical Distributed (i.n.i.d) GG random variables. First consider the case of two layers (i.e., $I_T = I_1 I_2$). The PDF of I_T is given as [99, Chapter 6]

$$f_{I_T}(I_T) = \int_{-\infty}^{\infty} f_{I_1}(I_1) f_{I_2}\left(\frac{I_T}{I_1}\right) \frac{1}{|I_1|} \quad dI_1 \ . \tag{3.35}$$

First utilizing [100, Eq. (03.04.26.0009.01)] to express the modified Bessel function of the second kind in Eq. (3.32) in terms of Meijer's G-function, then by using the properties of Meijer's G-function in [101, Eq. (4.256)] within the resulting expression, we can express the PDF in Eq. (3.32) on the preceding page as

$$f_{I_k}\left(I_k\right)=\frac{\alpha_k\beta_k}{\Gamma\left(\alpha_k\right)\Gamma\left(\beta_k\right)}G_{0,2}^{2,0}\left(\alpha_k\beta_kI_k\left|\begin{array}{c}\cdots\\ \alpha_k-1,\beta_k-1\end{array}\right.\right). \tag{3.36}$$

Replacing Eq. (3.36) in Eq. (3.35) on the preceding page, we have

$$\begin{aligned} f_{I_T}\left(I_T\right)=&\frac{\alpha_1\alpha_2\beta_1\beta_2}{\Gamma\left(\alpha_1\right)\Gamma\left(\alpha_2\right)\Gamma\left(\beta_1\right)\Gamma\left(\beta_2\right)}\\ &\times\int_0^\infty I_1^{-1}G_{0,2}^{2,0}\left(\alpha_2\beta_2\frac{I_T}{I_1}\left|\begin{array}{c}\cdots\\ \beta_2-1,\alpha_2-1\end{array}\right.\right)G_{0,2}^{2,0}\left(\alpha_1\beta_1I_1\left|\begin{array}{c}\cdots\\ \beta_1-1,\alpha_1-1\end{array}\right.\right)dI_1. \end{aligned} \tag{3.37}$$

Applying [101, Eq. (4.257)] on the first Meijer's G-function and [101, Eq. (4.256)] on the second Meijer's G-function in Eq. (3.37), we obtain

$$\begin{aligned} f_{I_T}\left(I_T\right)=&\frac{\alpha_1^2\alpha_2\beta_1^2\beta_2}{\Gamma\left(\alpha_1\right)\Gamma\left(\alpha_2\right)\Gamma\left(\beta_1\right)\Gamma\left(\beta_2\right)}\\ &\times\int_0^\infty G_{2,0}^{0,2}\left(\frac{I_1}{\alpha_2\beta_2I_T}\left|\begin{array}{c}2-\beta_2,2-\alpha_2\\ \cdots\end{array}\right.\right)G_{0,2}^{2,0}\left(\alpha_1\beta_1I_1\left|\begin{array}{c}\cdots\\ \beta_1-2,\alpha_1-2\end{array}\right.\right)dI_1. \end{aligned} \tag{3.38}$$

First utilizing [101, Eq. (4.266)] for performing the integration of the product of two Meijer's G-functions in Eq. (3.38), then by using the properties of Meijer's G-function in [101, Eq. (4.256)] within the resulting expression, we can express Eq. (3.38) as

$$f_{I_T}\left(I_T\right)=\frac{\left(\alpha_1\alpha_2\beta_1\beta_2\right)}{\Gamma(\alpha_1)\Gamma(\alpha_2)\Gamma(\beta_1)\Gamma(\beta_2)}G_{0,4}^{4,0}\left(\alpha_1\alpha_2\beta_1\beta_2I_T\left|\begin{array}{c}\cdots\\ \alpha_1-1,\alpha_2-1,\beta_1-1,\beta_2-1\end{array}\right.\right). \tag{3.39}$$

Observing the similarities between Eq. (3.36) and Eq. (3.39) and using mathematical induction theory [102], we obtain the PDF for K-layer case as

$$\begin{aligned} f_{I_T}\left(I_T\right)=&\frac{\prod_{k=1}^{K}\left(\alpha_k\beta_k\right)}{\prod_{k=1}^{K}\left(\Gamma\left(\alpha_k\right)\Gamma\left(\beta_k\right)\right)}\\ &\times G_{0,2K}^{2K,0}\left(\left(\prod_{k=1}^{K}\left(\alpha_k\beta_k\right)\right)I_T\left|\begin{array}{c}\cdots\\ \alpha_1-1,\cdots,\alpha_K-1,\beta_1-1,\cdots,\beta_K-1\end{array}\right.\right). \end{aligned} \tag{3.40}$$

The mean of I_T (i.e., $E\left[I_T\right] = \int\limits_0^\infty I_T f_{I_T}\left(I_T\right) d_{I_T}$) can be calculated as

$$E\left[I_T\right] = \frac{\prod\limits_{k=1}^{K}\left(\alpha_k\beta_k\right)}{\prod\limits_{k=1}^{K}\left(\Gamma\left(\alpha_k\right)\Gamma\left(\beta_k\right)\right)} \times \int\limits_0^\infty I_T G_{0,2K}^{2K,0}\left(\left(\prod_{k=1}^{K}\left(\alpha_k\beta_k\right)\right) I_T \middle| \begin{matrix} \cdots \\ \alpha_1-1,\cdots,\alpha_K-1,\beta_1-1,\cdots,\beta_K-1 \end{matrix}\right) d_{I_T}. \tag{3.41}$$

To solve the integration in Eq. (3.41), we first use [100, Eq. (07.34.21.0009.01)], then use the recursive property of Gamma function, i.e., $\Gamma\left(x+1\right) = x\Gamma\left(x\right)$ within the resulting expression. This yields $\mu_T = E\left[I_T\right] = \prod_{k=1}^{K} E\left[I_k\right]$. The second moment of I_T can be found as

$$E\left[I_T^2\right] = \frac{\prod\limits_{k=1}^{K}\left(\alpha_k\beta_k\right)}{\prod\limits_{k=1}^{K}\left(\Gamma\left(\alpha_k\right)\Gamma\left(\beta_k\right)\right)} \times \int\limits_0^\infty I_T^2 G_{0,2K}^{2K,0}\left(\left(\prod_{k=1}^{K}\left(\alpha_k\beta_k\right)\right) I_T \middle| \begin{matrix} \cdots \\ \alpha_1-1,\cdots,\alpha_K-1,\beta_1-1,\cdots,\beta_K-1 \end{matrix}\right) d_{I_T}. \tag{3.42}$$

Following similar steps in the above to solve the integral in Eq. (3.42), we obtain $E\left[I_T^2\right] = \prod_{k=1}^{K} E\left[I_k^2\right]$. Therefore, the overall variance can be written as $\sigma_T^2 = \prod_{k=1}^{K} E\left[I_k^2\right] - 1$ noting that $E\left[I_k\right] = 1,\ k = 1,2,\cdots,K$.

To this end, We have modeled the vertical UVLC channel as a concatenation of multiple non-mixing layers and statistically characterized the cascaded vertical channels. In Chapter 4 on the following page, these channels will be used for investigating BER performance as well as the achievable capacity of UVLC systems.

CHAPTER IV

EFFECT OF TURBULENCE ON THE PERFORMANCE OF UVLC SYSTEMS

4.1 Introduction

In Chapter 2 of this dissertation, we have considered only path loss and ignored the effects of turbulence, similar to most of the initial works in the UVLC literature [11, 31, 47] and determined the maximum achievable distance for different water types and investigated the deployment of underwater relay-assisted systems. We have further considered two adaptive algorithms which aim to maximize the throughput while satisfying a pre-defined BER target and investigated the benefits of link adaptation in the context of OFDM-based underwater VLC systems.

In this chapter, we investigate the performance of UVLC system in the presence of turbulence. Particularly, we consider vertical link and derive closed-form expressions for the BER performance of UVLC system described in Section 3.3.2 based on the cascaded LN and GG distributions respectively for weak and moderate/strong turbulence conditions. Then, we analyze the asymptotic BER performance and determine the diversity orders. In addition, we derive closed-form expressions for the average Ergodic capacity of underwater cascaded fading channels under consideration. We present simulation results to confirm the analytical findings.

4.2 Error Rate Performance of Underwater Vertical Links

We consider a VLC system with Intensity Modulation / Direct Detection (IM/DD). Under the assumption of M-ary Pulse-Amplitude Modulation (PAM), conditional BER (conditioned on the fading coefficient) takes the form of

$$BER = F\,\mathrm{erfc}\left(\sqrt{C\gamma I_T^2}\right), \tag{4.1}$$

where $F = (M-1)/(M\log_2(M))$, $C = 3/(2(M-1)(2M-1))$, $\mathrm{erfc}(\cdot)$ is the complementary error function and γ is average SNR [103, Chapter 3]. The average BER can be calculated by averaging BER in Equation (4.1) over the PDF of I_T as

$$\overline{BER} = F\int_0^\infty \mathrm{erfc}\left(\sqrt{C\gamma I_T^2}\right) f_{I_T}(I_T)\,d_{I_T}. \tag{4.2}$$

In the following, we first derive closed-form average BER expressions for cascaded LN and cascaded GG channels. Then, we analyze their asymptotic BER performance and determine the diversity orders.

4.2.1 Weak Turbulence

Solution of Eq. (4.2) under the assumption of LN distribution was previously studied in the context of UVLC [42] as well as in the context of FSO systems [19, 104–106]. Some of these are simply based on converting the integration into a truncated sum by the using of Gauss–Hermite [19, 42, 105] or Gauss–Laguerre quadrature formulas [106] while the complementary error function is replaced with its power series approximation in [104]. Such BER expressions do not provide insight into diversity gains. Here, we aim to derive a new closed-form expression which can be later utilized for diversity order analysis. Replacing Eq. (3.31) on page 46 in Eq. (4.2), we obtain

$$\overline{BER}_{\mathrm{LN}} = \frac{F}{\sqrt{2\pi\sigma_T^2}}\int_0^\infty I_T^{-1}\mathrm{erfc}\left(\sqrt{C\gamma I_T^2}\right)\exp\left(-\frac{(\ln(I_T)-\mu_T)^2}{2\sigma_T^2}\right) d_{I_T}. \tag{4.3}$$

Through a change of integration variable $x = (\mu_T - \ln(I))/\sqrt{2}\sigma_T$, we can express Eq. (4.3) on the previous page as

$$\overline{BER}_{\mathrm{LN}} = \frac{F}{\sqrt{\pi}} \int_{-\infty}^{\infty} \exp\left(-x^2\right) \operatorname{erfc}\left(\sqrt{C\gamma}\exp\left(\mu_T - \sqrt{2}\sigma_T x\right)\right) d_x. \tag{4.4}$$

Using the approximation $\operatorname{erfc}(x) \cong (1/6)\exp\left(-x^2\right) + (1/2)\exp\left(-4x^2/3\right)$ [73], we obtain

$$\overline{BER}_{\mathrm{LN}} \approx \frac{F}{6\sqrt{\pi}} \int_{-\infty}^{\infty} \exp\left(\gamma\phi(x)\right) d_x + \frac{F}{2\sqrt{\pi}} \int_{-\infty}^{\infty} \exp\left(\gamma\psi(x)\right) d_x, \tag{4.5}$$

where $\phi(x)$ and $\psi(x)$ are respectively given as

$$\phi(x) = -C\exp(2\mu_T)\exp\left(-2\sqrt{2}\sigma_T x\right) - \frac{1}{\gamma}x^2. \tag{4.6}$$

$$\psi(x) = -\frac{4}{3}C\exp(2\mu_T)\exp\left(-2\sqrt{2}\sigma_T x\right) - \frac{1}{\gamma}x^2. \tag{4.7}$$

Let $\phi'(x)$ and $\phi''(x)$ denote the first and second-order derivatives of $\phi(x)$. Similarly, define $\psi'(x)$ and $\psi''(x)$ as the first and second-order derivatives of $\psi(x)$. Utilizing Laplace method of integration [107, Appendix D], we can express Eq. (4.5) as

$$\overline{BER}_{\mathrm{LN}} \approx \frac{F/3}{\left(2\gamma|\phi''(x_\phi)|\right)^{1/2}} \exp\left(\gamma\phi(x_\phi)\right) + \frac{F}{\left(2\gamma|\psi''(x_\psi)|\right)^{1/2}} \exp\left(\gamma\psi(x_\psi)\right). \tag{4.8}$$

Here x_ϕ and x_ψ are, respectively, the solution of $\phi'(x) = 0$ and $\phi'(x) = 0$ and found as

$$x_\phi = \frac{1}{2\sqrt{2}\sigma_T} \mathrm{W}\left(4\gamma\sigma_T^2 C\exp(2\mu_T)\right), \tag{4.9}$$

$$x_\psi = \frac{1}{2\sqrt{2}\sigma_T} \mathrm{W}\left(\frac{16}{3}\gamma\sigma_T^2 C\exp(2\mu_T)\right). \tag{4.10}$$

where $\mathrm{W}(\cdot)$ is the Lambert-W function [108]. In Eq. (4.8), $\phi''(x)$ and $\psi''(x)$ are given as

$$\phi''(x) = -8\sigma^2 C\exp(2\mu)\exp\left(-2\sqrt{2}\sigma x\right) - \frac{2}{\gamma}. \tag{4.11}$$

$$\psi''(x) = -\frac{32}{3}\sigma^2 C\exp(2\mu)\exp\left(-2\sqrt{2}\sigma x\right) - \frac{2}{\gamma}. \tag{4.12}$$

Replacing Eq. (4.6) on the preceding page, Eq. (4.7) on the previous page, and Eq. (4.9) on the preceding page-Eq. (4.12) on the previous page in Eq. (4.8) on the preceding page, we obtain the final form of BER as

$$
\begin{aligned}
\overline{BER}_{\mathrm{LN}} \approx & \frac{F\exp\left[-\gamma C\exp\left(2\mu_T-\mathrm{W}\left(4\gamma\sigma_T^2C\exp\left(2\mu_T\right)\right)\right)\right]}{\sqrt{\left(144\gamma\sigma_T^2C\exp\left(2\mu_T-\mathrm{W}\left(4\gamma\sigma_T^2C\exp\left(2\mu_T\right)\right)\right)+36\right)}} \\
&\times\exp\left[-\frac{1}{8\sigma_T^2}\left[\mathrm{W}\left(4\gamma\sigma_T^2C\exp\left(2\mu_T\right)\right)\right]^2\right] \\
&+\frac{F\exp\left[-\frac{4}{3}\gamma C\exp\left(2\mu_T-\mathrm{W}\left(\frac{16}{3}\gamma\sigma_T^2C\exp\left(2\mu_T\right)\right)\right)\right]}{\sqrt{\left(\frac{64}{3}\gamma\sigma_T^2C\exp\left(2\mu_T-\mathrm{W}\left(\frac{16}{3}\gamma\sigma_T^2C\exp\left(2\mu_T\right)\right)\right)+4\right)}} \\
&\times\exp\left[-\frac{1}{8\sigma_T^2}\left[\mathrm{W}\left(\frac{16}{3}\gamma\sigma_T^2C\exp\left(2\mu_T\right)\right)\right]^2\right].
\end{aligned}
\tag{4.13}
$$

4.2.1.1 Asymptotical Analysis over Cascaded LN Channel

In the following, we consider asymptotically high SNR to derive the diversity gain. The decreasing rate of BER over LN fading channels does not converge to a finite value. To address this, Relative Diversity Order (RDO) was proposed in [109] which is basically the ratio between diversity gain of a MIMO system and that of a benchmarking Single-Input Single-Output (SISO) system. While RDO is useful for the analysis of MIMO systems, it is not applicable to the SISO system under consideration. To address this, we propose the so-called incremental diversity order here [110][1]. This is based on the observation that while the decreasing rate of BER does not converge to a finite value, the incremental change in the decreasing rate does converge. *Diversity order* (i.e., the negative slope of the BER curve on a log-log scale) determines how fast the BER changes with SNR. *Incremental diversity order*, on the other hand, determines how fast the diversity order changes with SNR.

[1] More details on the proposed IDO can be found in Section 5.2.

Let $\mathrm{DO}(\gamma) = -\partial \ln \overline{BER}_{\mathrm{LN}} / \partial \ln \gamma$ denote the Diversity Order (DO). IDO will be then defined as

$$\begin{aligned} \mathrm{IDO}(\gamma) &= \partial \mathrm{DO}(\gamma) / \partial \ln \gamma \\ &= -\frac{\partial^2 \ln \overline{BER}_{\mathrm{LN}}}{\partial (\ln \gamma)^2}. \end{aligned} \tag{4.14}$$

Asymptotical Incremental Diversity Order (AIDO) is then simply given by $\mathrm{AIDO} = \lim_{\gamma \to \infty} \mathrm{IDO}(\gamma)$ For high SNR values, we have $\exp(\gamma\phi(x)) \gg \exp(\gamma\psi(x))$. Using this, Eq. (4.13) on the previous page can be approximated as

$$\begin{aligned} \overline{BER}_{\substack{\mathrm{LN} \\ \gamma\to\infty}} \approx & \frac{F \exp\left[-\gamma C \exp\left(2\mu_T - \mathrm{W}\left(4\gamma\sigma_T^2 C \exp\left(2\mu_T\right)\right)\right)\right]}{\sqrt{\left(144\gamma\sigma_T^2 C \exp\left(2\mu_T - \mathrm{W}\left(4\gamma\sigma_T^2 C \exp\left(2\mu_T\right)\right)\right) + 36\right)}} \\ & \times \exp\left[-\frac{1}{8\sigma_T^2}\left[\mathrm{W}\left(4\gamma\sigma_T^2 C \exp\left(2\mu_T\right)\right)\right]^2\right]. \end{aligned} \tag{4.15}$$

Taking the derivative of $-\ln \overline{BER}_{\substack{\mathrm{LN} \\ \gamma\to\infty}}$ in Eq. (4.15) with respect to $\ln\gamma$, diversity order can be approximated for sufficiently high SNR values as

$$\mathrm{DO}(\gamma) \approx A(\gamma) + B(\gamma) + C(\gamma), \tag{4.16}$$

where $A(\gamma)$, $B(\gamma)$ and $C(\gamma)$ are, respectively, defined as

$$A(\gamma) = \frac{2\gamma\sigma_T^2 C \exp\left(2\mu_T - 2\sqrt{2}\sigma_T x_\phi\right)}{\left(4\gamma\sigma_T^2 C \exp\left(2\mu_T - 2\sqrt{2}\sigma_T x_\phi\right) + 1\right)} \left[1 - 2\sqrt{2}\sigma_T \frac{\partial x_\phi}{\partial \ln(\gamma)}\right]. \tag{4.17}$$

$$B(\gamma) = C\gamma \exp\left(2\mu_T - 2\sqrt{2}\sigma_T x_\phi\right) \left[1 - 2\sqrt{2}\sigma_T \frac{\partial x_\phi}{\partial \ln(\gamma)}\right]. \tag{4.18}$$

$$C(\gamma) = 2x_\phi \frac{\partial x_\phi}{\partial \ln(\gamma)}. \tag{4.19}$$

Using the derivative of Lambert-W function, i.e., $d\mathrm{W}(x)/dx = \mathrm{W}(x)/(x[1+\mathrm{W}(x)])$ [108, Eq. (5.15)], the derivative of $\partial x_\phi / \partial \ln(\gamma)$ required in Eq. (4.17)-Eq. (4.19) can be obtained. Replacing the resulting expressions therein, it can be readily verified that both $A(\gamma)$ and $B(\gamma)$ approach zero for high SNR. Utilizing this, Eq. (4.16) reduces to

$$\mathrm{DO}(\gamma) \approx \frac{1}{4\sigma_T^2} \frac{\left(\mathrm{W}\left(4\gamma\sigma_T^2 C \exp\left(2\mu_T\right)\right)\right)^2}{\left(1 + \mathrm{W}\left(4\gamma\sigma_T^2 C \exp\left(2\mu_T\right)\right)\right)}. \tag{4.20}$$

Noting that $\mathrm{W}\left(4\gamma\sigma_T^2 C \exp\left(2\mu_T\right)\right) \gg 1$ for high SNR, Eq. (4.20) on the preceding page can be further simplified as

$$\mathrm{DO}\left(\gamma\right) \approx \frac{1}{4\sigma_T^2} \mathrm{W}\left(4\gamma\sigma_T^2 C \exp\left(2\mu_T\right)\right) \cdot \tag{4.21}$$

The derivative of Eq. (4.21) yields IDO as

$$\mathrm{IDO}\left(\gamma\right) \approx \frac{1}{4\sigma_T^2} \frac{\mathrm{W}\left(4\gamma\sigma_T^2 C \exp\left(2\mu_T\right)\right)}{\left(1+\mathrm{W}\left(4\gamma\sigma_T^2 C \exp\left(2\mu_T\right)\right)\right)} \cdot \tag{4.22}$$

For $\gamma \rightarrow \infty$, AIDO is then obtained as

$$\begin{aligned} \mathrm{AIDO}\left(\gamma\right) &= \lim_{\gamma\rightarrow\infty} \mathrm{IDO}\left(\gamma\right) \\ &= \frac{1}{4\sigma_T^2} = \frac{1}{16\sum_{k=1}^{K} \sigma_{x_k}^2} \cdot \end{aligned} \tag{4.23}$$

This indicates that diversity gain changes inversely with the overall variance of σ_T^2.

4.2.2 Moderate/Strong Turbulence

Under the assumption of cascaded GG turbulence channels, we replace Eq. (3.40) on page 48 in Eq. (4.2) on page 51 to obtain

$$\begin{aligned} \overline{BER}_{\mathrm{GG}} = &\frac{F\,P_{\alpha\beta}}{P_{\Gamma(\alpha)\Gamma(\beta)}} \int_0^\infty \mathrm{erfc}\left(\sqrt{C\gamma I_T^2}\right) \\ &\times G_{0,2K}^{2K,0}\left(P_{\alpha\beta} I_T \left| \begin{matrix} \cdots \\ \alpha_1-1,\cdots,\alpha_K-1,\beta_1-1,\cdots,\beta_K-1 \end{matrix}\right.\right) d_{I_T}, \end{aligned} \tag{4.24}$$

where $P_{\alpha\beta} = \prod_{k=1}^{K}\left(\alpha_k\beta_k\right)$ and $P_{\Gamma(\alpha)\Gamma(\beta)} = \prod_{k=1}^{K}\left(\Gamma\left(\alpha_k\right)\Gamma\left(\beta_k\right)\right)$. If we use [100, Eq. (06.27.26.0006.01)] to express complementary error function in terms of Meijer's G-function, we can write Eq. (4.24) as

$$\begin{aligned} \overline{BER}_{\mathrm{GG}} = &\frac{F\,P_{\alpha\beta}}{\sqrt{\pi}P_{\Gamma(\alpha)\Gamma(\beta)}} \int_0^\infty G_{0,2K}^{2K,0}\left(P_{\alpha\beta} I_T \left| \begin{matrix} \cdots \\ \alpha_1-1,\ldots,\alpha_K-1,\beta_1-1,\ldots,\beta_K-1 \end{matrix}\right.\right) \\ &\times G_{1,2}^{2,0}\left(C\gamma I_T^2 \left| \begin{matrix} 1 \\ 0,\,\frac{1}{2} \end{matrix}\right.\right) dI_T \cdot \end{aligned} \tag{4.25}$$

By using the formulation in [100, Eq. (07.34.21.0013.01)] for the integration of the product of two Meijer's G-functions in Eq. (4.25) on the previous page, we obtain

$$\overline{BER}_{\mathrm{GG}} = \frac{F\, 2^{\sum_{k=1}^{K}(\alpha_k+\beta_k)-2K}}{\sqrt{\pi}\pi^K P_{\Gamma(\alpha)\Gamma(\beta)}} G_{4K+1,2}^{2,4K}\left(\frac{16^K C\gamma}{P_{\alpha\beta}^2}\middle| \begin{matrix}\mathbf{a},1\\ 0,\frac{1}{2}\end{matrix}\right), \tag{4.26}$$

where $\mathbf{a}$ is defined as

$$\mathbf{a} = \left[\frac{1-\alpha_1}{2},\ldots,\frac{1-\alpha_K}{2},\frac{2-\alpha_1}{2},\ldots,\frac{2-\alpha_K}{2},\frac{1-\beta_1}{2},\ldots,\frac{1-\beta_K}{2},\frac{2-\beta_1}{2},\ldots,\frac{2-\beta_K}{2}\right]_{1\times 4K}. \tag{4.27}$$

Special Case: As a sanity check, we consider the Horizontal link/single-layer case (i.e., $K=1$). Recall that α_h and β_h denote, respectively, the effective number of large-scale and small-scale cells of the scattering processes. Replacing $K=1$ in Eq. (4.26) and Eq. (4.27), we obtain

$$\overline{BER}_{\mathrm{GG_{SL}}} = \frac{F\, 2^{(\alpha_h+\beta_h)-2}}{\sqrt{\pi}\pi\Gamma(\alpha_h)\Gamma(\beta_h)} G_{5,2}^{2,4}\left(\frac{16C\gamma}{\alpha_h^2\beta_h^2}\middle| \begin{matrix}\frac{1-\alpha_h}{2},\frac{2-\alpha_h}{2},\frac{1-\beta_h}{2},\frac{2-\beta_h}{2},1\\ 0,\frac{1}{2}\end{matrix}\right) \tag{4.28}$$

which coincides with [111, Eq. (32)] earlier reported in the literature for single-layer GG channels.

4.2.2.1 Asymptotical Analysis over Cascaded GG Channel

Following the conventional definition of diversity order, we can write

$$\mathrm{DO}(\gamma) = -\frac{\partial \ln \overline{BER}_{\mathrm{GG}}}{\partial \ln\gamma}. \tag{4.29}$$

Asymptotical diversity order (ADO) is then simply given by $\mathrm{ADO} = \lim_{\gamma\to\infty}\mathrm{DO}(\gamma)$. To obtain ADO, we first express Meijer's G-function in Eq. (4.26) in terms of generalized hypergeometric function [100, Eq. (07.34.26.0005.01)]. Then by using the properties of generalized hypergeometric function in [100, Eq. (07.31.02.0001.01)] and ignoring the higher-order terms, we obtain

$$\underset{\gamma\to\infty}{\overline{BER}_{\mathrm{GG}}} = \frac{F\, 2^{\sum_{k=1}^{K}(\alpha_k+\beta_k)-2K}}{\sqrt{\pi}\pi^K P_{\Gamma(\alpha)\Gamma(\beta)}} \sum_{h=1}^{4K} \frac{\Gamma(1.5-a_h)\prod\limits_{\substack{j=1\\ j\neq h}}^{4K}\Gamma\left(a_h-a_j\right)}{(1-a_h)} \left(\frac{16^K C}{P_{\alpha\beta}^2}\right)^{a_h-1} \gamma^{a_h-1}. \tag{4.30}$$

As $\gamma \to \infty$, the term where γ is raised to the largest power will dominate the performance. Therefore, Eq. (4.30) on the previous page can be simplified as

$$\underset{\gamma\to\infty}{\overline{BER}_{\mathrm{GG}}} = \frac{F\, 2^{\sum_{k=1}^{K}(\alpha_k+\beta_k)-2K}}{G_d\sqrt{\pi}\pi^K P_{\Gamma(\alpha)\Gamma(\beta)}} \times \left(\Gamma(0.5+G_d)\prod_{\substack{j=1\\ a_j\neq\max(\mathbf{a})}}^{4K}\Gamma(1-a_j-G_d)\right)\left(\frac{P_{\alpha\beta}^2}{16^K C}\right)^{G_d}\gamma^{-G_d}, \tag{4.31}$$

where $G_d = 0.5\min(\alpha_1,\alpha_2,\ldots,\alpha_K,\beta_1,\beta_2,\ldots,\beta_K)$. Taking the derivative of $-\ln\underset{\gamma\to\infty}{\overline{BER}_{\mathrm{GG}}}$ with respect to $\ln\gamma$, the negative slope of $\ln\underset{\gamma\to\infty}{\overline{BER}_{\mathrm{GG}}}$ is found to be G_d, i.e.,

$$\mathrm{ADO} = G_d = 0.5\min(\alpha_1,\alpha_2,\ldots,\alpha_K,\beta_1,\beta_2,\ldots,\beta_K)\cdot \tag{4.32}$$

This indicates that the diversity gain is determined by the layer with the minimum effective number of large-/small-scale cells in cascaded GG channels. This is in contrast to cascaded LN channels where all layers contribute to the diversity order.

4.3 Ergodic Capacity of Underwater Vertical Links

Instantaneous Ergodic channel capacity for IM/DD channels can be approximated as [112]

$$C \approx \frac{1}{2\ln(2)}\ln\left(1+\frac{\exp(1)\gamma}{2\pi}I_T^2\right)\cdot \tag{4.33}$$

The average capacity can be calculated by taking expectation of Eq. (4.33) with respect I_T as

$$\overline{C} \approx \frac{1}{2\ln(2)}\int_0^\infty \ln\left(1+\frac{\exp(1)\gamma}{2\pi}I_T^2\right) f_{I_T}(I_T)\, d_{I_T}\cdot \tag{4.34}$$

In the following, we derive closed-form expressions for cascaded LN and cascaded GG channels.

4.3.1 Weak Turbulence

Under the assumption of cascaded LN turbulence channels, we first replace Eq. (3.31) on page 46 in Eq. (4.34) on the preceding page and apply a change of integration variable $x = \ln(I_T)$. This yields

$$\overline{C}_{\text{LN}} \approx \int_{-\infty}^{\infty} \frac{1}{2\ln(2)} \ln\left(1 + \frac{\exp(1)\,\gamma}{2\pi}\exp(2x)\right) \frac{1}{\sqrt{2\pi\sigma_T^2}} \exp\left(-\frac{(x-\mu_T)^2}{2\sigma_T^2}\right) d_x. \tag{4.35}$$

Using Holtzmann approach, the solution of this integral can be approximated by [113, Eq. (2.5) & Eq. (2.15)] as

$$\begin{aligned}\overline{C}_{\text{LN}} \approx & \frac{1}{3\ln(2)} \ln\left(1 + \frac{\exp(1)\,\gamma}{2\pi}\exp(2\mu_T)\right) \\ & + \frac{1}{12\ln(2)} \ln\left(1 + \frac{\exp(1)\,\gamma}{2\pi}\exp\left(2\mu_T + 2\sqrt{3}\sigma_T\right)\right) \\ & + \frac{1}{12\ln(2)} \ln\left(1 + \frac{\exp(1)\,\gamma}{2\pi}\exp\left(2\mu_T - 2\sqrt{3}\sigma_T\right)\right).\end{aligned} \tag{4.36}$$

4.3.2 Moderate/Strong Turbulence

Under the assumption of cascaded GG turbulence channels, we replace Eq. (3.40) on page 48 in Eq. (4.34) on the preceding page to obtain

$$\begin{aligned}\overline{C}_{\text{GG}} \approx & \frac{P_{\alpha\beta}}{2\ln(2)\,P_{\Gamma(\alpha)\Gamma(\beta)}} \int_0^{\infty} \ln\left(1 + \frac{\exp(1)\,\gamma}{2\pi} I_T^2\right) \\ & \times G_{0,2K}^{2K,0}\left(P_{\alpha\beta}\, I_T \,\middle|\, \begin{matrix} \cdots \\ \alpha_1 - 1, \cdots, \alpha_K - 1, \beta_1 - 1, \cdots, \beta_K - 1 \end{matrix}\right) d_{I_T}.\end{aligned} \tag{4.37}$$

Using [100, Eq. (07.34.03.0456.01)] to express natural logarithm in terms of Meijer's G-function, we can write Eq. (4.37) as

$$\begin{aligned}\overline{C}_{\text{GG}} \approx & \frac{P_{\alpha\beta}}{2\ln(2)\,P_{\Gamma(\alpha)\Gamma(\beta)}} \int_0^{\infty} G_{0,2K}^{2K,0}\left(P_{\alpha\beta}\, I_T \,\middle|\, \begin{matrix} \cdots \\ \alpha_1 - 1, \cdots, \alpha_K - 1, \beta_1 - 1, \cdots, \beta_K - 1 \end{matrix}\right) \\ & \times G_{2,2}^{1,2}\left(\frac{\exp(1)\,\gamma}{2\pi} I_T^2 \,\middle|\, \begin{matrix} 1,1 \\ 1,0 \end{matrix}\right) d_{I_T}.\end{aligned} \tag{4.38}$$

By using the formulation in [100, Eq. (07.34.21.0013.01)] for the integration of the product of two Meijer's G-functions in Eq. (4.38) on the preceding page, we obtain

$$\overline{C}_{\mathrm{GG}} \approx \frac{2^{\sum_{k=1}^{K}(\alpha_k+\beta_k)-2K-1}}{\ln(2)\,\pi^K P_{\Gamma(\alpha)\Gamma(\beta)}} G^{1,4K+2}_{4K+2,2}\left(\frac{\exp(1)\,2^{4K-1}\gamma}{\pi P^2_{\alpha\beta}}\middle|\begin{array}{c}\mathbf{a},1,1\\1,0\end{array}\right), \tag{4.39}$$

where $\mathbf{a}$ is previously defined in Eq. (4.27) on page 56.

4.4 Results and Discussions

In this section, we present numerical results to corroborate our derived closed-form BER and Ergodic capacity expressions. To verify our BER derivations, we also include Monte Carlo simulations. BER estimation include typical steps of generation of bits, mapping to modulation symbols, generation of fading coefficients and noise terms, and estimation of transmitted modulation symbols and demapping to bits. The BER estimation is then based on the comparison of transmitted and retrieved bits. The critical issue in our simulations is the generation of proper fading coefficients with the desired value of σ_k^2 for LN turbulence channel and the desired values of α_k and β_k for GG turbulence channel. As discussed in Sections 4.2.1 and 4.2.2 these values are related to the scintillation index denoted by $\sigma_{I_k}^2$. The scintillation index can be calculated by Eq. (3.19) on page 39 in conjunction with the underwater spatial power spectrum model presented in Eq. (3.16) on page 38. After the calculation of scintillation index, log-amplitude variance ($\sigma_{x_k}^2$) can be calculated using Eq. (3.30) on page 46. Similarly, α_k and β_k can be calculated from Eq. (3.33) on page 47 and Eq. (3.34) on page 47, respectively. In our study, we consider Pacific Ocean at high latitudes which is known to have strong stratification [62, 114] and assume two, three and four layers. Unless otherwise mentioned, we use the channel parameters listed in Table 4 on the next page.

Table 4: Simulation parameters.

Dissipation rate of mean-squared temperature	χ_T	LN	1×10^{-5}K^{2}s^{-3}
		GG	5×10^{-5}K^{2}s^{-3}
Dissipation rate of turbulent kinetic energy	ε		1×10^{-1}m^{2}s^{-3}
Wavelength	λ		0.530μm
Thermal expansion coefficient	A_k		Computed by TEOS[1]
Saline contraction coefficient	B_k		Computed by TEOS
Kinematic viscosity	υ_k		Computed by FVCOM[2]
Molecular thermal diffusivity	D_{T_k}		Computed by FVCOM
Molecular salinity diffusivity	D_{S_k}		$D_{S_k}\approx0.01D_{T_k}$

[1] **TEOS:** MATLAB Oceanographic Toolbox of International Thermodynamic Equation of Seawater-2010 (TEOS-10 standard).
[2] **FVCOM:** MATLAB Finite Volume Community Ocean Model-toolbox.

In Fig. 14 on the following page, we present the BER performance of a vertical underwater link with a transmission range of d_T= 60 m. The source is placed at the sea surface, i.e., d_0= 0 m. Under the assumption that the thickness of each layer is 30 m, the vertical link is modeled with two independent layers. In Fig. 14(a) on the next page, we consider cascaded LN fading channels and plot the derived approximate BER expression in Eq. (4.13) on page 53 along with Monte-Carlo simulation results. Our results demonstrate that the derived expression provides almost excellent match in all SNR region. As a benchmark, we further include the BER performance of a hypothetical vertical link with constant turbulent strength over the transmission range. The constant log-amplitude variance of $\sigma^2_{x_T}=21.88\times10^{-2}$ is computed based on averaging temperature and salinity values over the transmission range. It is observed that this simplifying assumption overestimates the actual BER values. In Fig. 14(b) on the next page, we consider cascaded GG fading channels and verify the accuracy of the derived BER expression in Eq. (4.26) on page 56 which matches with Monte-Carlo simulation results. We also include the BER performance of a hypothetical vertical link with constant turbulent strength whose corresponding channel parameters are found as $(\alpha,\beta)=(5.05,1.16)$. Unlike Fig. 14(a) on the next page, it is observed that there is underestimation of the actual BER values at low SNR and overestimation of the actual BER values at high SNR.

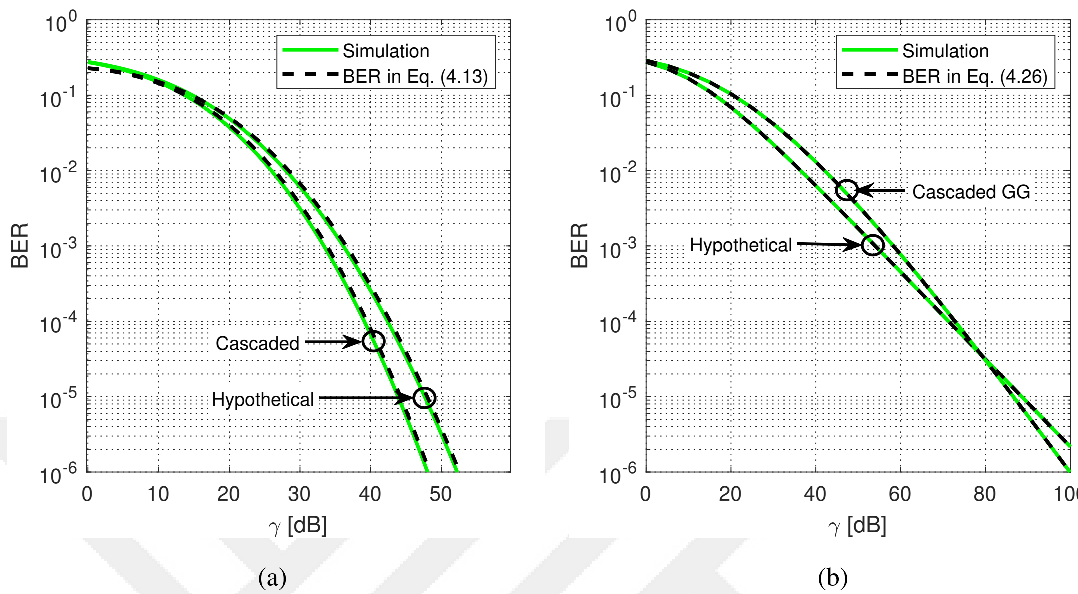

Figure 14: BER performance for vertical link with two layers: (a) cascaded LN turbulence channel and (b) cascaded GG turbulence channel.

In Fig. 15 on the following page, we present the effect of layer thickness on BER performance over cascaded LN and GG channels. We assume a link distance of $d_T =$ 60 m and consider different layer thicknesses of $d_k =$15 m, 20 m and 30 m[2]. It can be observed that performance discrepancy between actual and hypothetical cases increases as the number of layers increases. For example, consider the 2-layer case, i.e., d_k = 30 m, k =1, 2. For cascaded LN fading channels, SNR of 33.71 dB is required to maintain BER $= 10^{-3}$ while averaging approach estimates SNR of 36.12 dB, i.e., overestimation. Relative error percentage therefore becomes 7.15%. This climbs to 15.99% and 22.31% for 3-layer and 4-layer cases, respectively. For cascaded GG fading channels, SNR of 58.29 dB is required to maintain BER $= 10^{-3}$ while averaging approach estimates SNR of 54.01 dB, i.e., underestimation. Relative error percentage is therefore calculated as -6.31%. This becomes -4.06% and 0.29% for 3-layer and 4-layer cases, respectively. It can be further observed

[2]The layer of thickness depends on the location and season and changes with the degree of ocean stratification [92, Chapter 8].

that, for both channels at high SNR values, the more the layers the less the BER values. This is due to the fact that layering due to water stratification results in virtual hops and benefits of multi-hop transmission can be realized through the inherent characteristics of vertical propagation.

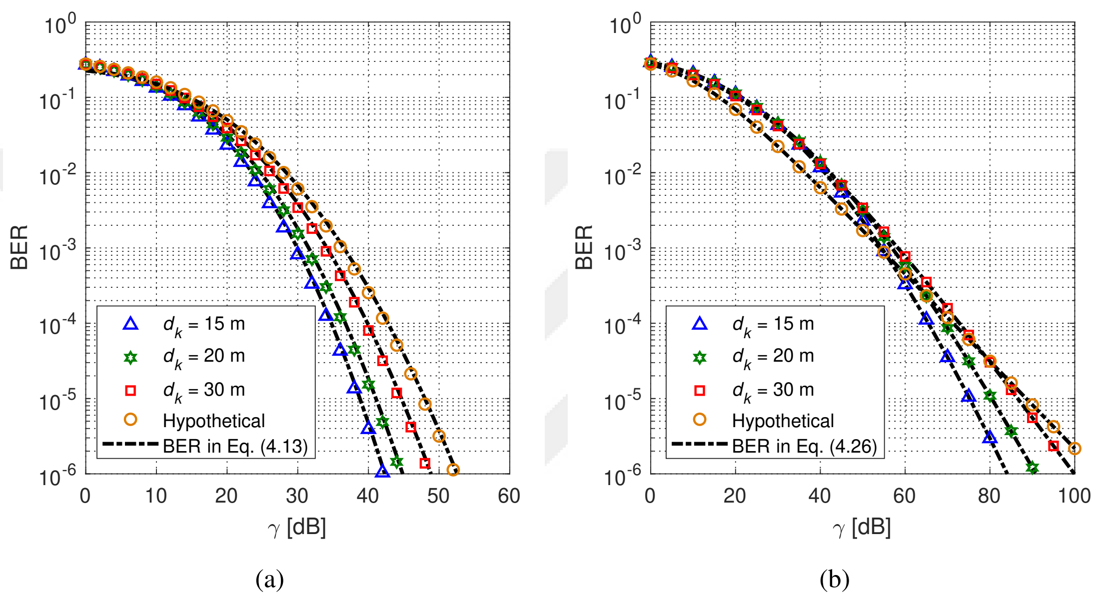

Figure 15: Effect of layer thickness on BER performance: (a) cascaded LN turbulence channel and (b) cascaded GG turbulence channel.

In Fig. 16 on the next page, we investigate diversity gains achieved over cascaded LN and GG fading channels. In Fig. 16(a) on the following page, we plot the exact IDO based on the numerical integration of Eq. (4.14) on page 54 along with the derived expression in Eq. (4.22) on page 55 for cascaded LN channels. We assume a link distance of $d_T = 60$ m and consider layer thicknesses of $d_k = 15$ m, 20 m and 30 m. Our results show that, in lower SNR region, there is some discrepancy, but as SNR goes up, the derived expression in Eq. (4.22) on page 55 coincides with the exact expression in Eq. (4.14) on page 54. It is also observed that the IDO converges to 0.35, 0.44, and 0.52, respectively for 2, 3 and 4-layer cases as predicted by the derived AIDO in Eq. (4.23) on page 55. In Fig. 16(b) on the following page, we present the diversity orders over cascaded GG fading channels.

It is observed that DO converges to 0.81, 1.18, and 1.68, respectively for 2, 3 and 4-layer cases. As predicted by the derived expression in Eq. (4.32) on page 57, the diversity gain is determined by the minimum effective number of large-scale and small-scale cells of the scattering processes.

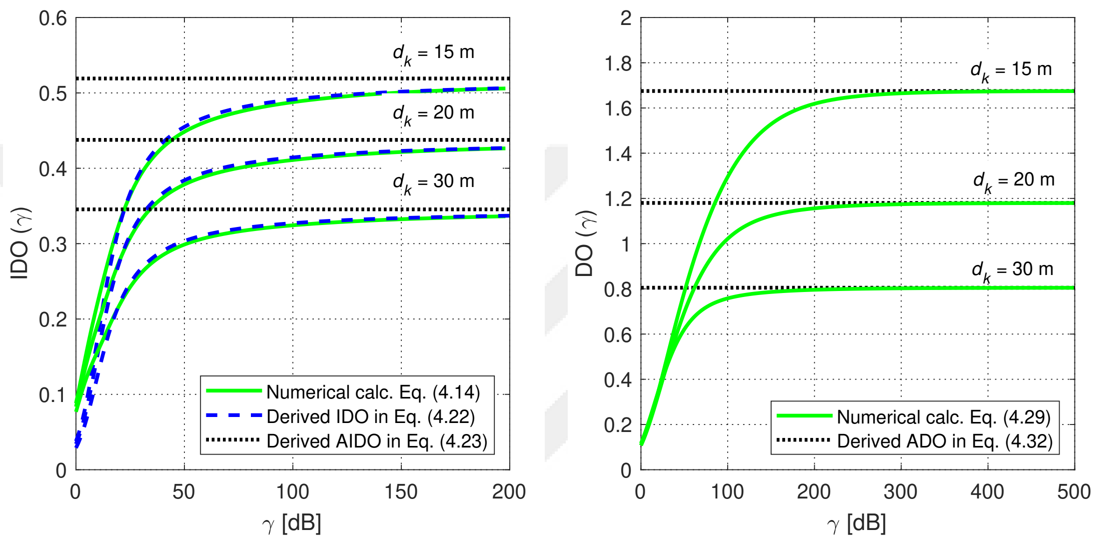

(a) (b)

Figure 16: Asymptotic behavior of BER: (a) cascaded LN turbulence channel and (b) cascaded GG turbulence channel.

In Fig. 17 on the following page, we present average Ergodic capacity of a two-layer vertical underwater link with a transmission range of $d_T = 60$ m. Similar to Fig. 13 on page 46, we consider a hypothetical vertical link with constant turbulent strength over the transmission range as a benchmark. In Fig. 17(a) on the following page, we consider cascaded LN fading channels and plot the derived capacity expression in Eq. (4.36) on page 58 along with the exact expression in Eq. (4.35) on page 58 (calculated through numerical means). In Fig. 17(b) on the next page, we consider cascaded GG fading channels and plot the derived and exact capacity expressions in Eq. (4.39) on page 59 and Eq. (4.37) on page 58, respectively. Our results demonstrate that the derived expressions provide excellent match for both turbulence channels confirming the accuracy of our derivations. It can be further observed from Fig. 17(a) that the effect of layering on the capacity of cascaded LN channels is almost negligible. In comparison to LN channels, the effect of layering is pronounced more in cascaded GG channels, but it is still not significant. For example, assuming LN channels, SNR of 36.87 dB is required to achieve capacity of 5 bps/Hz while SNR of 37.52 dB is required for a hypothetical single-layer case. Assuming GG channels, SNR of 41.50 dB is required to achieve capacity of 5 bps/Hz while SNR of 38.70 dB is required for a hypothetical single-layer case.

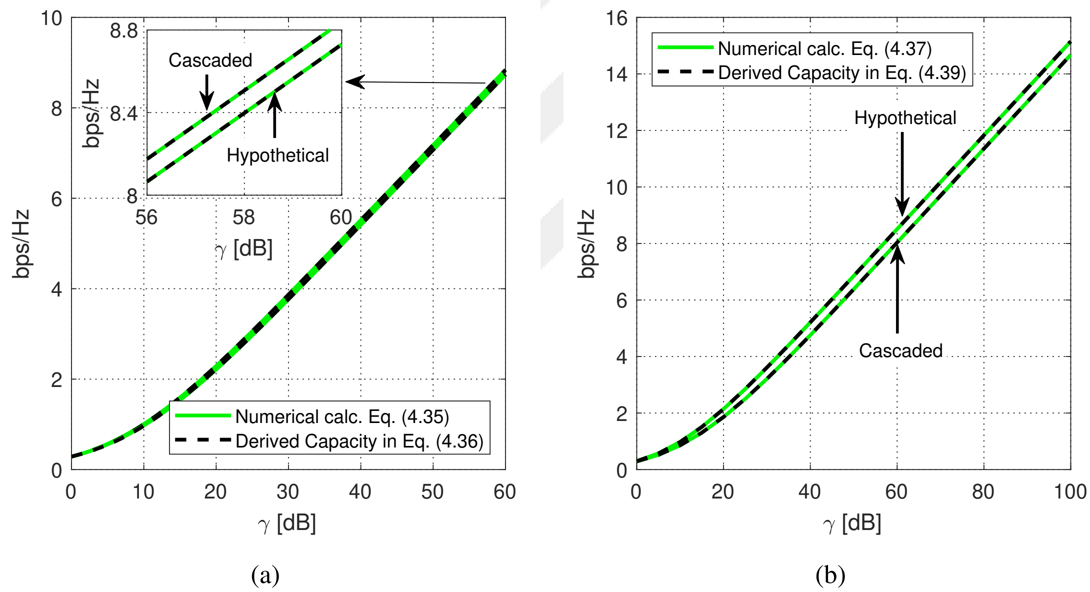

Figure 17: Capacity for vertical link: (a) cascaded LN turbulence channel and (b) cascaded GG turbulence channel.

CHAPTER V

FADING MITIGATION TECHNIQUES

5.1 Introduction

In Chapter 4, we have investigated the performance of UVLC system in the presence of turbulence. To combat the degrading effects of underwater turbulence, deployment of multiple transmitters and/or receivers in UVLC was proposed in [16–18] to extract the spatial diversity. This concept has been widely adopted in the context of FSOC [19–21]. As an alternative, TLS can be considered where only one of the transmitters is active. This method is able to extract full diversity while significantly reducing the complexity of the front-end. The same concept was earlier studied in the context of terrestrial FSO links [22–24]. Since coverage of the communication system is not increased in these fading mitigation techniques, Multi-hop serial-relaying, which improves the performance over fading channels by employing intermediate relays has been adopted in [42].

In the performance characterization of communication systems over fading channels, one of the major metrics is DO, which is basically the slope of bit error or outage probability against SNR on a log-log scale. However, the decreasing rate of error probability over LN fading channels does not converge to a finite value. That makes applying the concept of DO over LN channels is a big challenge. To address this, Asymptotical Relative Diversity Order (ARDO) was proposed in [115]. Since then, ARDO has been widely used in the literature to analyze the performance of MIMO and relay-assisted FSO systems [116–120] as well as some MIMO and cooperative wireless (radio frequency) systems [121–123] over LN fading channels.

In this Chapter, we propose the concept of IDO in order to quantify diversity gains of communication systems over LN fading channels. IDO is defined as the incremental change in the decreasing rate of BER in log-log scale and determines how fast the diversity order changes with SNR. Unlike ARDO widely used in the literature, calculation of IDO does not require the need of a benchmarking scheme and reflects the channel-dependent parameters in diversity gains.

The rest of this chapter is organized as follow. In Section 5.2, we consider a MIMO UVLC system over LN channels, derive a novel closed-form BER expression, introduce the concept of IDO and quantify IDO. In Section 5.3, we consider an UVLC system with GTLS where the n^{th} best laser is selected among the available N lasers and determine the so-called IDO.

5.2 *Multiple-Input Multiple-Output system*

UVLC communication systems experience turbulence-induced fading, which is typically modelled by LN distribution. In this section, we consider MIMO as a fading mitigation technique. Since the decreasing rate of error probability over LN fading channels does not converge to a finite value, we propose the concept of IDO, which is defined as the incremental change in the decreasing rate of BER on a log-log scale. We derive a novel closed-form BER expression in terms of Lambert-W function and obtain IDO as a function of the number of laser sources, the number of photo-detectors and the variance of the log-amplitude coefficient. We further present numerical results to validate the derived BER expression and associated IDO.

5.2.1 System Model

We consider a MIMO UVLC system with IM/DD. We assume that the system is equipped with N_{S} transmitters (laser sources) and N_{D} receivers (photodetectors). Repetition coding is employed, which is known to be quasi-optimal for IM/DD systems [124]. Let x denote the transmitted unipolar M-ary PAM (M-PAM) symbol. The received signal at the j^{th}

photodetector can be written as

$$y_j = \frac{\sqrt{P_{\mathrm{te}}/N_{\mathrm{S}}}}{N_{\mathrm{D}}}\eta r h x \sum_{i=1}^{N_{\mathrm{S}}} I_{ij} + w_j, \quad j = 1, 2, \cdots, N_{\mathrm{D}} \;, \tag{5.1}$$

where P_{te} is the average electrical transmit power, η is electro-optical conversion efficiency of the laser diode, r is the opto-electrical responsivity of the photodetector, w_j is the AWGN term with zero mean and noise variance of σ_{nj}^2 and h is the channel attenuation term. The scaling factor $1/N_{\mathrm{S}}$ is included to ensure that the total average electrical transmit power of the MIMO system is the same as that of a SISO system for a fair comparison. Similarly, the scaling factor $1/N_{\mathrm{D}}$ is introduced to ensure that the sum of the N_{D} photodetector areas is equal to the area of the single photodetector in the reference SISO system [125]. In Eq. (5.1), I_{ij} represents the fading channel coefficient between the i^{th} laser and the j^{th} photodetector. Under the assumption of Independent and Identical Distributed (i.i.d) LN turbulence, the PDF of I_{ij} can be written as [94]

$$f_{I_{ij}}(I_{ij}) = \frac{1}{I_{ij}\sqrt{2\pi\sigma^2}} \exp\left(-\frac{\left(\ln\left(I_{ij}\right)-\mu\right)^2}{2\sigma^2}\right), \; I_{ij} > 0 \tag{5.2}$$

where $\mu = 2\mu_x$ and $\sigma^2 = 4\sigma_x^2$. Here, μ_x and σ_x^2 denote, respectively, the mean and variance of the log-amplitude coefficient $X_{ij} = 0.5\ln\left(I_{ij}\right)$. For making sure that the fading coefficient will not affect the average power, fading coefficient is normalized (i.e. $\mathrm{E}\left[I_{ij}\right] = 1$) which implies $\mu_x = -\sigma_x^2$.

Equal Gain Combining (EGC) is employed at the receiver. Therefore, the destination node adds the outputs of the photodetectors. This gives

$$y = \frac{\sqrt{P_{\mathrm{te}}/N_{\mathrm{S}}}}{N_{\mathrm{D}}}\eta r h x \left(\sum_{j=1}^{N_{\mathrm{D}}}\sum_{i=1}^{N_{\mathrm{S}}} I_{ij}\right) + w, \tag{5.3}$$

where the EGC output noise is defined by $w = \sum_{j=1}^{N_D} w_j$ with a noise variance of $\sigma_N^2 = \sum_{j=1}^{N_D} \sigma_{nj}^2$. Since the noise variance is proportional to the aperture area size and we assume the same detection area for all photodetectors, noise variance will be identical for all photodetectors, i.e., $\sigma_{nj}^2 = \sigma_N^2/N_{\mathrm{D}}\;,\; j = 1,\; 2, \cdots, N_{\mathrm{D}}$.

5.2.2 Derivation of BER

The average BER of MIMO UVLC system can be calculated through the multi dimensional integral given by

$$\begin{aligned}\overline{BER} = F \int_0^{\infty}\int_0^{\infty}\cdots\int_0^{\infty} \operatorname{erfc}\left(\sqrt{C\gamma}\left(\sum_{j=1}^{N_{\mathrm{D}}}\sum_{i=1}^{N_{\mathrm{S}}} I_{ij}\right)\right) \\ \times f_{I_{11},I_{12},\cdots,I_{N_{\mathrm{D}}N_{\mathrm{S}}}}\left(I_{11},I_{12},\cdots,I_{N_{\mathrm{D}}N_{\mathrm{S}}}\right) d_{I_{11}} d_{I_{12}} \cdots d_{I_{N_{\mathrm{D}}N_{\mathrm{S}}}},\end{aligned} \tag{5.4}$$

where $f_{I_{11},I_{12},\cdots,I_{N_{\mathrm{D}}N_{\mathrm{S}}}}\left(I_{11},I_{12},\cdots,I_{N_{\mathrm{D}}N_{\mathrm{S}}}\right)$ is the joint PDF of vector $\mathbf{I} = \left(I_{11},I_{12},\cdots,I_{N_S N_D}\right)$, $F = (M-1)/(M\log_2(M))$ and $C = 3/(2(M-1)(2M-1))$. In Eq. (5.4), γ stands for fading-free (average) SNR and is defined as $\gamma = P_{\mathrm{te}}\eta^2 r^2 h^2/N_{\mathrm{S}}N_D^2\sigma_N^2$.

Let us define $I = \sum_{j=1}^{N_{\mathrm{D}}}\sum_{i=1}^{N_{\mathrm{S}}} I_{ij}$. The summation of i.i.d LN random variables can be efficiently approximated by another LN random variable [126, 127]. The accuracy of approximation depends on the number of underlying variables and their variance values. Romeo method was proposed for the moderately broad LN distribution and is accurate for the range of $0 \le \sigma \le 1.25$ [128]. Based on the Romeo method [128], the PDF of I can be approximated as

$$f_I(I) \approx \frac{1}{I\sqrt{2\pi\sigma_{\mathrm{MIMO}}^2}} \exp\left(-\frac{\left(\ln(I)-\mu_{\mathrm{MIMO}}\right)^2}{2\sigma_{\mathrm{MIMO}}^2}\right), \tag{5.5}$$

where the variance and mean of equivalent MIMO channel σ_{MIMO}^2 and μ_{MIMO} are obtained as $\sigma_{\mathrm{MIMO}}^2 = \ln\left[1 - N_S^{-1}N_D^{-1} + N_S^{-1}N_D^{-1}\exp\left(\sigma^2\right)\right]$ and $\mu_{\mathrm{MIMO}} = \ln(N_S N_D) + \mu + \left(\sigma^2 - \sigma_{\mathrm{MIMO}}^2\right)/2$.

Replacing the LN approximation, we reduce Eq. (5.4) to a single integral in the form of $\overline{BER} \approx F\int_0^{\infty} \operatorname{erfc}\left(\sqrt{C\gamma I}\right) f_I(I)\, d_I$. This still does not yield a closed-form exact solution. To address this, different methods were adopted in the literature to obtain approximate solutions. Some of these derivations are simply based on converting the integration into a truncated sum such as Gauss–Hermite quadrature [105] or Gauss–Laguerre quadrature [106]. In [104], the complementary error function is replaced with its power series approximation. The final form of BER expressions in these works [104–106] is basically a summation of terms and does not lend itself taking the derivative with respect to SNR required for diversity order analysis. In the following, we derive a novel approximate BER in terms of Lambert-W function.

Utilizing Eq. (5.5) on the preceding page, we obtain the BER as

$$\overline{BER} \approx \frac{F}{\sqrt{\pi}} \int\limits_{-\infty}^{\infty} \exp\left(-z^2\right) \operatorname{erfc}\left(\sqrt{C\gamma} \exp\left(\mu_{\text{MIMO}} - \sqrt{2}\sigma_{\text{MIMO}} z\right)\right) d_z, \tag{5.6}$$

where $z = (\mu - \ln(I))/\sqrt{2}\sigma_{\text{MIMO}}$. For sufficiently high values of SNR, we can use $\operatorname{erfc}(z) \lessapprox \left(z\sqrt{\pi}\right)^{-1} \exp\left(-z^2\right)$, $z \gg 0$ [129, Eq. (4.2)] and write Eq. (5.6) as

$$\overline{BER} \approx \frac{F}{\pi\sqrt{C\gamma}} \int_0^{\infty} \exp\left(\Upsilon(z)\right) d_z, \tag{5.7}$$

where $\Upsilon(z) = -C\gamma \exp\left(2\mu_{\text{MIMO}} - 2\sqrt{2}\sigma_{\text{MIMO}} z\right) - z^2 + \sqrt{2}\sigma_{\text{MIMO}} z - \mu_{\text{MIMO}}$. Using Laplace method of integration [107, Appendix D], we can solve Eq. (5.7) to obtain

$$\overline{BER} \approx \sqrt{\frac{2F^2}{C\pi\gamma|\Upsilon''(z_\circ)|}} \exp\left(\Upsilon(z_\circ)\right), \tag{5.8}$$

where $z_\circ$ is the solution of the first-order derivative of $\Upsilon(z)$ and $\Upsilon''(z)$ is the second-order derivative of $\Upsilon(z)$. Taking the derivative of $\Upsilon(z)$ and setting it to zero, we can obtain

$$z_\circ = \frac{1}{2\sqrt{2}\sigma_{\text{MIMO}}} \ln\left(\frac{4\sigma^2_{\text{MIMO}} C\gamma \exp\left(2\mu_{\text{MIMO}}\right)}{\mathrm{W}\left(4\sigma^2_{\text{MIMO}} C\gamma \exp\left(2\mu_{\text{MIMO}} - 2\sigma^2_{\text{MIMO}}\right)\right)}\right), \tag{5.9}$$

where $\mathrm{W}(\cdot)$ denotes the Lambert-W function [108]. If we replace $\Upsilon(z_\circ)$ and $\Upsilon''(z_\circ)$ in Eq. (5.8), we obtain the final form of BER as

$$\overline{BER} \approx \frac{F \exp\left(-z_\circ^2 + \sqrt{2}\sigma_{\text{MIMO}} z_\circ - C\gamma \exp\left(2\mu_{\text{MIMO}} - 2\sqrt{2}\sigma_{\text{MIMO}} z_\circ\right) - \mu_{\text{MIMO}}\right)}{\sqrt{C\pi\gamma\left(4\sigma^2_{\text{MIMO}} C\gamma \exp\left(2\mu_{\text{MIMO}} - 2\sqrt{2}\sigma_{\text{MIMO}} z_\circ\right) + 1\right)}}. \tag{5.10}$$

5.2.3 Incremental Diversity Order

The conventional DO is defined as [115]

$$\mathrm{DO} = \lim_{\gamma\to\infty} \mathrm{DO}(\gamma) = -\lim_{\gamma\to\infty} \frac{\partial \ln \overline{BER}}{\partial \ln \gamma}. \tag{5.11}$$

Replacing Eq. (5.10) on the preceding page in Eq. (5.11) on the previous page and taking the derivative, we have

$$
\begin{aligned}
\mathrm{DO} \approx & \lim_{\gamma\to\infty}\left(\frac{2\sigma_{\mathrm{MIMO}}^2 C\exp\left(2\mu_{\mathrm{MIMO}}\right)\gamma\exp\left(-2\sqrt{2}\sigma_{\mathrm{MIMO}} z_\circ\right)\left(1-2\sqrt{2}\sigma_{\mathrm{MIMO}} z'_\circ\right)}{\left(4\sigma_{\mathrm{MIMO}}^2 C\exp\left(2\mu_{\mathrm{MIMO}}\right)\gamma\exp\left(-2\sqrt{2}\sigma_{\mathrm{MIMO}} z_\circ\right)+1\right)}\right) \\
& + \lim_{\gamma\to\infty}\left(C\exp\left(2\mu_{\mathrm{MIMO}}\right)\gamma\exp\left(-2\sqrt{2}\sigma_{\mathrm{MIMO}} z_\circ\right)\left(1-2\sqrt{2}\sigma_{\mathrm{MIMO}} z'_\circ\right)\right) \\
& + \lim_{\gamma\to\infty}\left(\frac{1}{2}+2z_\circ z'_\circ-\sqrt{2}\sigma_{\mathrm{MIMO}} z'_\circ\right).
\end{aligned}
\tag{5.12}
$$

In Eq. (5.12), $z'_\circ = \partial z_\circ/\partial \ln(\gamma)$. Using the derivative of Lambert-W function [108, Eq. (5.15)], we calculate

$$
z'_\circ = \frac{1}{2\sqrt{2}\sigma_{\mathrm{MIMO}}}\left(\frac{\mathrm{W}\left(4\sigma_{\mathrm{MIMO}}^2 C\gamma\exp\left(2\mu_{\mathrm{MIMO}}-2\sigma_{\mathrm{MIMO}}^2\right)\right)}{1+\mathrm{W}\left(4\sigma_{\mathrm{MIMO}}^2 C\gamma\exp\left(2\mu_{\mathrm{MIMO}}-2\sigma_{\mathrm{MIMO}}^2\right)\right)}\right). \tag{5.13}
$$

By replacing Eq. (5.13) in Eq. (5.12), it can be readily verified that, for high SNR values, the first two terms in Eq. (5.12) approach zero and the third term reduces to $2z_\circ z'_\circ$. Therefore, DO can be written as

$$
\mathrm{DO} \approx \lim_{\gamma\to\infty}\left(\frac{1}{4\sigma_{\mathrm{MIMO}}^2}\right)\left(\ln\left[\frac{4\sigma_{\mathrm{MIMO}}^2 C\gamma\exp\left(2\mu_{\mathrm{MIMO}}-2\sigma_{\mathrm{MIMO}}^2\right)}{\mathrm{W}\left(4\sigma_{\mathrm{MIMO}}^2 C\gamma\exp\left(2\mu_{\mathrm{MIMO}}-2\sigma_{\mathrm{MIMO}}^2\right)\right)}\right]+2\sigma_{\mathrm{MIMO}}^2\right). \tag{5.14}
$$

Noting $\ln\left[x/\mathrm{W}(x)\right] = \mathrm{W}(x)$ [108, Eq. (8.2)] and neglecting the term $2\sigma_{\mathrm{MIMO}}^2$ for high SNR, Eq. (5.14) can be written as

$$
\mathrm{DO} \approx \lim_{\gamma\to\infty}\left(\frac{1}{4\sigma_{\mathrm{MIMO}}^2}\mathrm{W}\left(4\sigma_{\mathrm{MIMO}}^2 C\gamma\exp\left(2\mu_{\mathrm{MIMO}}-2\sigma_{\mathrm{MIMO}}^2\right)\right)\right). \tag{5.15}
$$

It can be shown that DO in Eq. (5.15) goes to infinity as expected for the LN channels. This is because of the fact that decreasing rate of BER over LN fading channels does not converge to a finite value. On the other hand, the incremental change in the decreasing rate converges. Based on this observation, we introduce the concept of incremental diversity order. Mathematically speaking, we define IDO as

$$
\mathrm{IDO} = \lim_{\gamma\to\infty}\mathrm{IDO}(\gamma) = -\lim_{\gamma\to\infty}\frac{\partial^2 \ln\overline{BER}}{\partial(\ln\gamma)^2}. \tag{5.16}
$$

In other words, while DO determines how fast the BER changes with SNR, IDO determines how fast the diversity order changes with SNR. Based on the derivative of argument in Eq. (5.15) on the preceding page, we obtain

$$\mathrm{IDO}(\gamma) \approx \frac{1}{4\sigma^2_{\mathrm{MIMO}}} \frac{\mathrm{W}\left(4\sigma^2_{\mathrm{MIMO}} C\gamma \exp\left(2\mu_{\mathrm{MIMO}} - 2\sigma^2_{\mathrm{MIMO}}\right)\right)}{\left(1 + \mathrm{W}\left(4\sigma^2_{\mathrm{MIMO}} C\gamma \exp\left(2\mu_{\mathrm{MIMO}} - 2\sigma^2_{\mathrm{MIMO}}\right)\right)\right)}. \tag{5.17}$$

For $\gamma \to \infty$, this yields

$$\mathrm{IDO} = \lim_{\gamma\to\infty} \mathrm{IDO}(\gamma) = \frac{1}{4\sigma^2_{\mathrm{MIMO}}}, \tag{5.18}$$

where σ^2_{MIMO} was earlier defined as a function of the number of laser sources, the number of photodetectors and the variance of the log-amplitude coefficient.

In the following, we consider two special cases: As a sanity check, by replacing $N_{\mathrm{S}} = 1$ and $N_{\mathrm{D}} = 1$ in Eq. (5.18), IDO of a SISO UVLC system can be obtained as $\mathrm{IDO}_{\mathrm{SISO}} \approx 1/4\sigma^2$. As another case, we assume that the fading variance is small enough (i.e. $\sigma^2 \to 0$). In this case, we can use the $\exp(x) \approx x + 1$ and simplify Eq. (5.18) as $\underset{\sigma^2\to 0}{\mathrm{IDO}} \approx N_S N_D / 4\sigma^2$. This indicates that full spatial diversity (i.e. $N_S N_D$) can be only exploited for very weak turbulence conditions.

5.2.4 Results and Discussions

In this section, we present numerical results and validate our derived closed-form BER expression in Eq. (5.10) on page 69 and IDO in Eq. (5.17). Unless otherwise stated, we assume 2×2 MIMO system, 4-PAM, noise power of $\sigma_N^2 = -100$ dBm, log amplitude variance of $\sigma^2 = 1 \times 10^{-1}$, electro-optical conversion efficiency of $\eta = 0.5$ W/A, opto-electrical responsivity of $r = 0.28$ A/W and channel attenuation term of $h = 1 \times 10^{-4}$ W.

In Figure 18 on the next page, we present Monte Carlo simulation results to validate the accuracy of derived BER expression in Eq. (5.10) on page 69. Since average SNR of MIMO system with EGC increases with increasing number of sources/detectors, we define $\gamma_c = P_{\mathrm{te}} \eta^2 r^2 h^2 / \sigma_N^2$ as a common SNR for a fair comparison. Our results show that there is some discrepancy in lower SNR region, but as SNR goes higher, the derived expression coincides with the simulation results. In particular, almost an exact match is observed for BER $< 1 \times 10^{-2}$. It can also be observed that the required SNR for SISO link in order to achieve a target BER of 10^{-6} is γ_c = 28.26 dB. This decreases to γ_c = 20.97 dB and 18.13 dB, respectively for 2×2 and 3×3 MIMO systems. These indicate performance improvements of 7.29 dB and 10.13 dB over SISO counterpart.

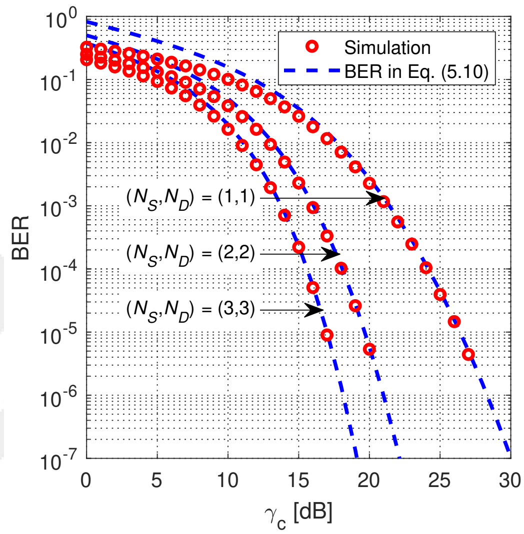

Figure 18: BER over LN fading channels.

As observed from Figure 18, the slope of BER curves versus SNR over LN fading does not converge to a fixed value. To better demonstrate this, we plot $\mathrm{DO}(\gamma) = -\partial \ln \overline{BER} / \partial \ln \gamma$ in Figure 19(a) on the following page along with the derived expression in Eq. (5.15) on page 70. Our derived expression provides excellent agreement with the exact DO confirming the accuracy of our derivation. It should be noted that we assume asymptotically high SNR range up to 300 dB. While these are obviously not practical values, it is essential to consider such a range for the demonstration of convergence. It is also observed from Figure 19(a) on the following page that the slope of BER continuously increases and can be represented by a line at high SNR. This indicates that the slope of DO must converge. This convergence is demonstrated in Fig. 19(b) on the next page where $\mathrm{IDO}(\gamma) = -\partial^2 \ln \overline{BER} / \partial (\ln \gamma)^2$ is plotted along with the derived IDO expression in Eq. (5.17) on the preceding page.

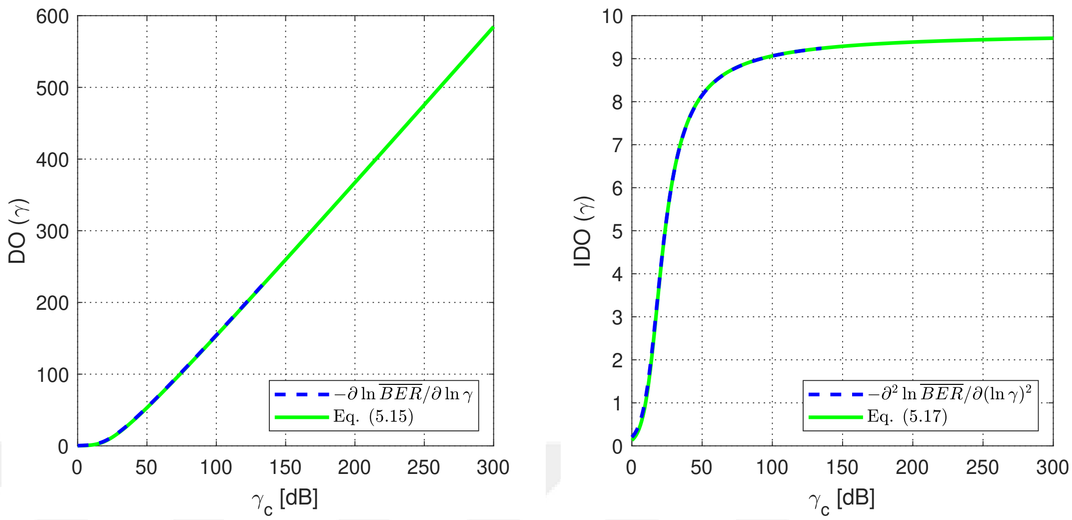

(a) (b)

Figure 19: Diversity analysis of BER over LN fading: (a) DO and (b) IDO.

In Figure 20 on the next page, we investigate the effect of number of transmitters and receivers on diversity gains. Specifically, we assume a log-amplitude variance of $\sigma^2 = 1 \times 10^{-1}$ and plot IDO(γ) based on Eq. (5.17) on page 71 for MIMO systems. SISO case (i.e. $N_S = 1$ and $N_D = 1$) is considered as a benchmark. The variance of equivalent MIMO channels are obtained as $\sigma^2_{\text{MIMO}} = 2.6 \times 10^{-2}$, 1.16×10^{-2} and 6.55×10^{-3} respectively for 2×2, 3×3 and 4×4 MIMO systems. It can be checked from Figure 20 on the next page that corresponding IDO values are obtained as 1.73, 6.36, 13.61 and 23.21 at γ_c = 30 dB, respectively. These are obviously much smaller than those predicted by Eq. (5.18) on page 71 which can be observed only for sufficiently high SNR values. For demonstrating the convergence, inset figure is used where sufficiently large values of SNR are assumed. The diversity gains predicted by Eq. (5.18) on page 71 are indicated by dashed lines. It is observed that IDO(γ) converges to IDO = $1/4\sigma^2_{\text{MIMO}}$ = 2.50, 9.63, 21.52 and 38.16 for 1×1, 2×2, 3×3 and 4×4 MIMO systems, respectively, confirming the accuracy of Eq. (5.18) on page 71. If we normalize these with the IDO value achieved for SISO case, we have 3.85<4, 8.61<9 and 15.26<16 indicating that full spatial diversity cannot be extracted for log-amplitude variance of $\sigma^2 = 1 \times 10^{-1}$.

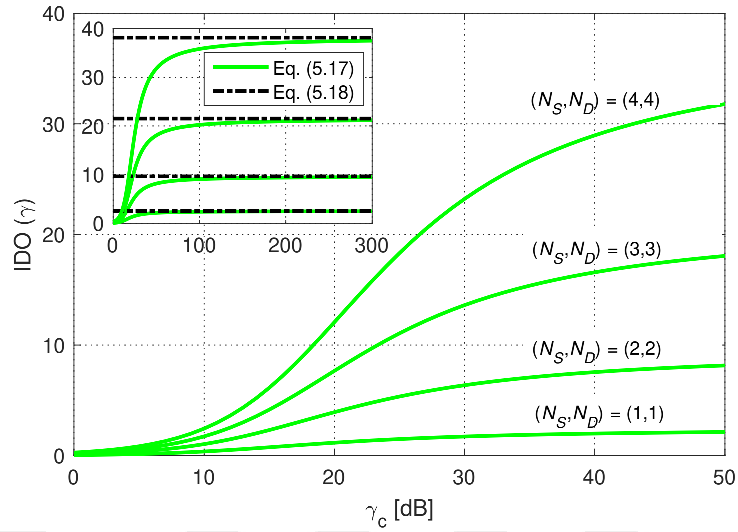

Figure 20: Effect of number of transmitters/receivers on IDO (LN variance of $\sigma^2 = 1 \times 10^{-1}$ is assumed).

In Figure 21 on the next page, we investigate the effect of different turbulence strengths on diversity gains. Specifically, we consider a 2×2 MIMO system and plot IDO(γ) based on Eq. (5.17) on page 71 for log-amplitude variances of $\sigma^2 = 1 \times 10^{-1}$, 5×10^{-2} and 2.5×10^{-2}. The corresponding variances of equivalent MIMO channels are obtained as $\sigma^2_{\mathrm{MIMO}} = 2.6 \times 10^{-2}$, 1.27×10^{-2} and 6.31×10^{-3}, respectively. Similar to Figure 20, full spatial diversity can not be attained within practical SNR range. For sufficiently large values of SNR, IDO values are obtained as 9.63, 19.63 and 39.63 for $\sigma^2 = 1 \times 10^{-1}$, 5×10^{-2} and 2.5×10^{-2}, respectively, as predicted by Eq. (5.18) on page 71. Normalization of IDO values yields 3.85, 3.93 and 3.96, respectively, for $\sigma^2 = 1 \times 10^{-1}$, 5×10^{-2} and 2.5×10^{-2} indicating that full spatial diversity (i.e. $N_S N_D = 4$) can be only obtained when fading variance is sufficiently small.

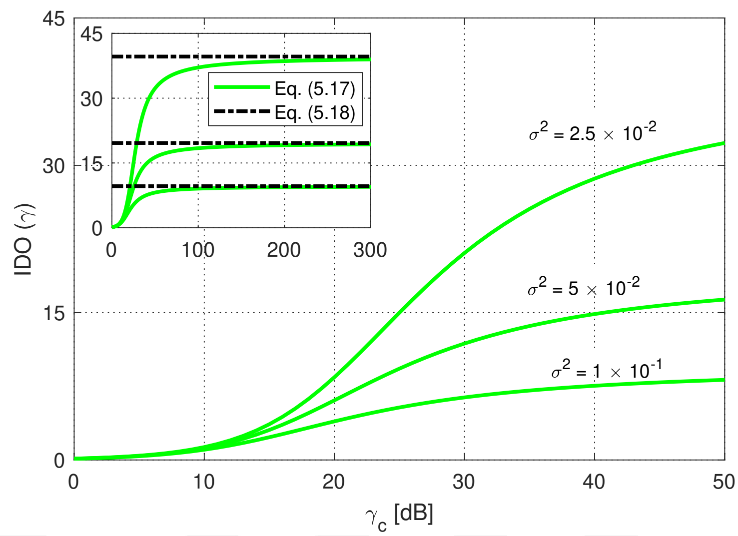

Figure 21: Effect of different variance values on IDO (2×2 MIMO system is assumed).

5.3 Generalized Transmit Laser Selection

TLS has been proposed as an efficient fading-mitigation technique over turbulence channels. In TLS, the transmitter is equipped with a number of laser sources and the best laser source is selected for transmission. In practice, feedback error or outdated selection due to temporal changes in the channel may result in selecting another source rather than the best one. In this section, we consider a UVLC system with GTLS where the n^{th} best laser is selected among the available N lasers. Under the assumption of LN turbulence channels in addition to pointing errors, we derive a closed-form expression for asymptotic bit error rate. We use our derived closed-form expression to determine the diversity gains. We finally present simulation results to corroborate our analytical findings.

5.3.1 System Model

As illustrated in Figure 22 on the next page, we consider a diver-to-diver UVLC system with N laser sources and a single photo-detector. The receiver estimates the fading channel coefficients (that determines the instantaneous SNR values) and chooses the index of the "best" laser source with the highest channel coefficient. Through a feedback channel, it sends the index to the transmitter and the transmitter accordingly switches to the "best" source. In the ideal case, the best source is the one that gives the highest value of instantaneous SNR. However, in practice, there might be different sources of errors which might result in the selection of second-best or worse.

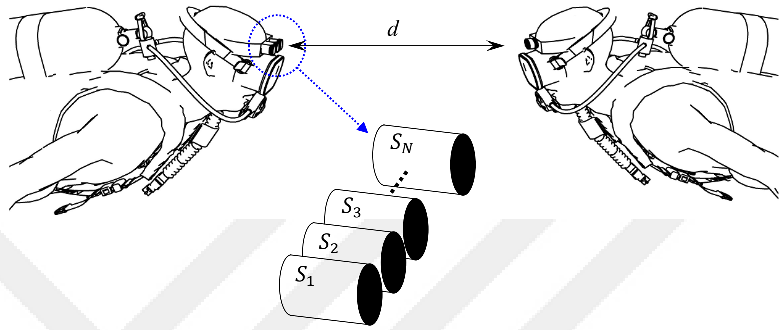

(a)

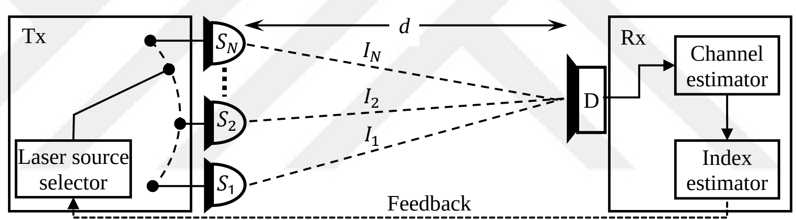

(b)

Figure 22: GTLS system block diagram.

Let $I_{(1)}$, $I_{(2)}$, $\ldots$,$I_{(n)}$,$\ldots$, $I_{(N)}$ be i.i.d LN fading coefficients arranged in decreasing order. $I_{(n)}$ represents the n^{th} largest fading coefficient associated with the n^{th} best laser source. Let s denote the transmitted unipolar M-ary pulse amplitude modulation (M-PAM) symbol. The received signal intensity can be written as

$$y = \sqrt{P_{\text{te}}}\eta r h I_{(n)} I_P s + w, \tag{5.19}$$

where P_{te} is the average electrical transmit power, η is the electro-optical conversion efficiency of the laser diode, r is the opto-electrical responsivity of the photo-detector, h is the channel loss term[1] and $w \sim \mathcal{N}\left(0, \sigma_n^2\right)$ is the AWGN term with zero mean and variance of

[1]The separation between sources is much smaller than the link distance. Therefore, the channel loss can be considered identical for all channels.

σ_n^2. Based on the order statistics [130, Eq. (2.2.2)], we can express the PDF of $I_{(n)}$ as

$$\begin{aligned} f_{I_{(n)}}\left(I_{(n)}\right) =& \frac{N!\,2^{1-N} I_{(n)}^{-1}}{(N-n)!\,(n-1)!\sqrt{2\pi\sigma^2}} \exp\left(-\frac{\left(\ln\left(I_{(n)}\right)-\mu\right)^2}{2\sigma^2}\right) \\ &\times \left(\operatorname{erfc}\left(\frac{\mu-\ln\left(I_{(n)}\right)}{\sqrt{2}\sigma}\right)\right)^{N-n} \left(\operatorname{erfc}\left(\frac{\ln\left(I_{(n)}\right)-\mu}{\sqrt{2}\sigma}\right)\right)^{n-1}. \end{aligned} \tag{5.20}$$

In Eq. (5.20), $\mu = 2\mu_x$ and $\sigma^2 = 4\sigma_x^2$. Here, μ_x and σ_x^2 denote, respectively, the mean and variance of the log amplitude coefficient $X_{(n)} = 0.5\ln\left(I_{(n)}\right)$. In order to make sure that fading coefficient does not change the average power, fading coefficient is normalized such that $\mathrm{E}\left[I_{(n)}\right] = 1$ (i.e., $\sigma_x^2 = -\mu_x$).

In Eq. (5.19) on the previous page, I_P represents the fading coefficient induced by pointing errors. Under the assumption that both displacements along the elevation and horizontal axes are modeled as i.i.d. Gaussian variables with zero mean and variance of σ_s^2, the PDF of I_P can be expressed as [131]

$$f_{I_p}\left(I_p\right) = \frac{\xi^2}{A_0^{\xi^2}} I_p^{\xi^2-1}, \quad 0 \le I_p \le A_0 \tag{5.21}$$

where A_0 is the fraction of the collected power at zero displacement and ξ defines the ratio between the equivalent beam radius and the pointing error displacement standard deviation (i.e., σ_s).

5.3.2 Derivation of BER

For M-PAM, the average BER associated with the selected n^{th} best source can be calculated as

$$BER_n = \int_0^\infty \int_0^{A_0} F \operatorname{erfc}\left(\sqrt{C\gamma_{(n)}}\right) f_{I_p}\left(I_p\right) f_{I_{(n)}}\left(I_{(n)}\right) dI_P\, dI_{(n)}, \tag{5.22}$$

where $\operatorname{erfc}(\cdot)$ is the complementary error function, $F = (M-1)/(M\log_2(M))$ and $C = 3/(2(M-1)(2M-1))$ [103, Eq. (3.10)]. In Eq. (5.22), $\gamma_{(n)} = \bar{\gamma} I_{(n)}^2 I_P^2$ is the instantaneous received SNR where $\bar{\gamma} = P_{\mathrm{te}}\eta^2 r^2 h^2/\sigma_n^2$ denotes the average received SNR. By changing the integration variable of $x=\left(\mu-\ln\left(I_{(n)}\right)\right)/\sqrt{2}\sigma$, we can rewrite Eq. (5.22) on the previous page as

$$\begin{aligned} BER_n = & \frac{N!2^{1-N}F\xi^2}{A_0^{\xi^2}(N-n)!\,(n-1)!\sqrt{\pi}} \\ & \times \int_{-\infty}^{\infty} \exp\left(-x^2\right)\left(\operatorname{erfc}(x)\right)^{N-n}\left(\operatorname{erfc}(-x)\right)^{n-1} \\ & \quad \times \int_0^{A_\circ} I_p^{\xi^2-1}\operatorname{erfc}\left(\sqrt{C\bar{\gamma}}\exp(\mu)\exp\left(-\sqrt{2}\sigma x\right)I_P\right)dI_p dx\cdot \end{aligned} \tag{5.23}$$

The second integration in Eq. (5.23) can be solved in terms of lower incomplete Gamma function by utilizing [132, section 4.1, Eq. (17)]. Assuming high SNR (i.e., $\bar{\gamma}\to\infty$), the lower incomplete Gamma function converges to Gamma function and we can write Eq. (5.23) in the form of

$$BER_{\text{Asym},n} \approx BER_{T_{\text{Asym}},n} + BER_{P_{\text{Asym}},n}, \tag{5.24}$$

where $BER_{T_{\text{Asym}},n}$ and $BER_{P_{\text{Asym}},n}$ are given respectively as

$$\begin{aligned} BER_{T_{\text{Asym}},n} = & \frac{N!2^{1-N}F}{(N-n)!\,(n-1)!\sqrt{\pi}}\int_{-\infty}^{\infty}\exp(-x^2)\operatorname{erfc}\left(\sqrt{C\bar{\gamma}}\exp(\mu)\exp\left(-\sqrt{2}\sigma x\right)A_\circ\right) \\ & \times\left(\operatorname{erfc}(x)\right)^{N-n}\left(\operatorname{erfc}(-x)\right)^{n-1}dx\cdot \end{aligned} \tag{5.25}$$

$$\begin{aligned} BER_{P_{\text{Asym}},n} = & \frac{N!2^{1-N}F\,\Gamma\left(\left(\xi^2+1\right)/2\right)}{\left(A_\circ\sqrt{C\bar{\gamma}}\exp(\mu)\right)^{\xi^2}(N-n)!\,(n-1)!\pi} \\ & \times\int_{-\infty}^{\infty}\exp\left(-x^2\right)\left(\operatorname{erfc}(x)\right)^{N-n}\left(\operatorname{erfc}(-x)\right)^{n-1}\exp\left(\xi^2\sqrt{2}\sigma x\right)dx\cdot \end{aligned} \tag{5.26}$$

For solving the integration in Eq. (5.25), we replace the first $\operatorname{erfc}(\cdot)$ term by $\operatorname{erfc}(x)\approx(1/6)\exp\left(-x^2\right)+(1/2)\exp\left(-4x^2/3\right)$ [73]. For the second and third $\operatorname{erfc}(\cdot)$ terms in Eq. (5.25), it can be readily checked that $\int_{x_0}^{\infty}f(x)\,d_x \gg \int_{-\infty}^{x_0}f(x)\,d_x,\ \ x_0\gg 0$ for high SNR (i.e., $\bar{\gamma}\to\infty$). Therefore, second $\operatorname{erfc}(\cdot)$ term can be replaced by $\operatorname{erfc}(x)\lessapprox\left(x\sqrt{\pi}\right)^{-1}\exp\left(-x^2\right),\ \ x\gg 0$ using Mills' ratio inequality [129, Eq. (4.2)]. It can be further noted that $\operatorname{erfc}(-x)\approx 2,\ \ x\gg 0$. Therefore, the third $\operatorname{erfc}(\cdot)$ term can be simply replaced by 2. Replacing these within Eq. (5.25) on the preceding page, we have

$$
\begin{aligned}
BER_{T_{\mathrm{Asym}},n} \approx & \frac{F}{3\pi^{(N-n+1)/2}} \frac{N!2^{-(N-n+1)}}{(N-n)!\,(n-1)!} \int_{-\infty}^{\infty} x^{n-N} \exp\left(\bar{\gamma}\phi\left(x\right)\right) dx \\
& + \frac{F}{\pi^{(N-n+1)/2}} \frac{N!2^{-(N-n+1)}}{(N-n)!\,(n-1)!} \int_{-\infty}^{\infty} x^{n-N} \exp\left(\bar{\gamma}\psi\left(x\right)\right) dx \cdot
\end{aligned}
\tag{5.27}
$$

In Eq. (5.27), $\phi\left(x\right) = -CA_{\circ}^{2}\exp\left(2\mu - 2\sqrt{2}\sigma x\right) - \left(\left(N-n+1\right)/\bar{\gamma}\right)x^{2}$ and $\psi\left(x\right) = -\left(4/3\right)CA_{\circ}^{2}\exp\left(2\mu - 2\sqrt{2}\sigma x\right) - \left(\left(N-n+1\right)/\bar{\gamma}\right)x^{2}$. Utilizing the Laplace method of integration, the integration in Eq. (5.27) can be solved as

$$
\begin{aligned}
BER_{T_{\mathrm{Asym}},n} \approx & \frac{F}{3\pi^{(N-n+1)/2}} \frac{N!2^{-N+n-1}}{(N-n)!\,(n-1)!} \left(\frac{2\pi}{\bar{\gamma}\left|\phi''\left(x_{\phi}\right)\right|}\right)^{1/2} x_{\phi}^{n-N} \exp\left(\bar{\gamma}\phi\left(x_{\phi}\right)\right) \\
& + \frac{F}{\pi^{(N-n+1)/2}} \frac{N!2^{-N+n-1}}{(N-n)!\,(n-1)!} \left(\frac{2\pi}{\bar{\gamma}\left|\psi''\left(x_{\psi}\right)\right|}\right)^{1/2} x_{\psi}^{n-N} \exp\left(\bar{\gamma}\psi\left(x_{\psi}\right)\right) \cdot
\end{aligned}
\tag{5.28}
$$

In Eq. (5.28), $\phi''\left(x\right) = -8\sigma^{2}CA_{\circ}^{2}\exp\left(2\mu - 2\sqrt{2}\sigma x\right) - \left(2\left(N-n+1\right)/\bar{\gamma}\right)$ and $\psi''\left(x\right) = -\left(32/3\right)\sigma^{2}CA_{\circ}^{2}\exp\left(2\mu - 2\sqrt{2}\sigma x\right) - \left(2\left(N-n+1\right)/\bar{\gamma}\right)$. x_{ϕ} and x_{ψ} are, respectively, the solutions of $\phi'\left(x\right) = 0$ and $\psi'\left(x\right) = 0$. It can be shown that the solution of $\phi'\left(x\right) = 0$ is given by $x_{\phi} = \left(1/2\sqrt{2}\sigma\right)\mathrm{W}\left(4\bar{\gamma}\sigma^{2}CA_{\circ}^{2}\exp\left(2\mu\right)/\left(N-n+1\right)\right)$ and the solution of $\psi'\left(x\right) = 0$ is given by $x_{\psi} = \left(1/2\sqrt{2}\sigma\right)\mathrm{W}\left(16\bar{\gamma}\sigma^{2}CA_{\circ}^{2}\exp\left(2\mu\right)/\left(3\left(N-n+1\right)\right)\right)$ with $\mathrm{W}\left(\cdot\right)$ denoting the Lambert-W function.

For solving the integration in Eq. (5.26) on the preceding page, first observe that it is in the form of $\int_{-\infty}^{\infty} g\left(x\right) f\left(x\right) d_{x}$, where $g\left(x\right) = \exp\left(-x^{2}\right)$ is absolutely integrable function (i.e., the integration of its absolute value over the whole domain is finite [133, Section 2.1]) and $f\left(x\right) = \left(\mathrm{erfc}\left(x\right)\right)^{N-n}\left(\mathrm{erfc}\left(-x\right)\right)^{n-1}\exp\left(\xi^{2}\sqrt{2}\sigma x\right)$ is a smooth-continuous function. Using Gauss-Hermite rule [134, Eq. (25.4.46)], we can write Eq. (5.26) on the previous page as a truncated sum

$$
\begin{aligned}
BER_{P_{\mathrm{Asym}},n} = & \frac{N!2^{1-N}F\,\Gamma\left(\left(\xi^{2}+1\right)/2\right)}{\left(A_{\circ}\sqrt{C}\exp\left(\mu\right)\right)^{\xi^{2}}\left(N-n\right)!\left(n-1\right)!\pi} \\
& \times \left(\sum_{i=1}^{l} w_{i,l}\left(\mathrm{erfc}\left(x_{i,l}\right)\right)^{N-n}\left(\mathrm{erfc}\left(-x_{i,l}\right)\right)^{n-1}\exp\left(\xi^{2}\sqrt{2}\sigma x_{i,l}\right)\right)\bar{\gamma}^{-\xi^{2}/2},
\end{aligned}
\tag{5.29}
$$

where $\Gamma(\cdot)$ is Gamma function. In Eq. (5.29) on the preceding page, $x_{i,l},\ i=1,2,\cdots,l$ is the set of roots defined by $H_l(x)=0$ with $H_l(x)$ denoting the physicists Hermite polynomial. $w_{i,l},\ i=1,2,\cdots,l$ is the corresponding weight to $x_{i,l}$.

Replacing Eq. (5.28) on the previous page and Eq. (5.29) on the preceding page in Eq. (5.24) on page 78, the final form of asymptotic BER expression can be written as

$$\begin{aligned}
BER_{\text{Asym},n} =& \frac{F}{3\pi^{(N-n+1)/2}}\frac{N!2^{-N+n-1}}{(N-n)!\,(n-1)!}\left(\frac{2\pi}{\bar{\gamma}\left|\phi''(x_\phi)\right|}\right)^{1/2} x_\phi^{n-N}\exp\left(\bar{\gamma}\phi\left(x_\phi\right)\right)\\
&+\frac{F}{\pi^{(N-n+1)/2}}\frac{N!2^{-N+n-1}}{(N-n)!\,(n-1)!}\left(\frac{2\pi}{\bar{\gamma}\left|\psi''(x_\psi)\right|}\right)^{1/2} x_\psi^{n-N}\exp\left(\bar{\gamma}\psi\left(x_\psi\right)\right)\\
&+\frac{N!2^{1-N}F\,\Gamma\left(\left(\xi^2+1\right)/2\right)}{\left(A_\circ\sqrt{C}\exp(\mu)\right)^{\xi^2}(N-n)!\,(n-1)!\,\pi}\\
&\times\left(\sum_{i=1}^{l} w_{i,l}\left(\operatorname{erfc}\left(x_{i,l}\right)\right)^{N-n}\left(\operatorname{erfc}\left(-x_{i,l}\right)\right)^{n-1}\exp\left(\xi^2\sqrt{2}\sigma x_{i,l}\right)\right)\bar{\gamma}^{-\xi^2/2}.
\end{aligned} \tag{5.30}$$

In the following, as a sanity check, we consider two special cases.

Special Case I: In the case of no pointing error, i.e., $A_0=1$ and $\xi\to\infty$, the third term in Eq. (5.30) becomes zero and BER in Eq. (5.30) reduces to Eq. (5.28) on the preceding page.

Special Case II: With the selection of best source (i.e., $n=1$), asymptotic BER expression in Eq. (5.28) on the previous page reduces to [135, Eq. (13)] which was earlier reported in the literature for TLS.

5.3.3 Diversity Gain Analysis

DO is typically defined as the negative slope of asymptotic BER versus SNR on a log-log scale. Mathematically speaking, we have

$$\mathrm{DO}=\lim_{\bar{\gamma}\to\infty}\mathrm{DO}(\bar{\gamma})=\lim_{\bar{\gamma}\to\infty}-\frac{\partial\ln BER_n}{\partial\ln\bar{\gamma}}. \tag{5.31}$$

Note that the first two terms of the derived BER in Eq. (5.30) are exponentially decreasing with SNR. Therefore, the third term will be much larger than the other two terms for $\bar{\gamma}\to\infty$.

After neglecting the first two terms and taking logarithm of the remaining term, we have

$$\ln BER_{\mathrm{Asym},n} = \ln\left(\begin{array}{l}\dfrac{N!2^{1-N}F\Gamma\left(\left(\xi^2+1\right)/2\right)}{\left(A_\circ\sqrt{C}\exp\left(\mu\right)\right)^{\xi^2}(N-n)!\,(n-1)!\pi} \\ \times\sum\limits_{i=1}^{l} w_{i,l}\left(\operatorname{erfc}\left(x_{i,l}\right)\right)^{N-n}\left(\operatorname{erfc}\left(-x_{i,l}\right)\right)^{n-1}\exp\left(\xi^2\sqrt{2}\sigma x_{i,l}\right)\end{array}\right) - \frac{\xi^2}{2}\ln\left(\bar{\gamma}\right). \tag{5.32}$$

Replacing Eq. (5.32) within Eq. (5.31) on the preceding page and taking the derivative, it can be readily verified that the DO will be equal to $\xi^2/2$. This indicates that diversity gain is dominated by pointing error, if present, rather than turbulence strength.

Pointing errors might be compensated with proper tracking techniques or its effect remains at a negligible level for short distances. In such cases, we need to consider only the effect of fading. It is important to note that the decreasing rate of error probability over LN fading channels does not converge to a finite value. Since the conventional definition of diversity order can not be used, IDO was recently proposed in [110] as an alternative performance metric. It is defined as the incremental change in the decreasing rate of BER in log-log scale. Mathematically speaking, it is given by

$$\mathrm{IDO} = \lim_{\bar{\gamma}\to\infty}\ \mathrm{IDO}\left(\bar{\gamma}\right) = \lim_{\bar{\gamma}\to\infty} -\frac{\partial^2 \ln BER_n}{\partial\left(\ln\bar{\gamma}\right)^2}. \tag{5.33}$$

For GTLS system under consideration, we derive the IDO for the n^{th} best source in the following. Replacing Eq. (5.28) on page 79 in Eq. (5.33) and noting that $\phi\left(x\right) > \psi\left(x\right)\ \forall x$, we have

$$\begin{aligned}\frac{\partial\ln BER_n}{\partial\ln\bar{\gamma}} \approx & -\frac{2\bar{\gamma}\sigma^2 C\exp\left(2\mu-2\sqrt{2}\sigma x_\phi\right)}{4\bar{\gamma}\sigma^2 C\exp\left(2\mu-2\sqrt{2}\sigma x_\phi\right)+(N-n+1)}\left[1-2\sqrt{2}\sigma x'_\phi\right] \\ & -C\bar{\gamma}\exp\left(2\mu-2\sqrt{2}\sigma x_\phi\right)\left[1-2\sqrt{2}\sigma x'_\phi\right] \\ & +(n-N)\frac{x'_\phi}{x_\phi}-2\left(N-n+1\right)x_\phi x'_\phi.\end{aligned} \tag{5.34}$$

In Eq. (5.34) on the previous page, $x'_\phi = \partial x_\phi / \partial \ln(\bar{\gamma})$. Utilizing the derivative of Lambert-W function, we can obtain x'_ϕ as

$$x'_\phi = \frac{1}{2\sqrt{2}\sigma} \frac{\mathrm{W}\left(\frac{4\bar{\gamma}\sigma^2 C\exp(2\mu)}{(N-n+1)}\right)}{\left(1+\mathrm{W}\left(\frac{4\bar{\gamma}\sigma^2 C\exp(2\mu)}{(N-n+1)}\right)\right)}. \tag{5.35}$$

Replacing Eq. (5.35) in Eq. (5.34) on the previous page, it can be readily confirmed that the first three terms in the resulting expression approach zero. Utilizing further the fact that $\mathrm{W}\left(4\bar{\gamma}\sigma^2 C\exp(2\mu)/(N-n+1)\right) \gg 1$ for high SNR, we obtain

$$\frac{\partial \ln BER_n}{\partial \ln \bar{\gamma}} \underset{\bar{\gamma}\to\infty}{\approx} -\frac{(N-n+1)}{4\sigma^2} \mathrm{W}\left(\frac{4\bar{\gamma}\sigma^2 C\exp(2\mu)}{(N-n+1)}\right). \tag{5.36}$$

The derivative of Eq. (5.35) yields IDO as

$$\begin{aligned}\mathrm{IDO} &\approx \lim_{\bar{\gamma}\to\infty} \frac{(N-n+1)}{4\sigma^2} \frac{\mathrm{W}\left(\frac{4\bar{\gamma}\sigma^2 C\exp(2\mu)}{(N-n+1)}\right)}{\left[1+\mathrm{W}\left(\frac{4\bar{\gamma}\sigma^2 C\exp(2\mu)}{(N-n+1)}\right)\right]} \\ &= \frac{(N-n+1)}{4\sigma^2}.\end{aligned} \tag{5.37}$$

Our result yields that IDO is mainly determined by two parameters. First, it is inversely proportional to log-amplitude variance. Second, it is proportional to $(N-n+1)$; this indicates that IDO is dominated by the source with the $(N-n+1)^{\text{th}}$ smallest fading coefficient.

5.3.4 Results and Discussions

In this section, we present numerical results and validate our derived asymptotic closed-form BER expression in Eq. (5.30) on page 80. We further show the convergence of incremental change in diversity order to the predicted value by Eq. (5.37). Unless stated otherwise, we assume 4-PAM, log amplitude variance of $\sigma^2 = 5\times10^{-1}$, noise variance of $\sigma_n^2 = -100$ dBm, electro-optical conversion efficiency of $\eta = 0.5$ W/A, opto-electrical photo-detector responsivity of $r = 0.28$ A/W and channel attenuation term of $h = -40$ dB. The pointing error parameters are set as $A_0 = 1$ and $\xi^2 = 3.5$.

In Figure 23, we consider GTLS system with $N = 5$ laser sources. Exact BER is obtained based on the numerical integration of Eq. (5.22) on page 77 and, as expected, provides a perfect match with Monte Carlo simulation results. The asymptotical BER is plotted based on the derived expression in Eq. (5.30) on page 80. This expression consists of three terms. The first two are related to LN fading while the last term is related to pointing error. It can be readily checked that the third term dominates the overall expression. From Figure 23, it can be observed that there is some deviation between the derived and exact expressions in low SNR values. This deviation comes from the replacing of lower incomplete Gamma function by Gamma function in the derivation of this third term, which is only valid for high SNR. As SNR values get higher, the derived asymptotical expression converges to the exact one regardless of the value of n.

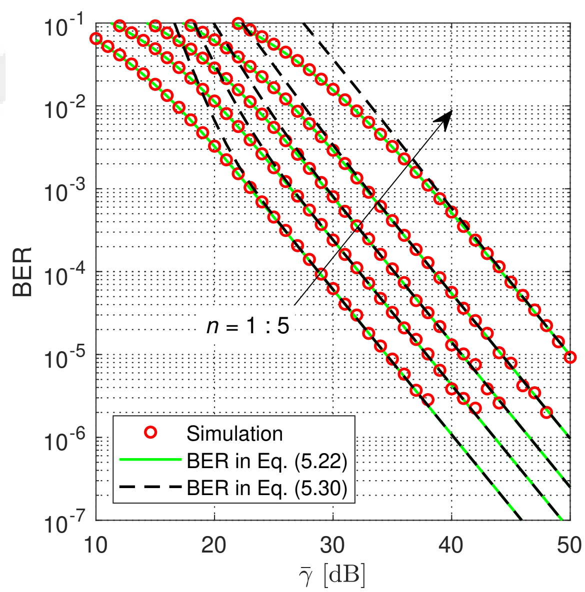

Figure 23: Comparison of derived BER expression with exact expression and simulations ($N = 5$ is assumed)

Our results further quantify the performance deterioration associated with choosing the n^{th} best source. It is observed from Figure 23 that SNR of $\bar{\gamma} = 34.48$ dB is required in order to achieve a targeted BER of 10^{-5} for the ideal case (i.e., TLS system) where the best source is always selected. The required SNR climbs to 37.89 dB indicating an extra SNR of 3.41 if the second best is selected due to incorrect selection of transmitter index. Extra SNRs for the selection of the third, fourth and fifth best are given respectively by 6.37 dB, 9.73 dB and 15.46 dB.

In Figure 24, we investigate the effect of the number of sources on the BER performance of GTLS. We consider $N = 2$, 3, 4 and 5 and assume that the second best is selected for all cases. Similar to Figure 23 on the previous page, the derived BER expression converges to the exact one regardless of N value and provides a good match to simulation results except low SNR values. It can be also checked from Figure 24 that SNR of $\bar{\gamma} = 47.87$ dB is required for $N = 2$ in order to achieve a targeted BER of 10^{-5}. This decreases to 42.10 dB, 39.51 dB and 37.89 dB, respectively, for $N = 3$, 4 and 5 sources indicating performance improvements of 5.77 dB, 8.36 dB and 9.98 dB. As expected, the increase in the number of sources improves the performance. However, the performance improvement gets smaller for higher number of sources.

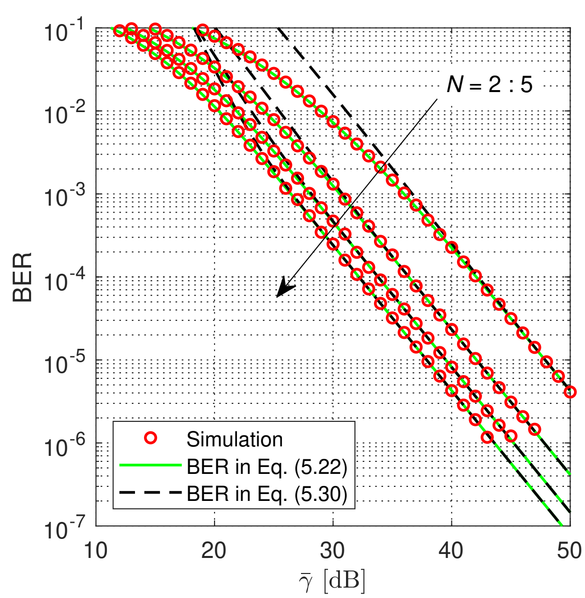

Figure 24: Effect of the number of sources on the BER performance. We consider N= 2, 3, 4 and 5 laser sources and assume that the second best (i.e., $n = 2$) is selected for all cases. .

In Figures 25(a) and 25(b), we analyze the diversity orders of GTLS with and without pointing errors, respectively. It is observed from Figure 25(a)that the decreasing rate of BER for $n = 1, 2, \cdots, 5$ is controlled by pointing error and converges to a fixed value given by $\xi^2/2 \ = 1.75$. Regardless of which source was selected, the same asymptotic diversity order is obtained. However, if the best source is selected, the gain becomes higher at finite SNR values. For the case of no pointing error, it is observed from Figure 25(b) that diversity order depends on the number of sources and the selected source index. As predicted by Eq. (5.37) on page 82, we obtain $(N-n+1)/4\sigma^2 \ = 2.5$, 2.0, 1.5, 1.0 and 0.5, respectively for =1, 2, 3, 4 and 5. It should be noted that we assume an SNR range up to 300 dB in this figure for the sake of demonstrating the convergence. This is due to the fact that the convergence to full diversity over LN channels is very slow. This also indicates that full diversity can not be extracted within practical SNR range.

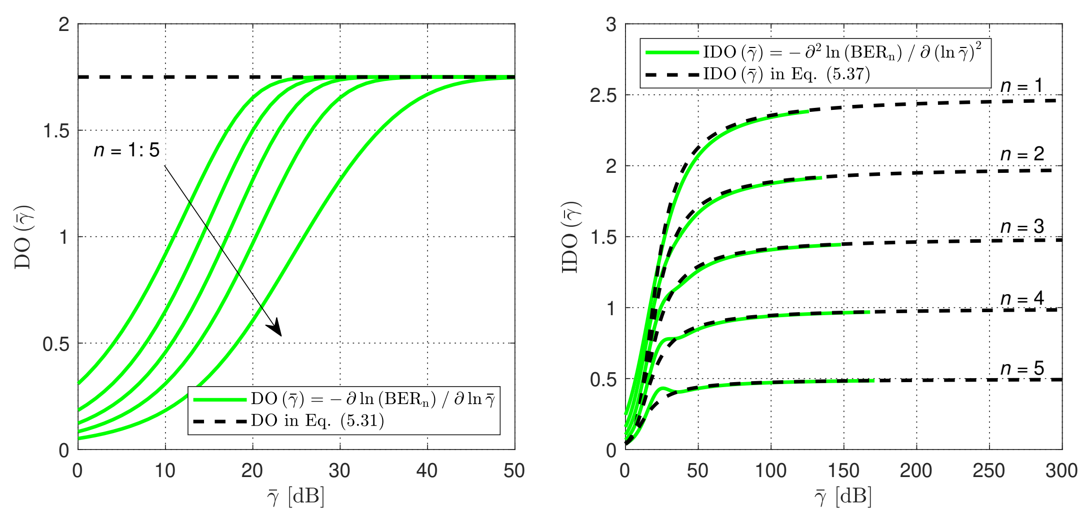

(a) (b)

Figure 25: Diversity order analysis of GTLS ($N = 5$ is assumed): (a) with pointing error (b) without pointing error.

CHAPTER VI

MULTIPLE ACCESS IN UVLC SYSTEMS

6.1 Introduction

The previous chapters of this dissertation are limited to a single-user case. Yet, practical implementation of USN requires the design of multiple access systems for supporting several sensor nodes. Motivated by this, several multiple access schemes have been proposed in the open literature for supporting multiple nodes connectivity, which can be divided into orthogonal and non-orthogonal multiple access schemes.

In orthogonal multiple access schemes, nodes are allocated orthogonal resources either in frequency or time domain. For example, in OFDMA, different nodes are assigned different frequency sub-carriers. In NOMA schemes, multiple users simultaneously share the entire available frequency and time resources, with a controlled interference threshold, leading to low latency and significant gains in spectral efficiency [136].

The rest of this chapter is organized as follow. In Section 6.2, we introduce the use of adaptive OFDMA in the context of UVLC systems. The adaptive system is formulated such that the overall data rate is maximized subject to two constraints: identical user's data rate and BER of each user not exceeding a pre-defined maximum BER. In Section 6.3, we consider NOMA in the context of USN and investigate the achievable NOMA capacity.

6.2 OFDMA

In this section, we consider the downlink of an USN where the communication between the central command unit and sensor nodes takes place through VLC. The system builds upon DCO-OFDMA where subsets of subcarriers are assigned to different nodes. We propose a joint subcarrier allocation and bit loading algorithm in an effort to achieve an identical data rate for each node in the USN while satisfying a targeted BER. We further present the Monte Carlo simulation results to demonstrate the performance of the proposed adaptive algorithm.

6.2.1 System Model

We envision a USN where a central command unit (that might, for example, take the form of an autonomous underwater vehicle) communicates with several sensor nodes. We employ adaptive DCO-OFDMA for downlink transmission (see Figure 26). We assume L sensor nodes and N subcarriers ($N \gg L$). For DCO-OFDM, only $N/2 - 1$ subcarriers are used for data transmission.

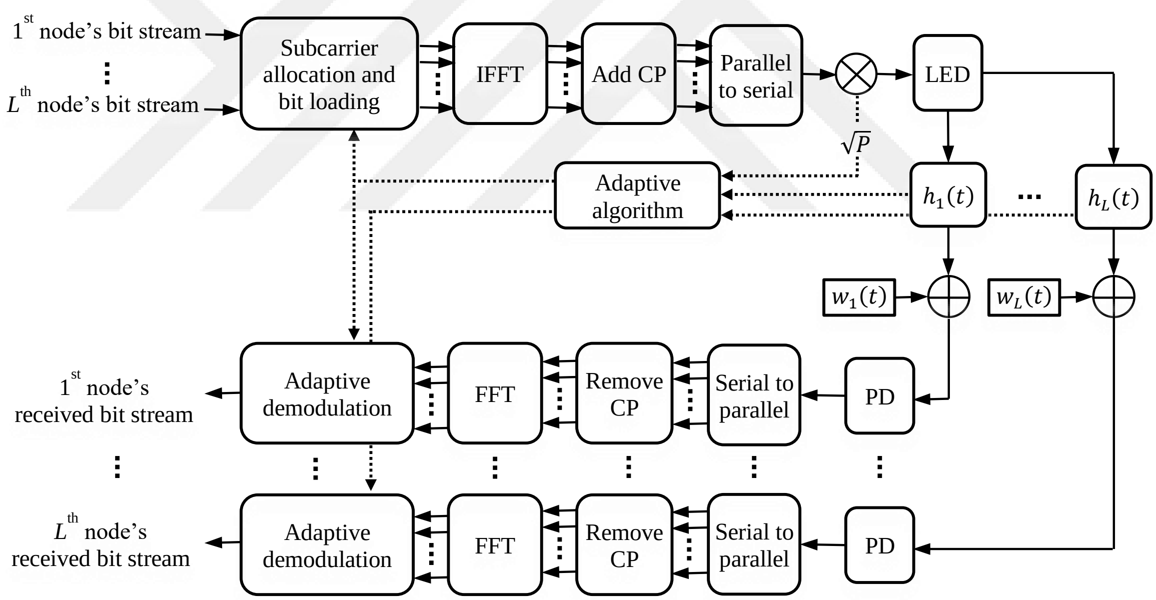

Figure 26: Block diagram of adaptive OFDMA system.

Let S_{K_l} and N_l denote, respectively, the set of subcarriers assigned to the l^{th} node and the size of S_{K_l} (i.e., the number of allocated subcarriers to the l^{th} node). We assume $\sum_{l=1}^{L} N_l \leq N$ and $S_{K_j} \cap S_{K_l} \in \varnothing$, $j \neq l$ with $\varnothing$ denoting the empty set. The selections of subcarriers for each node (i.e., how they will be allocated among nodes) and the modulation size for each subcarrier are decided by the adaptive algorithm (see Section 6.2.2).

Let u_i , $i = 1, \cdots, N/2 - 1$, PSK/QAM symbols. Hermitian symmetry is performed for ensuring that the output of IDFT is real. Therefore, frequency-domain OFDM symbol which carries data for L nodes is written as

$$\mathbf{X} = \begin{bmatrix} 0 & u_1 & \cdots & u_{N/2-1} & 0 & u^*_{N/2-1} & \cdots & u^*_1 \end{bmatrix}^T. \tag{6.1}$$

with $X[k]$ denoting the k^{th} element of vector $\mathbf{X}$ with a size of N. Let $\mathbf{x}$ denote the output vector of IDFT block, its n^{th} element, $n = 0,\ 1, \cdots,\ N-1$ can be expressed as

$$x[n] = \frac{1}{\sqrt{N}} \sum_{k=0}^{N-1} X[k] \exp\left(j2\pi nk/N\right), \tag{6.2}$$

After appending CP to the vector $\mathbf{x}$, we have

$$\tilde{\mathbf{x}} = \begin{bmatrix} x[N-N_{cp}] & \cdots & x[N-1] & x[0] & \cdots & x[N-1] \end{bmatrix}^T, \tag{6.3}$$

where N_{CP} denotes the length of CP. It can be noted that $\tilde{\mathbf{x}}$ is bipolar and real-valued signal. A DC bias is added to shift the negative values to the positive region before modulating the LED. Since the Fourier transform of DC must be zero everywhere except at $k = 0$ subcarrier, we drop DC bias from the formulations in the following. With $\tilde{x}[n]$ denoting the n^{th} element of vector $\tilde{\mathbf{x}}$ in Eq. (6.3), time-domain waveform that modulates the LED's intensity can be expressed as

$$x_s(t) = \sqrt{P} \sum_{n=0}^{(N-1)+N_{cp}} \tilde{x}[n]\, \delta\left(t - nT_s\right), \tag{6.4}$$

where P, $\delta(\cdot)$ and T_s are, respectively, average electrical transmit power, Dirac delta function and pulse duration. The received electrical time domain signal at the l^{th} node can be expressed as

$$\tilde{y}_l(t) = \left[R\sqrt{P} \sum_{n=0}^{(N-1)+N_{cp}} \tilde{x}[n]\delta\left(t - nT_s\right) \right] \otimes h_l(t) + w_l(t), \tag{6.5}$$

where R is the photodetector responsivity and $w_l(t)$ is the AWGN at the l^{th} node with zero mean and variance of σ_n^2. In Eq. (6.5), $h_l(t)$ denotes the CIR between the central unit and the l^{th} node (see Section 6.2.3). Let $w_l(n)$, $\tilde{y}_l(n)$ and $h_l(n)$ denote respectively the sampled version of $w_l(t)$, $\tilde{y}_l(t)$ and $h_l(t)$. Furthermore, let $y_l(n)$ denote the received time-domain signal at the l^{th} node after CP removal from $\tilde{y}_l(n)$. It can be expressed as

$$y_l(n) = \sqrt{P}Rx(n) \otimes h_l(n) + w_l(n), \quad n = 0, 1, \cdots, N-1 \cdot \tag{6.6}$$

The corresponding frequency-domain signal is given by

$$Y_l(k) = \sqrt{P}RX(k)H_l(k) + W_l(k), \quad k = 1, \cdots, N/2 - 1 \cdot \tag{6.7}$$

where $H_l(k)$ and $W_l(k)$ are the k^{th} element of N-point DFT of $h_l(n)$ and $w_l(n)$, respectively.

6.2.2 Resource Allocation

In this section, we investigate joint subcarrier allocation and bit loading in an effort to achieve fairness among sensor nodes, i.e., identical data rate for each node, while satisfying a maximum acceptable BER ($BER_{\max}$). Let $n_{l,k}$ denote the number of bits loaded on the k^{th} subcarrier for the l^{th} node. The number of bits loaded for the l^{th} node can be therefore written as

$$n_l = \sum_{k \in S_{K_l}} n_{l,k}, \quad l = 1, \cdots, L \cdot \tag{6.8}$$

We define the overall data rate as the total number of loaded bits per OFDMA symbol, i.e., for all nodes [137]. Therefore, we have

$$n = \sum_{l=1}^{L} n_l \cdot \tag{6.9}$$

The objective is to maximize the overall data rate subject to the constraint that the data rate for nodes becomes identical. Furthermore, as an additional constraint, the BER of each node should not exceed a pre-defined value of $BER_{\max}$. Therefore, the optimization problem can be formulated as

$$\begin{aligned} &\max \quad \text{n} \\ &\text{s.t.}: \quad n_l = n_j, \quad l \neq j \\ &\qquad\quad BER_l \leq BER_{\max}, \; l = 1, \cdots, L, \end{aligned} \tag{6.10}$$

where BER_l denotes the average BER of the l^{th} node. It is given by

$$BER_l = \frac{1}{N_l} \sum_{k \in S_{K_l}} BER_{l,k}, \tag{6.11}$$

where $BER_{l,k}$ denotes the BER on the k^{th} subcarrier of the l^{th} node. For 2-PSK and M-QAM, $BER_{l,k}$ can be expressed as [138]

$$BER_{l,k} \approx \frac{2}{\log_2 (U \times J)} \left(\frac{U-1}{U} + \frac{J-1}{J} \right) Q \left(\sqrt{\frac{6\,SNR_{l,k}}{U^2 + J^2 - 2}} \right), \tag{6.12}$$

where $Q(.)$ is the Gaussian Q-function and $U \times J = M$ with M denoting the modulation size. In Eq. (6.12), $SNR_{l,k}$ defines the received SNR for the k^{th} subcarrier at the l^{th} node. Based on Eq. (6.7) on the previous page, it is given by $SNR_{l,k} = \overline{SNR}\, R^2 H_l^2 (k)$ where $\overline{SNR} = P/\sigma_n^2$ is average electrical transmit SNR.

To solve Eq. (6.10) on the preceding page, we use an adaptive algorithm inspired by a similar algorithm from [139] which was earlier proposed in the context of radio-frequency wireless systems with different constraints. A pseudo-code is also provided in Algorithm 3 on the next page.

We first select the set of subcarriers that should not be assigned to the l^{th} node. This set is denoted as $\overline{S_{K_l}}$, $l = 1, 2, \ldots, L$. To do so, we assume all subcarriers are assigned to the l^{th} node and load all subcarriers by one bit (i.e., 2-PSK). If the node can achieve the $BER_l \leq BER_{\max}$ by this assignment, then we have $\overline{S_{K_l}} \in \varnothing$. Otherwise, the k^{th} subcarrier that imposes highest BER will be unloaded and added to $\overline{S_{K_l}}$. This will continue until the l^{th} node can achieve the $BER_l \leq BER_{\max}$.

After deciding on $\overline{S_{K_l}}$, $l = 1, 2, \ldots, L$, we initiate loading by selecting one subcarrier for each node and load it by one bit. To do so, the k^{th} subcarrier that satisfies $k^{\text{th}} \notin \overline{S_{K_l}}$ and imposes the least BER for the l^{th} node will be selected. If the subcarriers that yield the least BER for different nodes are different, the selected subcarrier will be loaded with one bit. Otherwise, if the subcarrier that imposes the least BER is the same for the l^{th} node and the j^{th} node, the priority is for the node that imposes the highest BER to load its selected subcarrier. The modulation level is then increased for the selected subcarrier and the algorithm stops when the $BER_{\max}$ is reached or this subcarrier is loaded by maximum number of bits of $n_{\max} = \log_2(M_{\max})$ with $M_{\max}$ denoting the highest modulation size.

We continue assigning subcarriers and bit loading by giving the priority to the node with less rate in order to increase its rate. If different nodes have the same rate, we give priority to the node with the highest BER. Until this stage, subcarriers are distributed and loaded but nodes may not have exactly the same number of bits per OFDM symbol. Therefore, the number of bits for subcarriers that impose the highest BER for the nodes with more rate will be decreased accordingly.

Algorithm 3 Proposed adaptive algorithm.

1: **Initialize:**

$S_{K_l} = \{\}\ \forall l,\ l = 1, 2, \cdots, L.\ \overline{S_{K_l}} = \{\}\ \forall l,\ l = 1, 2, \cdots, L.$

2: **Starting algorithm:**

Step 1: Searching for all subcarriers that should not be assigned to the l^{th} node.

3: **for** $l = 1$ to L **do**

Assume all subcarriers are assigned to the l^{th} node and load them by one bit.

Compute the average BER for this assignment by

$$BER_l = \frac{1}{N/2-1} \sum_{k=1}^{N/2-1} BER_{l,k}$$

4: **if** $BER_l \leq BER_{\max}$ **then** $\overline{S_{K_l}} \in \emptyset$

5: **else**

6: **while** $BER_l > BER_{\max}$ **do**

- Un-loaded k^{th} subcarrier that imposes the highest BER.
- Add k^{th} subcarrier to $\overline{S_{K_l}}$.
- Compute new BER_l by using Eq. (6.11) on the preceding page

7: **end while**

8: **end if**

9: **end for**

Step 2: Selecting the first subcarrier for each node.

for $l = 1$ to L **do**

  Add the subcarrier that imposes the least BER to S_{K_l} and $\overline{S_{Kj}}\,\forall j,\ j = 1, 2, \cdots, L$, $j \neq l$.

end for

if subcarrier that imposes the least BER is the same for different nodes **then**

- Assign it to the node that imposes the highest BER on the selected subcarrier.
- Select another subcarrier for the other node which is the next subcarrier to impose the least BER.
- Update S_{K_l} and $\overline{S_{Kl}}$.

end if

Step 3: Loading the first subcarrier for each node.

for $l = 1$ to L **do**

  while $BER_{l,k} < BER_{\max}$ and $n_{l,k} \leq n_{\max}$ **do**

  - Increase number of bits for the k^{th} subcarrier.
  - Compute new $BER_{l,k}$ by Eq. (6.12) on page 90.
  - Update n_l, i.e., $n_l \leftarrow n_{l,k}$.

  end while

end for

Step 4: Step 4. Assigning subcarriers and loading bits.

while some subcarriers are empty **do**

- Select the l^{th} node that satisfies $n_l = \min(\{n_1, n_2, \cdots, n_L\})$ if exists. Otherwise, select the l^{th} node that satisfies $BER_l = \max(\{BER_1, BER_2, \cdots, BER_L\})$
- Select the k^{th} subcarrier for the l^{th} node that satisfies $k \notin \overline{S_{K_l}}$ and impose the least BER
- Add the selected subcarrier to S_{K_l} and $\overline{S_{Kj}}\,\forall j,\ j = 1, 2, \cdots, L$, $j \neq l$.

  while $BER_l < BER_{\max}$ and $n_{l,k} \leq n_{\max}$ **do**

  - Increase the number of bits on the k^{th} subcarrier
  - Compute new BER_l by using Eq. (6.11) on page 90
  - Compute n_l by using Eq. (6.8) on page 89

end while

end while

Step 5: Ensuring equal data rate for all nodes.

for $l = 1$ to L **do**

while $n_l > \min(\{n_1, n_2, \cdots, n_L\})$ **do**

- Number of bits loaded on the k^{th} subcarriers that impose the highest BER will be decreased, i.e., $n_{l,k} \leftarrow n_{l,k} - 1$.
- Compute n_l by using Eq. (6.8) on page 89

end while

end for

6.2.3 Results and Discussions

In this section, we present simulation results for the underwater adaptive DCO-OFDMA system under consideration. As illustrated in Figure 27 on the next page, we consider a downlink scenario where the central command unit is in the form of an Autonomous Underwater Vehicle (AUV). The AUV is equipped with a cube-shaped transmitter. From one face, it is attached to the bottom of AUV. Other five faces of this cube are equipped with LED transmitters with a viewing angle of 100°. A receiver with an aperture diameter of 50 cm [11] and field of view of 180° [11] is considered for each sensor. Other channel parameters are provided in Table 5.

Table 5: Channel Parameters.

Object specifications	AUV and sensors: Galvanized steel metal Sea bottom: Mud
Transmitter specifications	Cube shaped transmitter with 5 LEDs Power: 1 Watt per each LED
Receiver specifications	Responsivity of photodetector: 0.53 (A/W)
Water type	Coastal-S_8 group (C_C: 0.8$\sim$2.2 mg/m^3)
Scattering phase function	OTHG
Mean cosine of scattering angles	0.9470

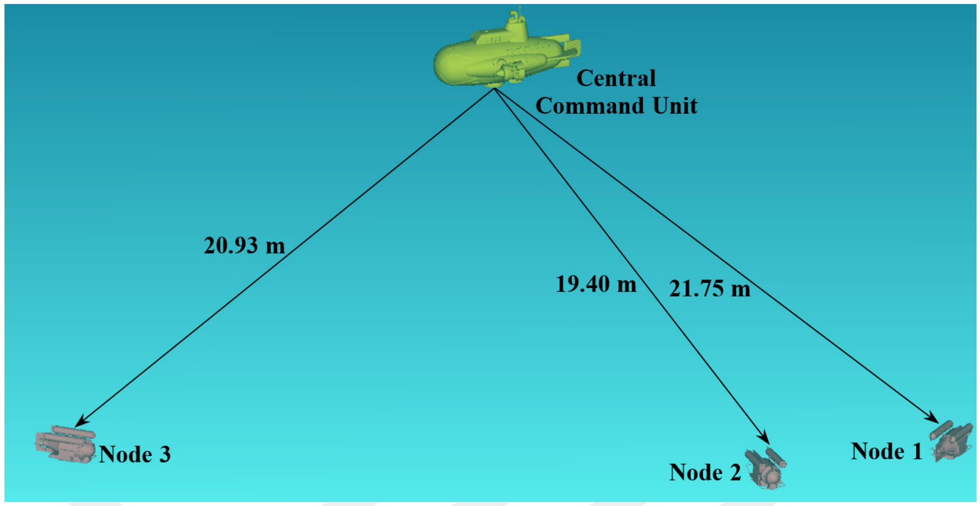

Figure 27: Underwater scenario under consideration.

We assume coastal water with an extinction coefficient of 0.3171 m^{-1}. We use the same methodology in [140] based on non-sequential ray tracing and obtain the CIRs, their sampled versions and corresponding frequency responses (see Figure 28 on the next page). It is observed from Figure 28(a) on the following page that the delay spread exceeds 19 ns, 16 ns and 15 ns, respectively, for first, second and third nodes. It can be readily verified that these channels exhibit frequency-selectivity if high-speed transmission in the order of hundreds of Mb/s are targeted.

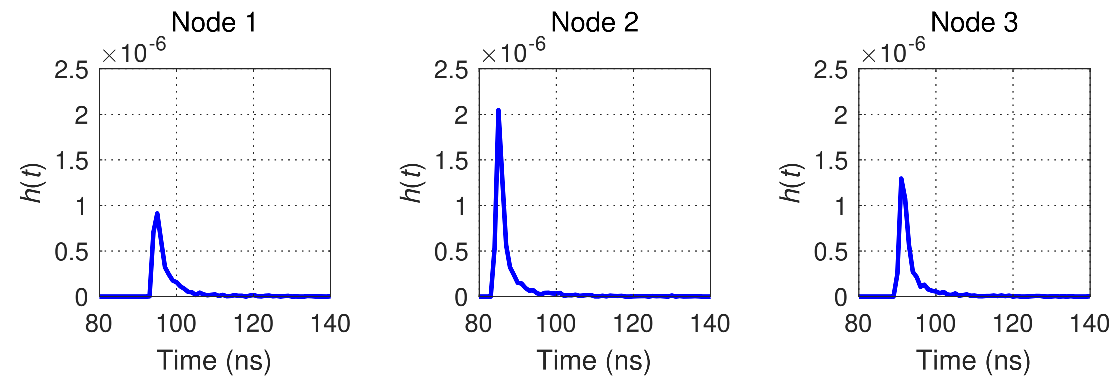

(a)

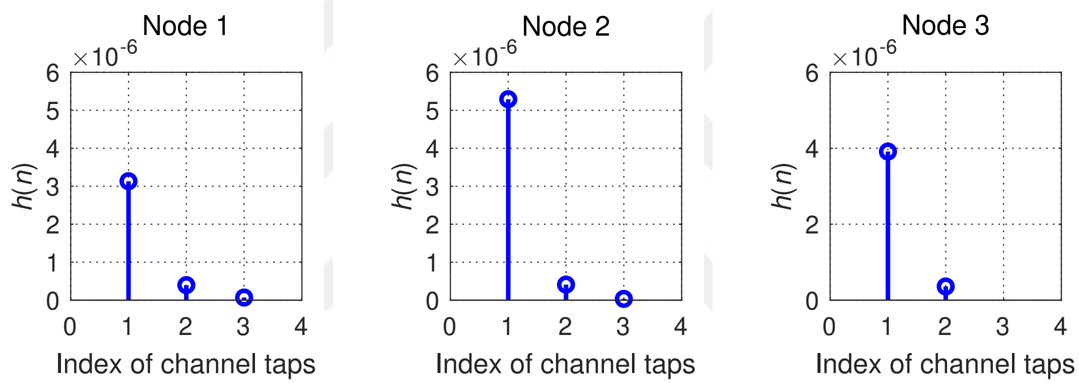

(b)

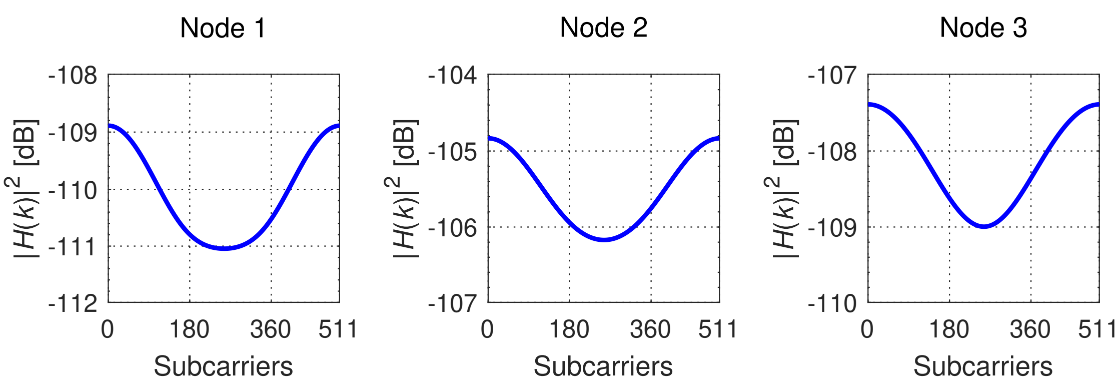

(c)

Figure 28: (a) CIR, (b) sampled CIR and (c) corresponding frequency response for Nodes 1, 2, 3.

We consider an OFDMA system with photodetector responsivity of $R = 0.53$ A/W and pulse duration of $T_s = 8$ ns. We assume that the number of subcarriers is set as $N = 512$. Because of Hermitian symmetry, only $N/2 - 1 = 255$ subcarriers carry data. We assume the deployment of 2-PSK and M-QAM, $M = 4, 8, \ldots, 128$.

In Figure 29 on the next page, we assume transmit SNR of $\overline{SNR} = 140$ dB[1] and present allocated subcarriers for each node. We impose the condition that the BER of each node should not exceed $BER_{\max} = 1 \times 10^{-6}$. We observe that the number of allocated subcarriers to the l^{th} node, l =1, 2 and 3 are, respectively, $N_l = 98$, 76 and 81 subcarriers. For Node 1, among its 98 allocated subcarriers, 35 subcarriers are loaded with 4 bits (i.e., 16-QAM) and 63 subcarriers are loaded with 5 bits (i.e., 32-QAM). For Node 2, among its 76 allocated subcarriers, 1 subcarrier is loaded with 4 bits (i.e., 16-QAM), 74 subcarriers are loaded with 6 bits (i.e., 64-QAM) and 1 subcarrier is loaded with 7 bits (i.e., 128-QAM). For Node 3, among its 81 allocated subcarriers, 1 subcarrier is loaded with 2 bits (i.e., 4-QAM), 27 subcarriers are loaded with 5 bits (i.e., 32-QAM) and 53 subcarriers are loaded with 6 bits (i.e., 64-QAM). It can be readily verified that all three nodes achieve identical total number of loaded bits per OFDM symbol of $n_l = 455$ bits, l =1, 2, 3. Based on Eq. (6.9) on page 89, the optimized overall data rate is then calculated as $n = 1365$ bits per OFDM symbol. Utilizing Eq. (6.11) on page 90, we can verify that the achieved BERs for this particular loading of $BER_1 = 0.94 \times 10^{-6}$, $BER_2 = 0.13 \times 10^{-6}$ and $BER_3 = 0.87 \times 10^{-6}$ are lower than the pre-defined constraint of $BER_{\max} = 1 \times 10^{-6}$.

[1] Given the path loss values, this is typical for VLC, see e.g., [141–144] for possible range of transmit SNR values.

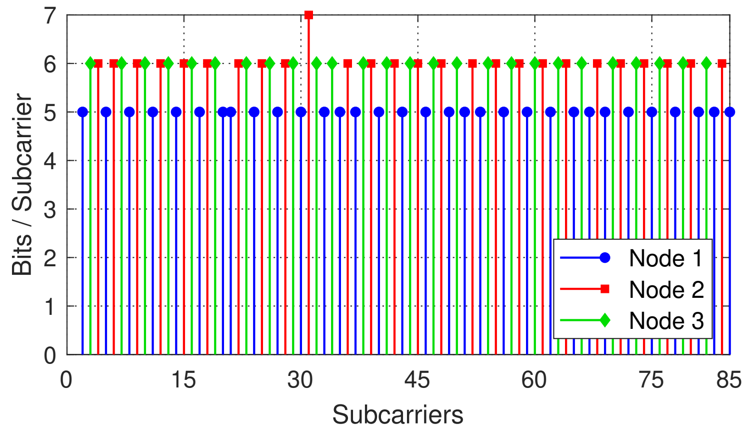

(a)

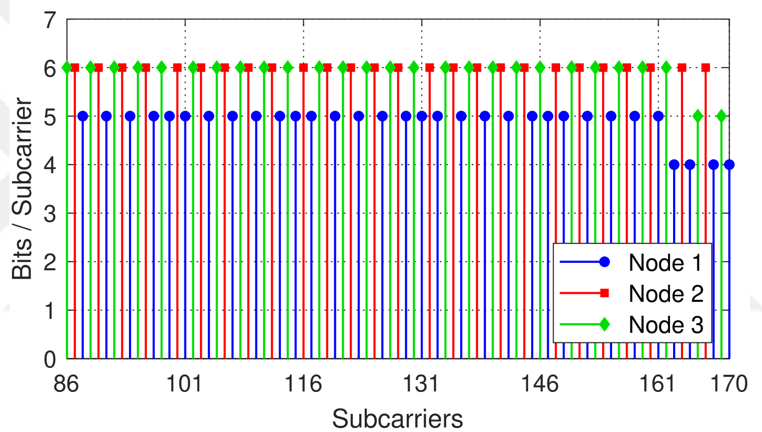

(b)

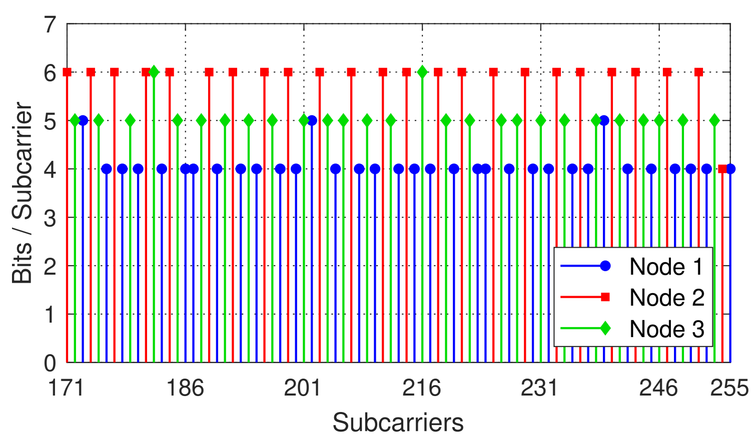

(c)

Figure 29: Allocated subcarriers for Node 1, Node 2 and Node 3: (a) $0 \leq k \leq 85$ (b) $86 \leq k \leq 170$ and (c) $171 \leq k \leq 255$ ($BER_{\max} = 1 \times 10^{-6}$ and $\overline{SNR} = 140$ dB).

In Figure 30, we present the number of bits loaded on set of subcarriers for each node (i.e., n_l, l =1, 2 and 3) versus $\overline{SNR}$. We assume $BER_{\max} = 1 \times 10^{-6}$. It can be observed that as $\overline{SNR}$ increases, n_l increases. Moreover, it is observed that no bits are loaded when transmit SNR lies below 125 dB. This is due to the fact that $BER_{\max} = 1 \times 10^{-6}$ cannot be satisfied even with smallest modulation size under consideration. It can be verified that the number of bits loaded for all nodes are identical as targeted by the adaptive algorithm and saturates at $n_l = 595$ bits, l =1, 2 and 3 when $\overline{SNR}$ exceeds 146.7 dB. Because at this SNR, all subcarriers experience strong channel gains and can be loaded with the highest modulation size of M =128-QAM.

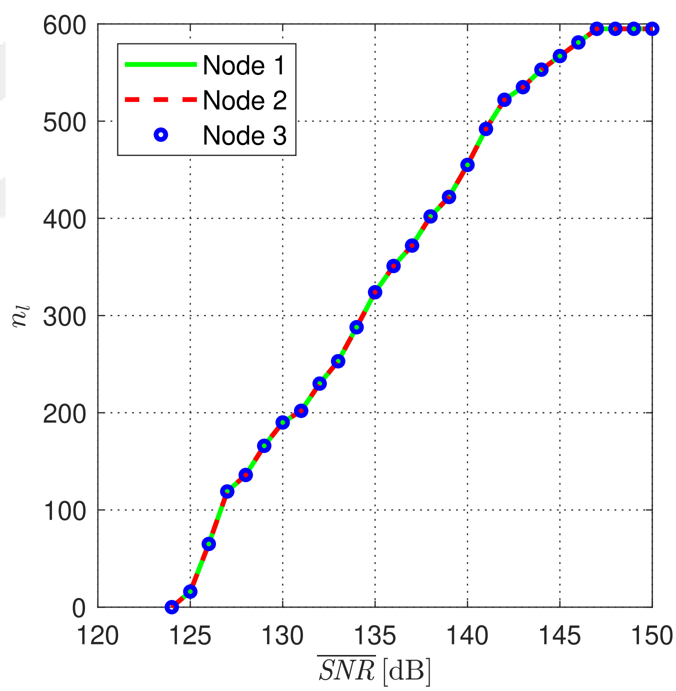

Figure 30: Effect of SNR on the number of bits loaded for the l^{th} node, $l = 1,2,3$.

In Figure 31 on the next page, we discuss the effect of different $BER_{\max}$ values. We assume $\overline{SNR}$ =140 dB. It is observed that the number of bits loaded on set of subcarriers for all nodes are identical, i.e., $n_1 = n_2 = n_3$. They are found as 455 bits for $BER_{\max} = 1 \times 10^{-6}$, 496 bits for $BER_{\max} = 1 \times 10^{-5}$, 531 bits for $BER_{\max}$=1×10^{-4}, 562 bits for

$BER_{\max} = 1 \times 10^{-3}$ and 595 bits for $BER_{\max} = 1 \times 10^{-2}$. Our results demonstrate that as $BER_{\max}$ increases, the number of loaded bits increases since higher BER values may be satisfied with higher modulation orders.

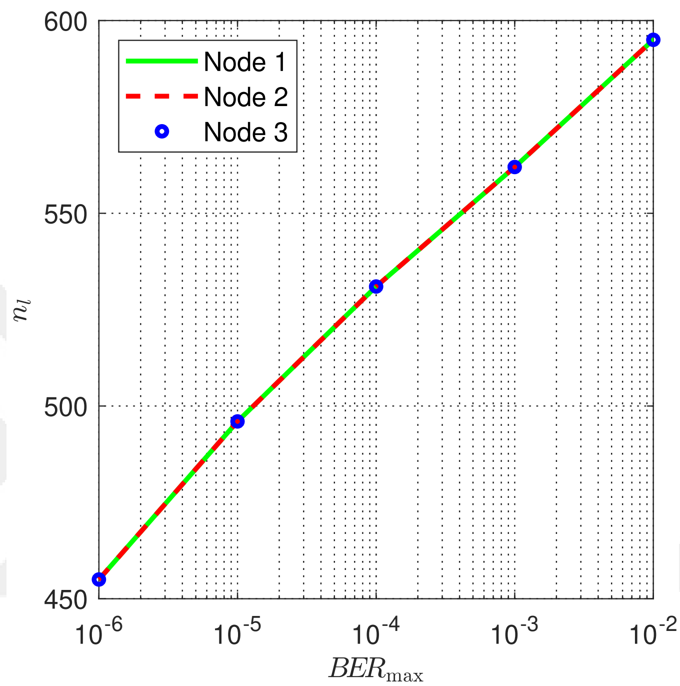

Figure 31: Effect of $BER_{\max}$ on the number of bits loaded for the l^{th} node, $l = 1, 2, 3$.

6.3 NOMA

In this section, we consider a clusterhead that communicates with several underwater sensor nodes and derive a closed-form expression for the NOMA system capacity over lognormal fading channels, which are encountered in such propagation environments. To gain more insights into the performance of the underlying system, we also derive a tight approximate expression for the user's capacity.

6.3.1 System Model

We consider a NOMA-enabled UVLC where a clusterhead communicates with K underwater sensor nodes, as depicted in Figure 32 on the following page. Each node is assumed to be at a distance d_k, $k = 1, 2, \cdots, K$, from the clusterhead. Let P_T, x_k and α_k denote the available power budget shared by all nodes, the transmitted symbol which can be any unipolar modulation technique such as PAM and power allocation coefficient of the k^{th} node, respectively. Therefore, the power of the k^{th} node is given by $P_k = \alpha_k P_T$. For the case of two nodes, power allocation coefficients of α and $1-\alpha$ are assigned to the first and second nodes, respectively.

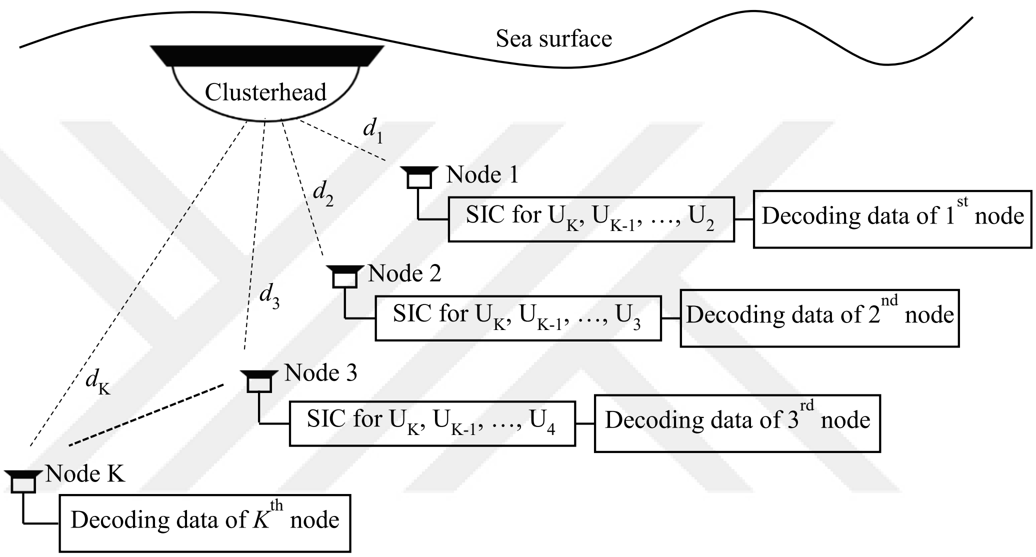

Figure 32: NOMA for downlink UVLC.

The normalized average power at the clusterhead is subject to $\sum_{k=1}^{K} \alpha_k = 1$. It should be noted that splitting the power among nodes allows the practical realization of Successive Interference Cancellation (SIC), i.e., it increases the ability of the receiver to eliminate the effect of high power signals and perform reliable signal detection. In other words, the receiver can successively decode the higher power signals and consider all other signals as interference, subtract the decoded signal from the superimposed signal and finally detect the intended signal. Then, the clusterhead superimposes the information waveforms, i.e., the transmited signal is $\mathscr{X} = \sum_{k=1}^{K} \sqrt{P_k} x_k$. Based on this, the received signal at the k^{th} node, assuming unity photodetector responsivity, is given by

$$y_k = h_k I_k \mathscr{X} + w_k, \tag{6.13}$$

where w_k denotes the additive noise at the receiver of the k^{th} node. In Eq. (6.13) on the previous page, I_k are random variables characterizing the fading induced by the underwater turbulence, whereas h_k are deterministic terms that characterize the attenuation loss over the link distance between the clusterhead and the k^{th} node, i.e., d_k. h_k for semi-collimated laser sources with Gaussian beam shape is expressed as [11]

$$h_k \approx D_R^2 \theta_F^{-2} d_k^{-2} \exp\left(-c D_R^{\rho} \theta_F^{-\rho} d_k^{1-\rho}\right), \tag{6.14}$$

where θ_F and D_R denote full-width transmitter beam divergence angle and receiver aperture diameter, respectively. In Eq. (6.14), ρ and c represent correction and extinction coefficients, which are both water type dependent.

It is recalled that, power allocation in NOMA systems is determined based on the channels condition between the transmitter and the receiving nodes. Specifically, nodes with strong channel gains (i.e., closest nodes to the clusterhead) are allocated lower power coefficients, while high power coefficients are assigned to nodes with weak channel gain. Without loss of generality, we assume that channel gains are ordered in a descending form, i.e., $h_1 > h_2 > \cdots > h_K$, hence the power allocation coefficients are then given as $\alpha_K > \cdots > \alpha_2 > \alpha_1$. Since the highest transmit power is assigned to the K^{th} node, this node does not perform SIC. Similarly, since the least transmit power is assigned to the first node, this node will decode the data of $K-1$ nodes before decoding its own signal (see Figure 32 on the previous page). The PDF of the fading coefficient (I_k) under the assumption of weak turbulence is given by [6]

$$f_{I_k}(I_k) = \frac{1}{I_k \sqrt{2\pi \left(4\sigma_{x_k}^2\right)}} \exp\left(-\frac{\left(\ln(I_k) - 2\mu_{x_k}\right)^2}{2\left(4\sigma_{x_k}^2\right)}\right), \tag{6.15}$$

where μ_{x_k} and $\sigma_{x_k}^2$ denote the mean and variance of the log-amplitude coefficient, respectively. To ensure that the fading coefficient does not change the value of average power, the fading amplitude is normalized such that $\mathrm{E}[I_k] = 1$, which implies $\mu_{x_k} = -\sigma_{x_k}^2$. The variance can be written in terms of the scintillation index ($\sigma_{I_k}^2$) as $\sigma_{x_k}^2 = 0.25 \ln\left(\sigma_{I_k}^2 + 1\right)$.

Scintillation index for laser sources with Gaussian beam shape can be calculated by [145, Eq. (7)] and [51, Eq. (16)].

6.3.2 Capacity Analysis

For a reliable data detection, each node in the USN performs SIC to reduce the multi-user interference. In particular, nodes successively cancel out the interference from those signals with higher power, and then decode their own signals. It is worth noting that lower power levels signals are treated as noise.

Assuming perfect SIC at the k^{th} node, the conditional SNR, i.e., conditioned on the fading coefficient I_k for the k^{th} node becomes

$$\mathrm{SNR_k} = \frac{\mathrm{P_k h_k^2 I_k^2}}{\mathrm{N_0\, W + h_k^2 I_k^2 \sum_{i=1}^{k-1} P_i}}, \tag{6.16}$$

where N_0 is the noise power spectral density and W is the corresponding bandwidth. Utilizing Eq. (6.16), the conditional capacity assuming perfect cancellation, i.e., the maximum conditional NOMA capacity can be written as

$$R_k = W \log_2 \left(1 + \frac{P_k h_k^2 I_k^2}{N_0\, W + h_k^2 I_k^2 \sum_{i=1}^{k-1} P_i} \right). \tag{6.17}$$

Therefore, the average capacity of the k^{th} node can be calculated by averaging the capacity in Eq. (6.17) over the PDF of the turbulence in Eq. (6.15) on the preceding page as

$$\begin{aligned} \overline{R_k} = \frac{W}{\sqrt{2\pi \left(4\sigma_{x_k}^2\right)}} \int_0^\infty \log_2 \left(1 + \frac{P_k h_k^2 I_k^2}{N_0 W + h_k^2 I_k^2 \sum_{i=1}^{k-1} P_i} \right) \\ \times I_k^{-1} \exp\left(- \frac{\left(\ln\left(I_k\right) - 2\mu_{x_k}\right)^2}{2\left(4\sigma_{x_k}^2\right)} \right) d_{I_k}. \end{aligned} \tag{6.18}$$

If the integration variable is changed to $x = \ln\left(I_k\right)$, Eq. (6.18) can be expressed as

$$\overline{R_k} = \int_{-\infty}^{\infty} g\left(x\right) f_x\left(x\right) d_x. \tag{6.19}$$

In Eq. (6.19) on the preceding page, $g(x)$ and $f_x(x)$ are defined, respectively, as

$$g(x) = W \log_2 \left(1 + \frac{P_k h_k^2 \exp(2x)}{N_0 W + h_k^2 \exp(2x) \sum_{i=1}^{k-1} P_i} \right). \tag{6.20}$$

$$f_x(x) = \frac{W}{\sqrt{2\pi \left(4\sigma_{x_k}^2\right)}} \exp\left(-\frac{\left(x - 2\mu_{x_k}\right)^2}{2\left(4\sigma_{x_k}^2\right)} \right). \tag{6.21}$$

With $\mathrm{E}[\cdot]$ denoting the expectation operator, integration in Eq. (6.19) on the previous page can be written in the form of $\mathrm{E}[g(x)]$, $x \sim \mathcal{N}\left(2\mu_{x_k}, 4\sigma_{x_k}^2\right)$ indicates that x follows the normal distribution with mean $2\mu_{x_k}$ and variance $4\sigma_{x_k}^2$. If we utilize Holtzmann's Gaussian approximation [113], the average capacity of the k^{th} node in Eq. (6.19) on the preceding page can be approximated as weighted sum of $g(x)$ by replacing x with $2\mu_{x_k}$, $2\mu_{x_k} - 2\sqrt{3}\sigma_{x_k}$ and $2\mu_{x_k} + 2\sqrt{3}\sigma_{x_k}$ as

$$\begin{aligned}
\overline{R_k} \approx & \frac{2}{3} W \log_2 \left(1 + \frac{P_k h_k^2 \exp\left(4\mu_{x_k}\right)}{N_0 W + h_k^2 \exp\left(4\mu_{x_k}\right) \sum_{i=1}^{k-1} P_i} \right) \\
& + \frac{1}{6} W \log_2 \left(1 + \frac{P_k h_k^2 \exp\left(4\mu_{x_k} + 4\sqrt{3}\sigma_{x_k}\right)}{N_0 W + h_k^2 \exp\left(4\mu_{x_k} + 4\sqrt{3}\sigma_{x_k}\right) \sum_{i=1}^{k-1} P_i} \right) \\
& + \frac{1}{6} W \log_2 \left(1 + \frac{P_k h_k^2 \exp\left(4\mu_{x_k} - 4\sqrt{3}\sigma_{x_k}\right)}{N_0 W + h_k^2 \exp\left(4\mu_{x_k} - 4\sqrt{3}\sigma_{x_k}\right) \sum_{i=1}^{k-1} P_i} \right).
\end{aligned} \tag{6.22}$$

Asymptotic NOMA Capacity: In the following, we apply the approximation upon which $\mathrm{E}\left[\log_2\left(1 + a/b\right)\right] \approx \log_2\left(1 + \mathrm{E}[a]/\mathrm{E}[b]\right)$ [146, Eq. (35)], Eq. (6.19) on the previous page can be written as

$$\overline{R_k} = W \log_2 \left(1 + \frac{P_k h_k^2 \mathrm{E}[\exp(2x)]}{N_0 W + h_k^2 \sum_{i=1}^{k-1} P_i \mathrm{E}[\exp(2x)]} \right), \tag{6.23}$$

where $\mathrm{E}[\exp(2x)]$ can be obtained by taking the expectation of $\exp(2x)$ over the PDF of x in Eq. (6.21) on the preceding page as

$$\mathrm{E}[\exp(2x)] = \int_{-\infty}^{\infty} \frac{\exp(2x)}{\sqrt{2\pi\left(4\sigma_{x_k}^2\right)}} \exp\left(-\frac{\left(x-2\mu_{x_k}\right)^2}{2\left(4\sigma_{x_k}^2\right)}\right) d_x. \tag{6.24}$$

The integration in Eq. (6.24) can be rearranged as.

$$\mathrm{E}[\exp(2x)] = \frac{\exp\left(8\sigma_{x_k}^2 + 4\mu_{x_k}\right)}{\sqrt{2\pi\left(4\sigma_{x_k}^2\right)}} \int_{-\infty}^{\infty} \exp\left(-\frac{\left(x-\left(8\sigma_{x_k}^2+2\mu_{x_k}\right)\right)^2}{2\left(4\sigma_{x_k}^2\right)}\right) d_x. \tag{6.25}$$

It can be readily verified that the solution of Eq. (6.25) is given as $\mathrm{E}[\exp(2x)] = \exp\left(8\sigma_{x_k}^2 + 4\mu_{x_k}\right)$. If we replace this within Eq. (6.23) on the previous page, we have

$$\overline{R_k} \approx W\log_2\left(1 + \frac{P_k h_k^2 \exp\left(8\sigma_{x_k}^2 + 4\mu_{x_k}\right)}{N_0 W + h_k^2 \exp\left(8\sigma_{x_k}^2 + 4\mu_{x_k}\right) \sum\limits_{i=1}^{k-1} P_i}\right). \tag{6.26}$$

The sum capacity for NOMA can be written as $R_T = \sum_{k=1}^{K} \overline{R_k}$

It should be noted that the closer the nodes, the larger the interference, which will result in the low SNR regime. Therefore, it is expected that the derived asymptotic expression will deviate from exact expression when nodes have quite same propagation distances.

In the following, we consider asymptotically high SNR or asymptotically high transmit power (i.e. $P_T \to \infty$). It can be readily checked that Eq. (6.26) for $P_T \to \infty$ reduces to

$$\overline{R_k}_{P_T\to\infty} \approx \begin{cases} W\log_2\left(\dfrac{P_T\alpha_1 h_1^2 \exp\left(8\sigma_{x_1}^2+4\mu_{x_1}\right)}{N_0 W}\right) & ,k=1 \\ W\log_2\left(1+\dfrac{\alpha_k}{\sum\limits_{i=1}^{k-1}\alpha_i}\right) & ,k>1 \end{cases} \tag{6.27}$$

This equation suggests that as P_T approaches ∞, the effect of turbulence is encountered only in the first node. On the other hand, the capacity of other nodes is controlled by the power allocation coefficients.

6.3.3 Results and Discussions

In this section, we present the capacity of wireless nodes in NOMA UVLC system, assuming perfect cancellation in the SIC receiver. To that end, we also validate our derived closed-form expression in Eq. (6.22) on page 103, closed-form approximate capacity expression in Eq. (6.26) on the preceding page and asymptotic capacity expression in Eq. (6.27) on the previous page. Unless otherwise stated, we assume two nodes and consider receiver aperture diameter of $D_R = 5$ cm, full-width transmitter beam divergence angle of $\theta_{\mathrm{F}} = 6°$, noise power spectral density of $N_0 = 10^{-22}$ W/Hz, bandwidth of $W = 200$ MHz and total transmit power of $P_T = 1$ W. Assuming clear ocean, the extinction and correction coefficients are given, respectively, as $c = 0.15$ and $T = 0.05$ [11]. We further calculate the scintillation index (σ_I^2) based on [145, Eq. (7)] in conjunction with [51, Eq. (16)] assuming salinity of 35 PPT and temperature of 20 °C. Utilizing the computed $\sigma_{I_k}^2$[2], we calculate log-amplitude variance ($\sigma_{x_k}^2$) considering different link distances of $d_k = 1, 2, \cdots, 20$ m. The corresponding values of deterministic channel attenuation coefficient (h_k) and log-amplitude variance are listed in Table 6.

Table 6: Channel attenuation coefficients and log-amplitude variances.

d_k	1 m	2 m	3 m	4 m	5 m
h_k	1.97×10^{-1}	4.31×10^{-2}	1.68×10^{-2}	8.31×10^{-3}	4.68×10^{-3}
$\sigma_{x_k}^2$	8.36×10^{-6}	6.69×10^{-5}	2.25×10^{-4}	5.33×10^{-4}	1.04×10^{-3}
d_k	6 m	7 m	8 m	9 m	10 m
h_k	2.87×10^{-2}	1.86×10^{-3}	1.26×10^{-3}	8.77×10^{-4}	6.29×10^{-4}
$\sigma_{x_k}^2$	1.79×10^{-3}	2.83×10^{-3}	4.20×10^{-3}	5.94×10^{-3}	8.09×10^{-3}
d_k (m)	11	12	13	14	15
h_k	4.60×10^{-4}	3.42×10^{-4}	2.58×10^{-4}	1.97×10^{-4}	1.52×10^{-4}
$\sigma_{x_k}^2$	1.07×10^{-2}	1.37×10^{-2}	1.73×10^{-2}	2.13×10^{-2}	2.59×10^{-2}
d_k (m)	16	17	18	19	20
h_k	1.19×10^{-4}	9.35×10^{-5}	7.40×10^{-5}	5.90×10^{-5}	4.73×10^{-5}
$\sigma_{x_k}^2$	3.09×10^{-2}	3.65×10^{-2}	4.26×10^{-2}	4.92×10^{-2}	5.63×10^{-2}

In Figure 33 on the next page, we present the capacity of NOMA and discuss the effect

[2]For computing log-amplitude variance, we assume a dissipation rate of mean-squared temperature of 1×10^{-3} $\mathrm{K}^2\mathrm{s}^{-3}$ and a dissipation rate of turbulent kinetic energy per unit mass of fluid of 1×10^{-2} $\mathrm{m}^2\mathrm{s}^{-3}$ (see Section 3.2).

of power allocation coefficient considering $d_T = d_1 + d_2 = 20$ m. Since d_1 is assumed to be shorter than d_2, we consider the range of $d_1 <$ (i.e. not equal) $d_T/2$. Since the received power at k^{th} node is proportional to h_k^2 and given the fact that power allocation coefficient is performed such that low transmits powers are assigned to the nodes with less severe channels and vice versa, we consider $\alpha_k \propto 1/h_k^2$, $k = 1, 2, \cdots, K$. Utilizing this and $\sum_{k=1}^{K} \alpha_k = 1$, we consider in simulation $\alpha_k = \left(1/h_k^2\right)/\sum_{i=1}^{K}\left(1/h_i^2\right)$, i.e., for two-node case $\alpha_1 = h_2^2/\left(h_1^2 + h_2^2\right)$ and $\alpha_2 = h_1^2/\left(h_1^2 + h_2^2\right)$. It can be observed from Figure 33 that our results demonstrate that the derived expression in Eq. (6.22) on page 103 provides excellent match to the analytical calculation based on Eq. (6.18) on page 102.

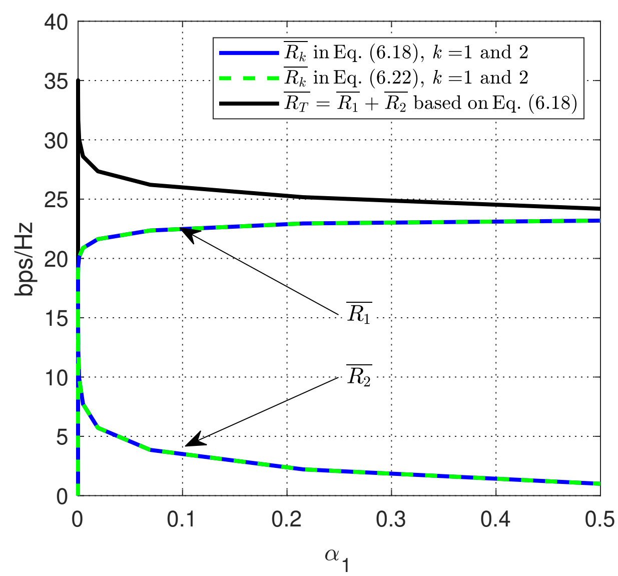

Figure 33: Capacity of NOMA downlink with two nodes.

It is also observed from Figure 33 that when $\alpha_1 = 0$, i.e., no power is allocated to the first node, its achievable capacity is zero. In this case, the second node achieves its highest capacity of $R_2 = 16.45$. It is noticed that the highest sum capacity is achieved when $\alpha_1 = 2.9487 \times 10^{-06}$ as $R_T = 35.02$. This corresponds to distances of d_1 = 2 m and d_2 = 18 m (*More discussion on the effect of distances is provided in* Figure 34 on the following page). On the other hand, when α_1 increases (i.e., $\alpha_2 = 1 - \alpha_1$ decreases), the capacity of the first node increases and the capacity of the second node decreases. It is also noted that the capacity of the first node (i.e., R_1) approaches the NOMA overall capacity while the capacity of the second node (i.e., R_2) approaches zero as α_1 increases.

In Figure 34, we study the effect of distance difference on performance. Therefore, we assume that $d_T = d_1 + d_2$ is fixed and consider two cases: $d_T = 15$ m and $d_T = 20$ m in Figures 34(a) and 34(b), respectively. Since d_1 is assumed to be shorter than d_2, we consider the range of $1\,\mathrm{m} \leq \mathrm{d}_1 \leq 7\,\mathrm{m}$ for both scenarios.

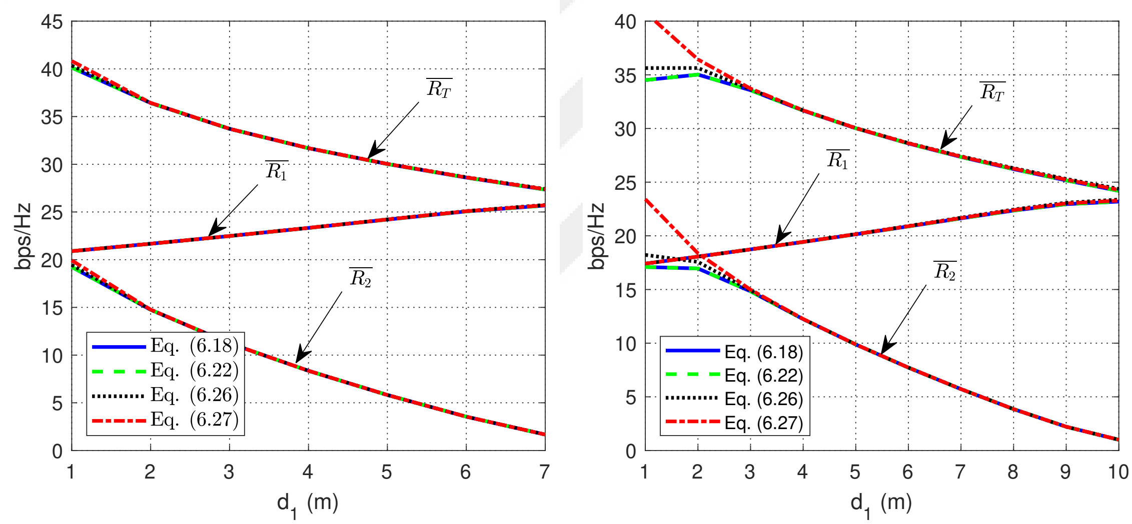

(a) (b)

Figure 34: Effect of distance on total rate of downlink NOMA with two nodes: (a) $d_1 + d_2 = 15$ m and (b) $d_1 + d_2 = 20$ m.

It can be observed that the overall capacity increases as distance difference increases (i.e., $d_2 - d_1$ increases). This is because the power allocation coefficient for the farthest point is much larger than the power allocation coefficient for the nearest point (i.e., $\alpha_2 \gg \alpha_1$). Therefore, node 1 has a good capacity due to small propagation distance and node 2 has a good capacity due to very small interference from node 1. On the contrary, we observe a decrease in the overall capacity as d_1 increases, d_2 decreases and hence $d_2 - d_1$ decreases. It can be observed from Figure 34(b) that the capacity of $d_1 = 1$ m (i.e., $d_2 - d_1 = 18\,\mathrm{m}$)

is less than the capacity when d_1 =2 m (i.e., $d_2 - d_1 = 16\,\mathrm{m}$). This is due to the fact that while assigning most of the power to the farthest point and very low amount of available power to the nearest point, the received power at the farthest point is low due to very low channel gain (i.e., $h_2 = 7.40 \times 10^{-5}$).

It can also be observed in Figure 34 on the preceding page that the derived closed-form approximate capacity expression in Eq. (6.26) on page 104 has an excellent match with the exact expressions for most of the range (i.e., $d_1 \leq d_T/2$). Similarly, the asymptotic capacity expression in Eq. (6.27) on page 104 which is derived assuming high transmit power (i.e., high SNR) provides excelent match with the exact capacity expression for most of the range. It can be further observed from Figure 34(b) on the previous page that these expressions deviate from the actual value when $d_1 = 1$ m. because both nodes will have a low SNR. The first node will have low SNR since most of the power is assigned to farthest node and the second node due to very low channel gain that is strongly decaying with propagation distance. It can also be observed that the capacity of the first node increases with increasing d_1, This is due to the considered power allocation strategy. In other words, $P_1 h_1^2$ increases with distance.

CHAPTER VII

CONCLUSIONS AND FUTURE WORK

In this chapter, we review the entire dissertation objectives and results. We emphasize on the contributions that this research made. At the end, we give some prospective points for future work.

7.1 Conclusions

In this Dissertation, we have, firstly, considered turbulence-free environment and investigated the maximum achievable link distance for point-to-point and relay-assisted transmission to achieve a specified targeted BER and investigated the benefits of link adaptation in the context of OFDM-based UVLC systems. For performance analysis over turbulence channels, we began by developing an accurate spatial power spectrum model of turbulent fluctuations of the sea-water refraction index that accurately describe how the fluctuation in both temperature and salinity contribute to the fluctuation in the refractive index and characterized the vertical UVLC optical turbulence cascaded channels. Utilizing our turbulence channel Models, we investigated the BER performance and Ergodic capacity of UVLC systems considering both weak and moderate/strong turbulence conditions, analyzed the asymptotic behavior of BER and determined the diversity orders. We then investigated the benefit of using different fading mitigation techniques on the performance of UVLC systems and proposed the concept of IDO to quantify diversity gains of communication systems over LN fading channels. In the last part of this dissertation, we consider a practical implementation of USNs that requires the design of multiple access systems for supporting several sensor nodes and considered both orthogonal and non-orthogonal multiple access. The contributions of this dissertation can be summarized as follows.

In Chapter 2, we used the newly proposed underwater closed-form expression for the optical channel coefficient to determine the maximum achievable distance for different water types. Since numerical results revealed that the transmission range is limited to a few tens of meters in typical scenarios, we further investigated the deployment of underwater relay-assisted systems. For a multi-hop system with equidistant relay placement in a serial fashion, we determined the maximum achievable distance for a given number of hops to satisfy a targeted end-to-end BER. Our results demonstrated that relay-assisted systems can effectively extend the transmission range, but the improvement factors are less than the number of hops [11, 147].

Then, we investigated the benefits of link adaptation in the context of OFDM-based underwater VLC systems. We considered two adaptive algorithms which aim to maximize the throughput while satisfying a pre-defined BER target. The algorithms differ from each other in the sense that the constraints are imposed either overall BER or per subcarrier BER. Our simulation results demonstrated the superiority of using adaptive algorithms over non-adaptive one in terms of average bit loading. Furthermore, the adaptive algorithm with overall BER constraint over-performed its counterpart with BER constraint per subcarrier [148].

Chapter 3 can be summarized as follow. In Section 3.2, we have obtained a simplified spatial power spectrum model of underwater turbulent fluctuations as an explicit function of eddy diffusivity ratio. Using the derived model, we have investigated the effect of eddy diffusivity on the scintillation index of the optical plane and spherical waves. Our results have demonstrated that the scintillation index is either significantly underestimated or over-estimated in previous works that have built on the assumption of unit diffusivity ratio [51]. In Section 3.3, we have investigated the statistical characterization for the distribution of turbulence-induced fading in UVLC systems considering both horizontal and vertical links. We have further demonstrated that in a vertical UVLC link, water with different values of salinity and temperature form non-mixing layers due to ocean stratification. This results in variations of turbulence strength through the transmission range. Utilizing this, we modeled the vertical UVLC channel as a concatenation of multiple non-mixing layers and statistically characterized the cascaded channel. The fading coefficients associated with non-mixing layers are modeled as either i.n.i.d LN or GG random variables based on the strength of turbulence. These channel models are later used in Chapter 4 to derive closed-form expressions for BER, asymptotic BER and Ergodic capacity over both cascaded LN and GG turbulence channels [149–151].

In Chapter 4, we used the derived cascaded LN and GG turbulence channels in Chapter 3 and derived closed-form expressions for the BER performance of vertical links which were verified through numerical results. As a benchmark, we made comparisons with the performance of a hypothetical vertical link based on the assumption of constant turbulent strength. Our results demonstrated that such a simplifying assumption provides an inaccurate estimation of BER values where overestimation and/or underestimation are observed in different SNR regions. We further analyzed the asymptotic BER performance and determined the diversity gains. Our results demonstrated that the diversity gain is determined by the layer with minimum effective number of large-/small-scale cells in cascaded GG channels. On the other hand, in cascaded LN channels, all underlying layers contribute to the diversity order. In addition, we derived closed-form expressions for Ergodic capacity and investigated the effect of layering on the capacity [149–151].

Chapter 5 can be summarized as follow. In Section 5.2, we considered a MIMO UVLC system over LN turbulence channels, derived a novel closed-form BER expression, introduced the concept of IDO and quantified the achievable IDO as a function of the number of laser sources, the number of photo-detectors and the variance of the log-amplitude coefficient [110]. In Section 5.3, in an effort to reduce the hardware complexity, we proposed the use TLS in the context of UVLC. Since feedback error or outdated selection due to temporal changes in the channel may result in selecting another source rather than the best one, we considered an UVLC system with GTLS where the n^{th} best laser is selected among the available N lasers and determined the achievable IDO [135, 152].

Chapter 6 can be summarized as follow. In Section 6.2, we considered the downlink of a USN where the system is built upon OFDMA-based VLC. We presented an adaptive algorithm which aims to maximize the overall data rate subject to maintaining identical data rate for each underwater sensor node while satisfying a predefined maximum acceptable BER. Based on the information on channel gains per subcarrier of each node, the adaptive algorithm performs bit loading through sequential scheduling of subcarriers. To demonstrate the performance of the adaptive transmission, we conducted a simulation study of the OFDMA VLC system under consideration using channel gains obtained through non-sequential ray tracing for a realistic underwater setting and presented the achievable data rates [153]. In Section 6.3, we considered NOMA in the context of underwater sensor networks. To this end, we derived a simple closed-form expression for the NOMA capacity as well as a simple and accurate asymptotic representation. The derived closed-form expressions are in agreement with the corresponding analytic results while they are insightful and easy to compute. Analyzing the performance of the considered underwater network set up, we considered various scenarios where we studied the effect of different link distances on the overall NOMA capacity. We observed that the overall capacity is severely worsening with propagation distance which is due to the fact that the VLC channel gain severely drops with propagation distance. Therefore, the considered configuration can exhibit particularly high rates in the context of a local area network.

7.2 Future Work

In Chapter 2, we have considered different water types and determined the maximum achievable distance to satisfy a targeted end-to-end BER assuming turbulence free channels. We have further investigated the benefits of link adaptation in the absence of turbulence. Investigating the achievable distance as well as the benefits of link adaptation in the presence of turbulence can be a topic for future work.

In Chapter 3, we have investigated the effect of eddy diffusivity ratio on the scintillation index of optical plane and spherical waves.Therefore, investigating the effect of eddy diffusivity ratio on the other types of waves can be a topic for future work. We have as well modeled in Chapter 3 the vertical UVLC channel as a concatenation of multiple non-mixing layers and statistically characterized the cascaded channels for two cases: cascaded LN and cascaded GG turbulence channels. Therefore, modeling vertical link by considering different turbulence channels can be also a topic for future work.

In Chapter 4, we have considered cascaded LN and GG turbulence channels and derived closed-form expressions for the BER performance of vertical links, analyzed the asymptotic BER performance and determined the diversity gains. In addition, we have derived closed-form expressions for Ergodic capacity and investigated the effect of layering. Considering different turbulence channels for investigating error rate performance and the achievable capacity can be considered as an open research area.

In Chapter 5, we considered a MIMO and GTLS as a fading mitigation technique in the context of UVLC systems. We have just considered LN turbulence channels. However, full investigation can be done by considering different turbulence channels such as GG. Furthermore, relay-assisted transmission, which takes advantage of the shorter hops can also be considered as a fading mitigation technique.

In Chapter 6, we have considered the downlink of an USN where the system is built upon OFDMA-based VLC and proposed an adaptive algorithm that aims to maximize the overall data rate subject to maintaining identical data rate for each underwater sensor node while satisfying a predefined maximum acceptable BER in the absence of turbulence. The proposed adaptive algorithm can be extended considering different turbulence channels. We have also considered NOMA in the context of USN and derived a simple closed-form expression for the NOMA capacity as well as a simple and accurate asymptotic representation. However, full investigation of NOMA in the context of USN can be done by considering different turbulence channels such as GG.

PUBLICATIONS

Some of the research leading to this dissertation has appeared previously in the following publications.

Journal Articles

[1] **M. Elamassie**, M. Uysal, Y. Baykal, M. Abdallah, and K. Qaraqe, ”Effect of eddy diffusivity ratio on underwater optical scintillation index,” *J. Opt. Soc. Am. A*, vol. 34, no. 11, pp. 1969-1973, 2017.

[2] **M. Elamassie**, F. Miramirkhani and M. Uysal, ”Performance characterization of underwater visible light communication,” *IEEE Trans. Commun.*, vol. 67, no. 1, pp. 543-552, Jan. 2019.

[3] **M. Elamassie** and M. Uysal, ”Incremental diversity order for characterization of FSO communication systems over lognormal fading channels,” *IEEE Commun. Lett.*, vol. 24, no. 4, pp. 825-829, April 2020.

[4] **M. Elamassie** and M. Uysal, ”Asymptotic performance of generalized transmit laser selection over lognormal turbulence channels,” *Accepted for publication in IEEE Commun. Lett.*, doi: 10.1109/LCOMM.2020.2989560.

[5] **M. Elamassie** and M. Uysal, ”Vertical underwater visible light communication links: Channel modeling and performance analysis,” *Accepted for publication in IEEE Trans. Wireless Commun.*, 2020.

Conference Papers

[1] **M. Elamassie**, F. Miramirkhani, and M. Uysal, ”Channel modelling and performance characterization of underwater visible light communications,” *in IEEE International Conference on Communications Workshops (ICC Workshops): The 4th Workshop on Optical Wireless Communications (OWC) (ICC 2018 Workshop - OWC)*, Kansas City, USA, May 2018.

[2] **M. Elamassie** and M. Uysal, ”Performance characterization of vertical underwater VLC links in the presence of turbulence,” *in 11th IEEE/IET International Symposium on Communication Systems, Networks & Digital Signal Processing (CSNDSP'18)*, Budapest, Hungary, July 2018.

[3] **M. Elamassie**, S. M. Sait, and M. Uysal, ”Underwater visible light communications in cascaded Gamma-Gamma turbulence,” *in 8th IEEE GLOBECOM Workshop on Optical Wireless Communications (GC'18 WS - OWC)*, Abu Dhabi, United Arab Emirates, Dec. 2018.

[4] **M. Elamassie**, M. Karbalayghareh, F. Miramirkhani, and M. Uysal, ”Adaptive DCO-OFDM for Underwater Visible Light Communications,” *in IEEE 27th Signal Processing, Communication and Applications Conference (SIU)*, Sivas, Turkey, April 2019.

[5] **M. Elamassie**, M. Karbalayghareh, F. Miramirkhani, M. Uysal, M. M. Abdallah, and K. A. Qaraqe, ”Resource allocation for downlink OFDMA in underwater visible light communications,” *in IEEE International Black Sea Conference on Communications and Networking (BlackSeaCom) (IEEE BlackSeaCom 2019)*, Sochi, Russia, Jun. 2019. (**Best Paper Award**)

[6] **M. Elamassie** and M. Uysal, ”Vertical underwater VLC links over cascaded Gamma-Gamma turbulence channels with pointing errors,” *in IEEE International Black Sea Conference on Communications and Networking (BlackSeaCom) (IEEE BlackSeaCom 2019)*, Sochi, Russia, Jun. 2019.

[7] **M. Elamassie**, M. Al-Nahhal, R. C. Kizilirmak, and M. Uysal, ”Transmit laser selection for underwater visible light communication systems,” *IEEE 30th Annual International Symposium on Personal, Indoor and Mobile Radio Communications (PIMRC)*, Istanbul, Turkey, Sep. 2019.


IEEE BlackSeaCom™ IEEE IEEE ComSoc IEEE Communications Society

IEEE International Black Sea Conference on Communications and Networking

BEST PAPER AWARD

is presented to

Mohammed Elamassie, Mehdi Karbalayghareh, Farshad Miramirkhani, Murat Uysal, Mohamed M. Abdallah, Khalid A. Qaraqe

for the paper entitled

Resource Allocation for Downlink OFDMA in Underwater Visible Light Communications

3-6 June 2019 // Sochi, Russia

Evgeny Khorov | Noura Limam | Claudio Sacchi

TPC Chairs BlackSeaCom 2019

Bibliography

[1] C. M. G. Gussen, P. S. R. Diniz, M. L. R. Campos, W. A. Martins, and J. N. Gois, "A survey of underwater wireless communication technologies," *J. Commun. Inf. Sys.*, vol. 31, no. 1, pp. 242–255, 2016.

[2] Sonardyne Corporation, "Bluecomm underwater optical communication." https://www.sonardyne.com/product/bluecomm-underwater-optical-communication-system/. [Accessed: June 29, 2020].

[3] D. C. Sigee, *Freshwater microbiology: biodiversity and dynamic interactions of microorganisms in the aquatic environment*. John Wiley & Sons, June 2005.

[4] A. P. Klimley, *The biology of sharks and rays*. University of Chicago Press, 2013.

[5] C. Wang, H. Yu, Y. Zhu, and T. Wang, "Blind detection for SPAD-based underwater VLC system under P-G mixed noise model," *IEEE Commun. Lett.*, vol. 21, pp. 2602–2605, Dec. 2017.

[6] A. Tabeshnezhad and M. A. Pourmina, "Outage analysis of relay-assisted underwater wireless optical communication systems," *Optics Commun.*, vol. 405, pp. 297–305, Aug. 2017.

[7] T. Shafique, O. Amin, M. Abdallah, I. S. Ansari, M. Alouini, and K. Qaraqe, "Performance analysis of single-photon avalanche diode underwater VLC system using ARQ," *IEEE Photon. J.*, vol. 9, pp. 1–11, Oct. 2017.

[8] S. Hessien, S. C. Tokgöz, N. Anous, A. Boyacı, M. Abdallah, and K. A. Qaraqe, "Experimental evaluation of OFDM-based underwater visible light communication system," *IEEE Photon. J.*, vol. 10, pp. 1–13, Oct. 2018.

[9] G. Cossu, A. Sturniolo, A. Messa, D. Scaradozzi, and E. Ciaramella, "Full-Fledged 10Base-T ethernet underwater optical wireless communication system," *IEEE J. Sel. Areas Commun.*, vol. 36, pp. 194–202, Jan. 2018.

[10] Z. Vali, A. Gholami, Z. Ghassemlooy, M. Omoomi, and D. G. Michelson, "Experimental study of the turbulence effect on underwater optical wireless communications," *Appl. Opt.*, vol. 57, pp. 8314–8319, Oct. 2018.

[11] M. Elamassie, F. Miramirkhani, and M. Uysal, "Performance characterization of underwater visible light communication," *IEEE Trans. Commun.*, vol. 67, pp. 543–552, Jan 2019.

[12] N. Huang, M. Chen, W. Xu, and J. Wang, "Incorporating importance sampling in EM learning for sequence detection in SPAD underwater OWC," *IEEE Access*, vol. 7, pp. 4529–4537, 2019.

[13] N. Saeed, A. Celik, T. Y. Al-Naffouri, and M. Alouini, "Localization of energy harvesting empowered underwater optical wireless sensor networks," *IEEE Trans. Wireless Commun.*, vol. 18, pp. 2652–2663, May 2019.

[14] A. Yilmaz, M. Elamassie, and M. Uysal, "Diversity gain analysis of underwater vertical MIMO VLC links in the presence of turbulence," in *IEEE BlackSeaCom*, pp. 1–6, June 2019.

[15] Y. Wu, Y. Zhang, and Y. Zhu, "Average intensity and directionality of partially coherent model beams propagating in turbulent ocean," *J. Opt. Soc. Am. A*, vol. 33, no. 8, pp. 1451–1458, 2016.

[16] K. P. Peppas, A. C. Boucouvalas, and Z. Ghassemloy, "Performance of underwater optical wireless communication with multi-pulse pulse-position modulation receivers and spatial diversity," *IET Optoelectron.*, vol. 11, no. 5, pp. 180 –185, 2017.

[17] M. V. Jamali, J. A. Salehi, and F. Akhoundi, "Performance studies of underwater wireless optical communication systems with spatial diversity: MIMO scheme," *IEEE Trans. Commun.*, vol. 65, pp. 1176–1192, Mar. 2017.

[18] M. V. Jamali, P. Nabavi, and J. A. Salehi, "MIMO underwater visible light communications: Comprehensive channel study, performance analysis, and multiple-symbol detection," *IEEE Trans. Veh. Technol.*, vol. 67, pp. 8223–8237, Sep. 2018.

[19] S. M. Navidpour, M. Uysal, and M. Kavehrad, "BER performance of free-space optical transmission with spatial diversity," *IEEE Trans. Wireless Commun.*, vol. 6, pp. 2813–2819, Aug. 2007.

[20] M. T. Dabiri, M. J. Saber, and S. M. S. Sadough, "On the performance of multiplexing FSO MIMO links in log-normal fading with pointing errors," *IEEE/OSA J. Opt. Commun. Netw*, vol. 9, pp. 974–983, Nov. 2017.

[21] A. A. Farid and S. Hranilovic, "Diversity gain and outage probability for MIMO free-space optical links with misalignment," *IEEE Trans. Commun.*, vol. 60, pp. 479–487, Feb. 2012.

[22] B. Castillo-Vazquez, A. Garcia-Zambrana, and C. Castillo-Vazquez, "Closed-form BER expression for FSO links with transmit laser selection over exponential atmospheric turbulence channels," *Electro. Lett.*, vol. 45, pp. 1185–1187, Nov. 2009.

[23] H. Samimi, "Free-space optical link with dual-branch transmit laser selection diversity over double generalised gamma turbulence channel," *IET Commun.*, vol. 11, no. 15, pp. 2345–2349, 2017.

[24] A. García-Zambrana, B. Castillo-Vázquez, and C. Castillo-Vázquez, "Asymptotic error-rate analysis of FSO links using transmit laser selection over gamma-gamma atmospheric turbulence channels with pointing errors," *Opt. Express*, vol. 20, pp. 2096–2109, Jan 2012.

[25] Z. Zeng, S. Fu, H. Zhang, Y. Dong, and J. Cheng, "A survey of underwater optical wireless communications," *IEEE Commun. Surveys Tuts.*, vol. 19, pp. 204–238, Mar. 2017.

[26] K. Nakamura, I. Mizukoshi, and M. Hanawa, "Optical wireless transmission of 405 nm, 1.45 Gbit/s optical IM/DD-OFDM signals through a 4.8 m underwater channel," *Opt. Express*, vol. 23, pp. 1558–1566, Jan. 2015.

[27] C. Shen, Y. Guo, H. M. Oubei, T. K. Ng, G. Liu, K.-H. Park, K.-T. Ho, M.-S. Alouini, and B. S. Ooi, "20-meter underwater wireless optical communication link with 1.5 Gbps data rate," *Opt. Express*, vol. 24, pp. 25502–25509, Oct 2016.

[28] J. Xu, Y. Song, X. Yu, A. Lin, M. Kong, J. Han, and N. Deng, "Underwater wireless transmission of high-speed QAM-OFDM signals using a compact red-light laser," *Opt. Express*, vol. 24, pp. 8097–8109, Apr. 2016.

[29] M. Kong, W. Lv, T. Ali, R. Sarwar, C. Yu, Y. Qiu, F. Qu, Z. Xu, J. Han, and J. Xu, "10-m 9.51-Gb/s RGB laser diodes-based WDM underwater wireless optical communication," *Opt. Express*, vol. 25, pp. 20829–20834, Aug. 2017.

[30] C. Gabriel, M.-A. Khalighi, S. Bourennane, P. Leon, and V. Rigaud, "Channel modeling for underwater optical communication," in *Proc. IEEE Glob. Commun. Conf. (GLOBECOM'11)*, (Houston, TX, USA), Dec. 2011.

[31] C. Gabriel, M.-A. Khalighi, S. Bourennane, P. Léon, and V. Rigaud, "Monte-Carlo-based channel characterization for underwater optical communication systems," *IEEE/OSA J. Opt. Commun. Netw.*, vol. 5, pp. 1–12, Jan. 2013.

[32] S. Tang, Y. Dong, and X. Zhang, "On path loss of NLOS underwater wireless optical communication links," in *Proc. MTS/IEEE OCEANS (OCEANS'13)*, (Bergen, Norway), Jan. 2013.

[33] V. Guerra, C. Quintana, J. Rufo, J. Rabadan, and R. Perez-Jimenez, "Parallelization of a Monte Carlo ray tracing algorithm for channel modelling in underwater wireless optical communications," *Proc. Technol.*, vol. 7, pp. 11 – 19, 2013. 3rd Iberoamerican Conference on Electronics Engineering and Computer Science, CIIECC.

[34] V. Guerra, O. El-Asmar, C. Suarez-Rodriguez, and R. Perez-Jimenez, "Statistical study of the channel parameters in underwater wireless optical links," in *IEEE Int. Work Conf. Bio-inspired Intell. (IWOBI)*, (Liberia, Costa Rica), July 2014.

[35] W. Liu, D. Zou, P. Wang, Z. Xu, and L. Yang, "Wavelength dependent channel characterization for underwater optical wireless communications," in *IEEE Int. Conf. Signal Processing, Communications and Computing (ICSPCC'14)*, (Guilin, China), Aug. 2014.

[36] Y. Dong, H. Zhang, and X. Zhang, "On impulse response modeling for underwater wireless optical MIMO links," in *Proc. IEEE/CIC Int. Conf. Commun. in China (ICCC'14)*, (Shanghai, China), Oct. 2014.

[37] F. Miramirkhani and M. Uysal, “Visible light communication channel modeling for underwater environments with blocking and shadowing,” *IEEE Access*, vol. 6, pp. 1082–1090, 2018.

[38] S. Arnon and D. Kedar, “Non-line-of-sight underwater optical wireless communication network,” *J. Opt. Soc. Am. A*, vol. 26, pp. 530–539, Mar. 2009.

[39] A. Mora, D. Ganger, G. Wells, J. Zhang, X. Hu, C. Zhou, A. Richa, and C. Youngbull, “Ad-hoc multi-hop underwater optical network for deep ocean monitoring,” in *Oceans - San Diego*, (San Diego, CA, USA), Sept. 2013.

[40] F. Akhoundi, J. A. Salehi, and A. Tashakori, “Cellular underwater wireless optical CDMA network: Performance analysis and implementation concepts,” *IEEE Trans. Commun.*, vol. 63, pp. 882–891, Mar. 2015.

[41] M. V. Jamali, F. Akhoundi, and J. A. Salehi, “Performance characterization of relay-assisted wireless optical CDMA networks in turbulent underwater channel,” *IEEE Trans. Wireless Commun.*, vol. 15, pp. 4104–4116, June 2016.

[42] M. V. Jamali, A. Chizari, and J. A. Salehi, “Performance analysis of multi-hop underwater wireless optical communication systems,” *IEEE Photon. Technol. Lett.*, vol. 29, pp. 462–465, Mar. 2017.

[43] X. Ma, F. Yang, S. Liu, and J. Song, “Channel estimation for wideband underwater visible light communication: a compressive sensing perspective,” *Opt. Express*, vol. 26, pp. 311–321, Jan 2018.

[44] S. Arnon, J. R. Barry, G. K. Karagiannidis, R. Schober, and M. Uysal, *Advanced Optical Wireless Communication Systems*. Cambridge Univ. Press, 1 ed., 2012.

[45] C. Li, K.-H. Park, and M.-S. Alouini, “On the use of a direct radiative transfer equation solver for path loss calculation in underwater optical wireless channels,” *IEEE Commun. Lett.*, vol. 4, pp. 561–564, Oct. 2015.

[46] S. Jaruwatanadilok, “Underwater wireless optical communication channel modeling and performance evaluation using vector radiative transfer theory,” *IEEE J. Sel. Areas Commun.*, vol. 26, pp. 1620–1627, Dec. 2008.

[47] B. M. Cochenour, L. J. Mullen, and A. E. Laux, “Characterization of the beam-spread function for underwater wireless optical communications links,” *IEEE J. Ocean. Eng.*, vol. 33, pp. 513–521, Oct. 2008.

[48] B. Cochenour, L. Mullen, and A. Laux, “Spatial and temporal dispersion in high bandwidth underwater laser communication links,” in *Proc. IEEE Military Commun. Conf. (MILCOM)*, (San Diego, CA, USA), Nov. 2008.

[49] C. D. Mobley, B. Gentili, H. R. Gordon, Z. Jin, G. W. Kattawar, A. Morel, P. Reinersman, K. Stamnes, and R. H. Stavn, “Comparison of numerical models for computing underwater light fields,” *Appl. Opt.*, vol. 32, pp. 7484–7504, Dec. 1993.

[50] W. C. Cox, *Simulation, modeling, and design of underwater optical communication systems*. PhD thesis, North Carolina State University, Raleigh, North Carolina, USA, 2012.

[51] M. Elamassie, M. Uysal, Y. Baykal, M. Abdallah, and K. Qaraqe, "Effect of eddy diffusivity ratio on underwater optical scintillation index," *J. Opt. Soc. Am. A*, vol. 34, no. 11, pp. 1969–1973, 2017.

[52] M. Bernotas and C. Nelson, "Probability density function analysis for optimization of underwater optical communications systems," in *OCEANS 2015 - MTS/IEEE Washington*, pp. 1–8, 2015.

[53] H. M. Oubei, E. Zedini, R. T. ElAfandy, A. Kammoun, M. Abdallah, T. K. Ng, M. Hamdi, M.-S. Alouini, and B. S. Ooi, "Simple statistical channel model for weak temperature-induced turbulence in underwater wireless optical communication systems," *Opt. Lett.*, vol. 42, pp. 2455–2458, Jul 2017.

[54] M. V. Jamali, A. Mirani, A. Parsay, B. Abolhassani, P. Nabavi, A. Chizari, P. Khorramshahi, S. Abdollahramezani, and J. A. Salehi, "Statistical studies of fading in underwater wireless optical channels in the presence of air bubble, temperature, and salinity random variations," *IEEE Trans. Commun.*, vol. 66, no. 10, pp. 4706–4723, 2018.

[55] M. V. Jamali, P. Khorramshahi, A. Tashakori, A. Chizari, S. Shahsavari, S. AbdollahRamezani, M. Fazelian, S. Bahrani, and J. A. Salehi, "Statistical distribution of intensity fluctuations for underwater wireless optical channels in the presence of air bubbles," in *Iran Workshop on Communication and Information Theory (IWCIT)*, pp. 1–6, 2016.

[56] Y. Fu and Y. Du, "Performance of heterodyne differential phase-shift-keying underwater wireless optical communication systems in gamma-gamma-distributed turbulence," *Appl. Opt.*, vol. 57, pp. 2057–2063, Mar 2018.

[57] Y. Ji, G. Wu, and C. Wang, "Generalized likelihood block detection for SPAD-based underwater VLC system," *IEEE Photon. J.*, vol. 12, no. 1, pp. 1–10, 2020.

[58] S. Tannaz, C. Ghobadi, J. Nourinia, and E. Mostafapour, "Theoretical analysis of the underwater incremental adaptive network performance based on the vlc technology," *Wireless Personal Communications*, 2020.

[59] H. Jiang, H. Qiu, N. He, W. Popoola, Z. Ahmad, and S. Rajbhandari, "Performance of spatial diversity DCO-OFDM in a weak turbulence underwater visible light communication channel," *J. Lightw. Technol.*, vol. 38, no. 8, pp. 2271–2277, 2020.

[60] R. Chester and T. D. Jickells, *Marine Geochemistry*. Wiley-blackwell, 3 ed., Oct. 2012.

[61] R. Griffis and J. Howard, *Oceans and marine resources in a changing climate: a technical input to the 2013 national climate assessment*. Island Press, 2013.

[62] V. V. Nikishov and V. I. Nikishov, “Spectum of turbulence fluctuations of the sea-water refraction index,” *Int. J. Fluid Mech. Res.*, vol. 27, no. 1, p. 82–98, 2000.

[63] R. D. Muench, H. J. S. Fernando, and G. R. Stegen, “Temperature and salinity staircases in the northwestern weddell sea,” *American Meteorological Society*, vol. 20, pp. 295–306, Feb. 1990.

[64] G. D. Gilbert and R. C. Honey, “Optical turbulence in the sea,” *Underwater Photo-Optical Instrumentation Applications*, vol. 0024, p. 49–55, Jun. 1971.

[65] H. Stommel and K. N. Fedorov, “Small scale structure in temperature and salinity near timor and mindanao,” *Tellus*, vol. 19, no. 2, p. 306–325, 1967.

[66] J. J. Shynk, *Mathematical Foundations for Linear Circuits and Systems in Engineering*. Wiley, 1 ed., 2016.

[67] A. Goldsmith, *Wireless communications*. Cambridge: Cambridge Univ. Press, 1 ed., 2005.

[68] J. Grubor, S. Randel, K.-D. Langer, and J. W. Walewski, “Broadband information broadcasting using LED-based interior lighting,” *J. Lightw. Technol.*, vol. 26, pp. 3883–3892, Dec. 2008.

[69] C. E. Webb and J. D. C. Jones, *Handbook of Laser Technology and Applications: Laser design and laser systems*, vol. 2 of *Handbook of Laser Technology and Applications*. Bristol, Philadelphia: Institute of Physics (IoP) Ltd, 2004.

[70] W. Zheng and M. A. Ingram, “Maximum multi-hop range using cooperative transmission with a fixed number of nodes,” in *2013 IEEE Int. Conf. Commun. (ICC)*, June 2013.

[71] Q. Wang, M. Hempstead, and W. Yang, “A realistic power consumption model for wireless sensor network devices,” in *3rd Annual IEEE Communications Society on Sensor and Ad Hoc Communications and Networks*, Sept 2006.

[72] A. Muller and J. Speidel, “Achieving exponential diversity in wireless multihop systems with regenerative relays,” in *Proc. IEEE Int. Conf. Commun. (ICC)*, (Dresden, Germany), June 2009.

[73] M. Chiani, D. Dardari, and M. K. Simon, “New exponential bounds and approximations for the computation of error probability in fading channels,” *IEEE Trans. Wireless Commun.*, vol. 2, pp. 840–845, July 2003.

[74] L. Sperling, *Introduction to physical polymer science*. John Wiley & Sons: CRC Pres, 4 ed., 2005.

[75] E. Morgado, I. Mora-Jiménez, J. J. Vinagre, J. Ramos, and A. J. Caamaño, “End-to-end average BER in multihop wireless networks over fading channels,” *IEEE Trans. Wireless Commun.*, vol. 9, pp. 2478–2487, Aug. 2010.

[76] M. O. Hasna and M.-S. Alouini, "Outage probability of multihop transmission over Nakagami fading channels," *IEEE Commun. Lett.*, vol. 7, pp. 216–218, May 2003.

[77] P. Xia, S. Zhou, and G. B. Giannakis, "Adaptive MIMO-OFDM based on partial channel state information," *IEEE Trans. Signal Process.*, vol. 52, pp. 202–213, Jan. 2004.

[78] R. F. H. Fischer and J. B. Huber, "A new loading algorithm for discrete multitone transmission," in *IEEE Global Telecommunications Conference*, pp. 724–728, Nov. 1996.

[79] B. S. Krongold, K. Ramchandran, and D. L. Jones, "Computationally efficient optimal power allocation algorithm for multicarrier communication systems," in *IEEE International Conference on Communications (ICC'98)*, pp. 1018–1022, June 1998.

[80] O. Narmanlioglu, R. C. Kizilirmak, T. Baykas, and M. Uysal, "Link adaptation for MIMO OFDM visible light communication systems," *IEEE Access*, vol. 5, pp. 26006–26014, 2017.

[81] A. Radosevic, T. M. Duman, J. G. Proakis, and M. Stojanovic, "Adaptive OFDM for underwater acoustic channels with limited feedback," in *Conference Record of the Forty Fifth Asilomar Conference on Signals, Systems and Computers (ASILOMAR)*, pp. 975–980, 2011.

[82] O. Korotkova, N. Farwell, and E. Shchepakina, "Light scintillation in oceanic turbulence," *Waves Random Complex Media*, vol. 22, pp. 260–266, 5 2012.

[83] Y. Ata and Y. Baykal, "Scintillations of optical plane and spherical waves in underwater turbulence," *J. Opt. Soc. Am. A*, vol. 31, pp. 1552–1556, Jul 2014.

[84] H. Gerçekcioğlu, "Bit error rate of focused gaussian beams in weak oceanic turbulence," *J. Opt. Soc. Am. A*, vol. 31, pp. 1963–1968, Sep 2014.

[85] M. Yousefi, S. Golmohammady, A. Mashal, and F. D. Kashani, "Analyzing the propagation behavior of scintillation index and bit error rate of a partially coherent flat-topped laser beam in oceanic turbulence," *J. Opt. Soc. Am. A*, vol. 32, pp. 1982–1992, Nov 2015.

[86] X. Yi, Z. Li, and Z. Liu, "Underwater optical communication performance for laser beam propagation through weak oceanic turbulence," *Appl. Opt.*, vol. 54, pp. 1273–1278, Feb 2015.

[87] Y. Baykal, "Higher order mode laser beam scintillations in oceanic medium," *Waves Random Complex Media*, vol. 26, no. 1, pp. 21–29, 2016.

[88] S. A. Arpali, Y. Baykal, and Çağlar Arpali, "Ber evaluations for multimode beams in underwater turbulence," *J. Mod. Opt.*, vol. 63, no. 13, pp. 1297–1300, 2016.

[89] N. Farwell and O. Korotkova, “Intensity and coherence properties of light in oceanic turbulence,” *Opt. Commun.*, vol. 285, pp. 872–875, 2012.

[90] K. N. Fedorov, *The thermohaline finestructure of the ocean*. pergamon Press, 1978.

[91] P. R. Jackson and C. R. Rehmann, “Laboratory measurements of differential diffusion in a diffusively stable, turbulent flow,” *J. Phys. Oceanogr.*, vol. 33, no. 8, pp. 1592–1603, 2003.

[92] T. Radko, *Double-diffusive convection*. Cambridge University Press, 2013.

[93] E. Kunze, “A review of oceanic salt-fingering theory,” *Prog. Oceanogr.*, vol. 56, no. 3, pp. 399–417, 2003.

[94] L. C. Andrews and R. L. Phillips, *Laser Beam Propagation through Random Media*. Bellingham, WA, USA: SPIE, 2 ed., 2005.

[95] E. B. Kraus and J. A. Businger, *Atmosphere–Ocean Interaction*. Oxford University Press, 1994.

[96] N. Ramsing and J. Gundersen, *Seawater and gases: tabulated physical parameters of interest to people working with microsensors in marine systems*. Unisense, 2000.

[97] Z. Ghassemlooy, W. Popoola, and S. Rajbhandari, *Optical wireless communications: system and channel modelling with MATLAB*. CRC Press, 2013.

[98] S. Tang, Y. Dong, and X. Zhang, “Impulse response modeling for underwater wireless optical communication links,” *IEEE Trans. Commun.*, vol. 62, pp. 226–234, Jan 2014.

[99] J. H. Drew, D. L. Evans, A. G. Glen, and L. M. Leemis, *Computational Probability: Algorithms and Applications in the Mathematical Sciences*. Springer Publishing Company, 2 ed., 2017.

[100] Wolfram Research, Inc. http://functions.wolfram.com. [Accessed: June 29, 2020].

[101] P. M. Shankar, *Fading and Shadowing in Wireless Systems*. New York, USA: Springer, 2012.

[102] D. S. Gunderson, *Handbook of Mathematical Induction: Theory and Applications*. Discrete Mathematics and Its Applications, CRC Press, 2010.

[103] Z. Wang, Q. Wang, W. Huang, and Z. Xu, *Visible light communications: modulation and signal processing*. Hoboken, New Jersey: Wiley-IEEE Press, 2017.

[104] H. Moradi, M. Falahpour, H. H. Refai, P. G. LoPresti, and M. Atiquzzaman, “BER analysis of optical wireless signals through lognormal fading channels with perfect CSI,” in *17th International Conference on Telecommunications*, (Doha, Qatar), pp. 493–497, 2010.

[105] G. Yang, Z. Li, M. Bi, X. Zhou, R. Zeng, T. Wang, and J. Li, "Channel modeling and performance analysis of modulating retroreflector FSO systems under weak turbulence conditions," *IEEE Photon. J.*, vol. 9, pp. 1–10, April 2017.

[106] P. Saxena and M. R. Bhatnagar, "A simplified form of beam spread function in underwater wireless optical communication and its applications," *IEEE Access*, vol. 7, pp. 105298–105313, 2019.

[107] R. Korn, *Optimal Portfolios. Stochastic Models for Optimal Investment and Risk Management in Continuous Time*. Singapore: World Scientific, 1997.

[108] D. Belkić, "The Euler T and Lambert W functions in mechanistic radiobiological models with chemical kinetics for repair of irradiated cells," *J. Math. Chemistry*, vol. 56, pp. 2133–2193, Sep. 2018.

[109] M. Safari and M. Uysal, "Cooperative diversity over log-normal fading channels: performance analysis and optimization," *IEEE Trans. Wireless Commun.*, vol. 7, pp. 1963–1972, May. 2008.

[110] M. Elamassie and M. Uysal, "Incremental diversity order for characterization of FSO communication systems over lognormal fading channels," *IEEE Commun. Lett.*, vol. 24, pp. 825–829, Apr. 2020.

[111] Z. Abu-Almaalie, Z. Ghassemlooy, M. R. Bhatnagar, H. Le-Minh, N. Aslam, S.-K. Liaw, and I. E. Lee, "Investigation on iterative multiuser detection physical layer network coding in two-way relay free-space optical links with turbulences and pointing errors," *Appl. Opt.*, vol. 55, pp. 9396–9406, Nov 2016.

[112] L. Yin and H. Haas, "Physical-layer security in multiuser visible light communication networks," *IEEE J. Sel. Area Commun.*, vol. 36, no. 1, pp. 162–174, 2018.

[113] J. M. Holtzmann, "On using perturbation analysis to do sensitivity analysis: Derivatives versus differences," *IEEE Trans. Automat. Contr.*, vol. 37, pp. 243–247, Feb. 1992.

[114] R. X. Huang, *Ocean circulation: wind-driven and thermohaline processes*. Cambridge University Press, 2010.

[115] M. Safari and M. Uysal, "Cooperative diversity over log-normal fading channels: performance analysis and optimization," *IEEE Trans. Wireless Commun.*, vol. 7, pp. 1963–1972, May 2008.

[116] C. Abou-Rjeily and M. Bkassiny, "On the achievable diversity orders over non-severely faded lognormal channels," *IEEE Commun. Lett.*, vol. 14, pp. 695–697, Aug. 2010.

[117] M. A. Kashani, M. Safari, and M. Uysal, "Optimal relay placement and diversity analysis of relay-assisted free-space optical communication systems," *IEEE/OSA J. Opt. Commun. Netw*, vol. 5, pp. 37–47, Jan. 2013.

[118] M. A. Kashani and M. Uysal, "Outage performance and diversity gain analysis of free-space optical multi-hop parallel relaying," *IEEE/OSA J. Opt. Commun. Netw.*, vol. 5, pp. 901–909, Aug 2013.

[119] L. Yang, X. Gao, and M.-S. Alouini, "Performance analysis of free-space optical communication systems with multiuser diversity over atmospheric turbulence channels," *IEEE Photon. J.*, vol. 6, pp. 1–17, April 2014.

[120] F. Yang and J. Cheng, "Recent results on correlated lognormal atmospheric turbulence channels," in *International Conference on Computing, Networking and Communications (ICNC)*, pp. 1–6, Feb. 2016.

[121] D. Skraparlis, V. K. Sakarellos, A. D. Panagopoulos, and J. D. Kanellopoulo, "Outage performance analysis of cooperative diversity with MRC and SC in correlated lognormal channels," *EURASIP J. Wireless Commun. Netw.*, vol. 2009, pp. 1–7, Jul. 2009.

[122] G. Pan, E. Ekici, and Q. Feng, "Performance analysis of multi-branch multi-hop wireless relay systems over log-normal channels," *IEEE Trans. Wireless Commun.*, vol. 13, pp. 223–233, Jan. 2014.

[123] L. Yang, K. Qaraqe, E. Serpedin, and X. Gao, "Performance analysis of two-way relaying networks with the *N*th worst relay selection over various fading channels," *IEEE Trans. Veh. Technol.*, vol. 64, pp. 3321–3327, July 2015.

[124] A. Chaaban, Y. Sapenov, Z. Rezki, and M. Alouini, "Average worst-case PEP optimality of repetition coding among rate-1 DC-offset STBCs for MIMO optical intensity channels," *IEEE Trans. Commun.*, vol. 66, pp. 6409–6422, Dec 2018.

[125] E. Lee and V. Chan, "Part 1: optical communication over the clear turbulent atmospheric channel using diversity," *IEEE J. Sel. Areas Commun.*, vol. 22, pp. 1896–1906, Nov. 2004.

[126] E. L. Crow and K. Shimizu, *Lognormal Distributions: Theory and Applications*. Taylor & Francis Group, 1988.

[127] C. Abou-Rjeily, "Power allocation for quantum-limited multihop free-space optical communication systems," *IEEE Commun. Lett.*, vol. 16, pp. 2068–2071, Dec. 2012.

[128] M. Romeo, V. D. Costa, and F. Bardou, "Broad distribution effects in sums of lognormal random variables," *Eur. Phys. J.*, vol. 32, no. 4, pp. 513–525, 2013.

[129] P. Fan, "New inequalities of Mills ratio and application to the inverse Q-function approximation," *Aust. J. Math. Anal. Appl.*, vol. 10, Oct. 2013.

[130] B. C. Arnold, N. Balakrishnan, and H. N. Nagaraj, *A First Course in Order Statistics*. Society for Industrial and Applied Mathematics, 2008.

[131] A. A. Farid and S. Hranilovic, "Outage capacity optimization for free-space optical links with pointing errors," *J. Lightw. Technol.*, vol. 25, no. 7, pp. 1702–1710, 2007.

[132] E. W. Ng and M. Gelle, "A table of integrals of the error functions*," *J. Res. Nat. Bur. Stand.*, vol. 73B, no. 1, pp. 1–20, 1968.

[133] H. Dutta and J. F. Peters, *Applied Mathematical Analysis: Theory, Methods, and Applications*. Springer, 2020.

[134] M. Abramowitz and I. A. Stegun, *Handbook of Mathematical Functions: with Formulas, Graphs, and Mathematical Tables*. New York, NY, USA: Dover: US Government printing office, 10 ed., Dec. 1972.

[135] M. Elamassie, M. Al-Nahhal, R. C. Kizilirmak, and M. Uysal, "Transmit laser selection for underwater visible light communication systems," in *IEEE 30th Annual International Symposium on Personal, Indoor and Mobile Radio Communications (PIMRC)*, (Istanbul, Turkey), Sep. 2019.

[136] Z. Ding, X. Lei, G. K. Karagiannidis, R. Schober, J. Yuan, and V. K. Bhargava, "A survey on non-orthogonal multiple access for 5G networks: Research challenges and future trends," *IEEE J. Sel. Areas Commun*, vol. 35, pp. 2181–2195, Oct 2017.

[137] A. Batra, J. Balakrishnan, A. Dabak, R. Gharpurey, P. Fontaine, J. Lin, J.-M. Ho, and S. Lee, "TI physical layer proposal for IEEE 802.15 task group 3a," IEEE P802.15-03/142r2-TG3a, May. 2003.

[138] K. Cho and D. Yoon, "On the general BER expression of one- and two-dimensional amplitude modulations," *IEEE Trans. Commun.*, vol. 50, pp. 1074–1080, July 2002.

[139] C. Liu, A. Schmeink, and R. Mathar, "Equal rate resource allocation for multiuser OFDM," *EURASIP J. on Wireless Commun. and Netw.*, vol. 2012, p. 344, Nov. 2012.

[140] S. Sendra, J. Lloret, J. M. Jimenez, and L. Parra, "Underwater acoustic modems," *IEEE Sens. j.*, vol. 16, pp. 4063–4071, Jun. 2016.

[141] T. Fath and H. Haas, "Performance comparison of MIMO techniques for optical wireless communications in indoor environments," *IEEE Trans. Commun.*, vol. 61, pp. 733–742, Feb. 2013.

[142] C. He, T. Q. Wang, and J. Armstrong, "Performance of optical receivers using photodetectors with different fields of view in a MIMO ACO-OFDM system," *J. Lightw. Technol.*, vol. 33, pp. 4957–4967, Dec. 2015.

[143] L. Yin, W. O. Popoola, X. Wu, and H. Haas, "Performance evaluation of non-orthogonal multiple access in visible light communication," *IEEE Trans. Commun.*, vol. 64, pp. 5162–5175, Dec 2016.

[144] T. Q. Wang, C. He, and J. Armstrong, "Performance analysis of aperture-based receivers for MIMO IM/DD visible light communications," *J. Lightw. Technol.*, vol. 35, pp. 1513–1523, May 2017.

[145] M. Cheng, L. Guo, and Y. Zhang, “Scintillation and aperture averaging for Gaussian beams through non-Kolmogorov maritime atmospheric turbulence channels,” *Opt. Express*, vol. 23, pp. 32606–32621, Dec. 2015.

[146] E. Bjornson, M. Matthaiou, and M. Debbah, “A new look at dual-hop relaying: Performance limits with hardware impairments,” *IEEE Trans. Commun.*, vol. 61, pp. 4512–4525, Nov. 2013.

[147] M. Elamassie, F. Miramirkhani, and M. Uysal, “Channel modeling and performance characterization of underwater visible light communications,” in *IEEE International Conference on Communications Workshops (ICC Workshops)*, pp. 1–5, 2018.

[148] M. Elamassie, M. Karbalayghareh, F. Miramirkhani, and M. Uysal, “Adaptive DCO-OFDM for underwater visible light communications,” in *27th Signal Processing and Communications Applications Conference (SIU)*, pp. 1–4, 2019.

[149] M. Elamassie and M. Uysal, “Performance characterization of vertical underwater VLC links in the presence of turbulence,” in *11th International Symposium on Communication Systems, Networks Digital Signal Processing (CSNDSP)*, pp. 1–6, 2018.

[150] M. Elamassie, S. M. Sait, and M. Uysal, “Underwater visible light communications in cascaded Gamma-Gamma turbulence,” in *IEEE Globecom Workshops (GC Wkshps)*, pp. 1–6, 2018.

[151] M. Elamassie and M. Uysal, “Vertical underwater visible light communication links: Channel modeling and performance analysis,” *Accepted for publication in IEEE Trans. Wireless Commun.*, 2020.

[152] M. Elamassie and M. Uysal, “Asymptotic performance of generalized transmit laser selection over lognormal turbulence channels,” *IEEE Commun. Lett.*, 2020.

[153] M. Elamassie, M. Karbalayghareh, F. Miramirkhani, M. Uysal, M. Abdallah, and K. Qaraqe, “Resource allocation for downlink OFDMA in underwater visible light communications,” in *IEEE BlackSeaCom*, pp. 1–6, June 2019.

VITA

Mohammed Elamassie is a Palestinian researcher. He was born in Tlemcen, Algeria. He received the B.Sc. and M.Sc. degrees (Hons.) in electrical engineering from the Islamic University of Gaza, Gaza Strip, Palestine, in 2006 and 2011, respectively. He joined the Communication Theory and Technologies (CT&T) Research Group as a Research Assistant in 2015 working toward his doctorate under the supervision of Prof. Murat Uysal at Özyeğin University, Istanbul, Turkey. His current research interests include visible light communications, optical turbulence, underwater acoustic communication, diversity techniques for fading channels, performance analysis over fading channels and time-varying channels, channel estimation and equalization, multi-input multi-output (MIMO) communications.

Elamassie is a Review Editor on the Editorial Board of Non-Conventional Communications and Networks (specialty section of Frontiers in Communications and Networks). He is also a Review Editor on the Editorial Board of Wireless Communications (specialty section of Frontiers in Communications and Networks). He as well has served as a reviewer for Institute of Electrical & Electronics Engineers (IEEE) and Optical Society of America (OSA) journals and conferences.

He has several practical experiences as he served as a designing and supervising Electrical Engineer with the Engineering Office & Development Department, Ministry of Health, Gaza, Palestine for four years. Mr Elamassie is a member of OSA with membership No.1390625 and IEEE with membership No. 94182541.